SPACE-CHARGE SATURATION AND CURRENT LIMITS IN CYLINDRICAL DRIFT TUBES AND PLANAR SHEATHS

Kenneth Frank Stephens II, B.S., M.S.

Dissertation Prepared for the Degree of

DOCTOR OF PHILOSOPHY

UNIVERSITY OF NORTH TEXAS

August, 2000

APPROVED:

Carlos A. Ordonez, Major Professor

William D. Deering, Committee Member, Professor of Physics

Duncan Weathers, Committee Member, Professor of Physics

Jim Roberts, Committee Member, Professor of Physics

Sam Matteson, Chair, Department of Physics

C. Neal Tate, Dean of the Robert B. Toulouse School of Graduate Studies

Stephens, Kenneth Frank II, Space-Charge Saturation and Current Limits in Cylindrical Drift Tubes and Planar Sheaths. Doctor of Philosophy (Physics), August 2000, 146 pp., 2 tables, 23 illustrations, bibliography, 79 titles.

Space-charge effects play a dominant role in many areas of physics. In high-power microwave devices using high-current, relativistic electron beams, it places a limit on the amount of radiation a device can produce. Because the beam's space-charge can actually reflect a portion of the beam, the ability to accurately predict the amount of current a device can carry is needed. This current value is known as the space-charge limited current. Because of the mathematical difficulties, this limit is typically estimated from a one-dimensional theory. This work presents a two-dimensional theory for calculating an upper-bound for the space-charge limited current of relativistic electron beams propagating in grounded coaxial drift tubes. Applicable to annular beams of arbitrary radius and thickness, the theory includes the effect introduced by a finite-length drift tube of circular cross-section. Using Green's second identity, the need to solve Poisson's equation is transferred to solving a Sturm-Liouville eigenvalue problem, which is easily solved by elementary methods. In general, the resulting eigenvalue, which is required to estimate the limiting current, must be numerically determined. However, analytic expressions can be found for frequently encountered limiting cases.

Space-charge effects also produce the fundamental collective behavior found in plasmas, especially in plasma sheaths. A plasma sheath is the transition region between a bulk plasma and an adjacent plasma-facing surface. The sheath controls the loss of particles from the plasma in order to maintain neutrality. Using a fully kinetic theory, the

problem of a planar sheath with a single-minimum electric potential profile is investigated. Appropriate for single charge-state ions of arbitrary temperature, the theory includes the emission of warm electrons from the surface as well as a net current through the sheath and is compared to particle-in-cell simulations. Approximate expressions are developed for estimating the sheath potential as well as the transition to space-charge saturation. The case of a space-charge limited sheath is discussed and compared to the familiar Child-Langmuir law.

TABLE OF CONTENTS

LIST OF TABLES

LIST OF FIGURES

CHAPTER 1

INTRODUCTION TO SPACE-CHARGE LIMITED CURRENTS

It has been known for nearly a century that there is an upper limit on the amount of current that can pass between two electrodes. This limiting current is known as the space-charge limited (SCL) current and is one of the most important phenomena related to charged particle beams. For beam currents below this limit, the beam flow is laminar through the drift space and the problem is time-independent. However, if the beam current exceeds the SCL current a virtual cathode is formed and the transmitted current decreases. The virtual cathode is a point where a fraction of the beam particles come to rest and represents an instability in the beam. After the formation of a virtual cathode, the transmitted current decreases as the injected current increases. The ability to accurately determine the SCL current, in order to prevent or enhance the formation of a virtual cathode, is required in several fields, including high-power microwave devices,[1–4] astrophysical plasmas,[5] xerographic technology,[6] electron beam ion sources and traps,[7–9] field emitter arrays,[10] and collective-ion acceleration.[11,12] For most high-power microwave (HPM) devices the presence of a limiting current represents a limitation in the ability to produce microwave energy since an arbitrarily large electron beam current is not possible. On the otherhand, the vircator (VIRtual Cathode oscillATOR) and reflex triode use the presence of the virtual cathode as a means for microwave production.[1] In astrophysical plasmas, electric fields established in pulsar magnetospheres and white dwarf accretion disks are expected to establish currents that are space-charge limited.[5] Similar to simple diodes, xerographic devices

employ a potential difference to transport resin particles from a donor electrode to the receiver electrode as a means to transfer images.[6] Electron beam ion sources/traps use the potential depression of an electron beam to trap and/or create high charge state ions. High density beams, i.e., large current densities, are required to obtain high ionization efficiencies. The SCL current is one limitation that must be considered.[7] Field emitter arrays "hold the potential for significantly impacting next-generation radio-frequency amplifiers."[10] Employing numerous conical emitters and applying a larger potential difference between the gate electrode and anode, large current densities are possible and understanding the effects of space-charge on the current flow is essential. Collective-ion accelerators use a propagating virtual cathode formed within a high energy electron beam to accelerate the ions.[11] Thus, it is clear that knowledge of the space-charge limited current and the ability to predict it for a variety of beam and drift space geometries is important throughout physics.

Review of the Classical Space-Charge Limited Current Theory

For completeness, this section presents a review of the classical solution to the space-charge limited diode. A thorough discussion, along with numerous references and the early theory development, is given in the book by Birdsall and Bridges.[13] The problem geometry, illustrated in Fig. 1.1, consists of two ideal, infinite electrodes held at a potential difference of V_0 and separated by a distance L. The grounded cathode emits a zero temperature stream of electrons into the gap, which propagate to the anode (held at potential V_0). As long as the electron velocities are much less than the speed of light, the self-magnetic field can be neglected and the problem is one-dimensional. Starting with Poisson's equation (in SI units),

$$\frac{d^2\phi(x)}{dx^2} = -\frac{\rho(x)}{\epsilon_0}, \tag{1.1}$$

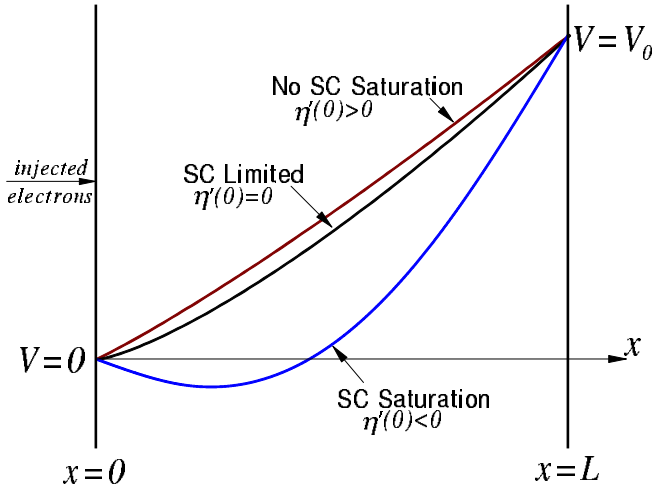

FIG. 1.1. Geometry considered in the classical space-charge limited flow problem. Cold electrons are injected from the grounded cathode into the gap. The electron stream travels a distance L to the anode, which is held at a potential, V_0. Also shown are three electric potential profiles illustrating the three regimes of space-charge effects, which can be classified by the value of the electric field at the cathode.

where $\phi(x)$ is the electric potential and $\rho(x)$ the charge density, the charge density can be written in terms of the potential by using conservation of charge and energy. Since all physical quantities are taken to be time independent, the continuity equation states that the current density is constant. Letting the current density be J_0, it is written in terms of the electron velocity and particle density as $J_0 = -en(x)v(x)$. From energy conservation, the velocity and potential are related through $v^2(x) = -2e\phi(x)/m$. Therefore, Poisson's equation can be re-written as

$$\frac{d^2\phi\left(x\right)}{dx^2} = -\frac{J_0}{\epsilon_0}\sqrt{\frac{m}{2e\phi\left(x\right)}}. \tag{1.2}$$

Changing variables according to $\zeta = x/L$ and $\eta = \phi/V_0$, this becomes

$$\frac{d^2\eta\left(\zeta\right)}{d\zeta^2} = -\frac{J_0L^2}{\epsilon_0V_0^{3/2}}\sqrt{\frac{m}{2e\eta\left(\zeta\right)}}. \tag{1.3}$$

If the current density is also scaled, using $j = J_0/J_{cl}$ where

$$J_{cl} = \frac{4\epsilon_0}{9L^2}\sqrt{\frac{2e}{m}}V_0^{3/2}, \tag{1.4}$$

Poisson's equation can be written in non-dimensional form as

$$\frac{d^2\eta\left(\zeta\right)}{d\zeta^2} = -\frac{4j}{9\sqrt{\eta\left(\zeta\right)}}, \tag{1.5}$$

and is subject to the boundary conditions $\eta(0) = 0$ and $\eta(1) = 1$. As will be seen, one important factor in the study of space-charge limited flow is the value of the electric field at the emitting surface. For the cases considered here, the value $\eta'(0)$ is of concern. To maintain consistency among these three conditions on $\eta(x)$, a relation is needed between the normalized current density, j, and the electric field at the surface, $\eta'(0)$. To this end, multiply Eq. (1.5) by $2\eta'(x)$ and re-write the result as

$$\frac{d}{d\zeta}\left[\frac{d\eta\left(\zeta\right)}{d\zeta}\right]^2 = \frac{16}{9}j\frac{d\sqrt{\eta\left(\zeta\right)}}{d\zeta}; \tag{1.6}$$

integrating yields

$$\left[\frac{d\eta\left(\zeta\right)}{d\zeta}\right]^2 - \left[\eta'\left(0\right)\right]^2 = \frac{16}{9}j\sqrt{\eta\left(\zeta\right)}, \tag{1.7}$$

where the boundary condition $\eta(0) = 0$ was used. Using the integral relation

$$\int_0^x \frac{dz}{\sqrt{a\sqrt{z}+b^2}} = \frac{4}{3a^2}\left[2b^3 + \left(a\sqrt{x} - 2b^2\right)\sqrt{a\sqrt{x}+b^2}\right], \tag{1.8}$$

the solution to this differential equation is

$$\left(\frac{4}{3}\right)^3 j^2\zeta = 2\left[\eta'\left(0\right)\right]^3 + \left(\frac{16}{9}j\sqrt{\eta\left(\zeta\right)} - 2\left[\eta'\left(0\right)\right]^2\right)\sqrt{\frac{16}{9}j\sqrt{\eta\left(\zeta\right)} + \left[\eta'\left(0\right)\right]^2}. \tag{1.9}$$

Using the boundary condition $\eta(1) = 1$, j can be expressed in terms of $\eta'(0)$ as

$$j = \frac{2 + \sqrt{4 - 27\left[1 - \eta'\left(0\right)\right]\left[\eta'\left(0\right)\right]^2}}{4}. \tag{1.10}$$

Using Eq. (1.10) in Eq. (1.9) and solving for $\eta(\zeta)$ gives the normalized electric potential with the only parameter being the electric field at the cathode. Since Eq. (1.9) is a cubic equation in $\eta(\zeta)$, the particular solution must be chosen to satisfy the given boundary conditions. The solution is not given here because of its complicated nature and yields no pertinent information for the present discussion.

From the discriminant of Eq. (1.10), it is clear that only a finite range of electric field values are appropriate to the analysis at hand: $-\frac{1}{3} \leq \eta'(0) \leq \frac{2}{3}$. However, the range of electric field values is more restrictive than this. An implicit assumption throughout this analysis is that the electric potential minimum is located at the cathode. Since the anode is held at a positive potential with respect to the cathode, the electric field cannot be positive at the surface, i.e., $\eta'(0) < 0$. If this were so, the electric potential would have an inflection point within the gap. At this point, the electric field would be zero and a virtual cathode would exist, reflecting a portion of the injected electrons. Since only particles with positive velocities (toward the anode) are considered, the present analysis breaks down. Therefore, the value of the electric field at the cathode provides a convenient measure of the degree of space-charge saturation in the gap. Figure 1.1 illustrates the effect of the surface electric field on the electric potential profile. If the surface electric field is negative, $\eta'(0) > 0$, there is insufficient space-charge to limit the particle flow. If the electric field is zero at the surface, $\eta'(0) = 0$, the particle flow is space-charge limited. In this case, $j = 1$ and the current density equals that given by the Child-Langmuir law, Eq. (1.4). If the electric field is positive at the surface, $\eta'(0) < 0$, the particle flow is called space-charge saturated. For this case, a virtual cathode forms in front of the cathode and the effect of the reflected particles must be considered. Although a time-independent

analysis of this case has been made,[13] a rigorous treatment would include temporal effects. However, the mathematical difficulties in such an approach restrict such a treatment to numerical modeling or particle simulation.

History of Space-Charge Limited Current

The first published accounts of SCL currents is due to Child[14] in 1911 and Langmuir[15,16] a few years later, who investigated the current flow between planar electrodes with a potential difference insufficient to saturate the region. Neglecting the effect of initial velocity, they found that the maximum current that would flow between the electrodes varied as the three halves power of the gap potential. This relationship between the current and potential is known as the Child-Langmuir law. The effects of small initial velocity were investigated by Langmuir[17] and later by Langmuir and Compton[18] assuming a Maxwellian distribution of initial velocities. Each study found only minor corrections to the Child-Langmuir law. Extending to larger initial velocity, Gill[19] discovered qualitatively new behavior, including hysteresis between the transmitted and injected currents. Gill found that as the injected current increases past the space-charge limit, the transmitted current continues to decreases. If the injected current is then steadily decreased, the transmitted current increases but does not reach the SCL current value. In 1944, Knipp[20] presented a more complete version of the classical solution by including the space-charge of electrons reflected from the virtual cathode. The same problem was later treated by Bull.[21] Using a Maxwellian velocity distribution as well as an angular distribution of velocities, Walker[22] investigated the effects of particle deflections from the grid wires. One of the earliest treatments of axial current in cylindrical tubes was preformed by Smith and Hartmann,[23] who considered a solid beam propagating in an infinitely-long drift tube.

Hollow beams were later considered by Wax[24] and Brewer.[25] Solutions for finite radius beams travelling in finite length drift tubes were presented by Bridges, Frey and Birdsall in 1965.[26] With the development and wide-spread use of solid-state devices, the interest in vacuum tubes, as well as research into limiting currents, declined.

More recently, increased interest in HPM devices caused a revival in the desire to accurately predict the SCL current in vacuum and plasma-filled devices. This change in application led to a significant change in the approach to estimating the limiting current. Most diodes, and the like, employ non-relativistic beams. In the pursuit of high-power microwave output, HPM researchers use electrons beams with the highest possible energy. Thus, relativistics effects must be considered in analyzing the space-charge limiting current. The first exact treatment of the relativistic Child-Langmuir problem was given by Jory and Trivelpiece in 1969.[27] They considered a one-dimensional planar diode with a cold, mono-energetic beam of electrons injected from the cathode. Using elliptic integrals, they developed an analytic expression for the limiting current that reduces to the Child-Langmuir law in the non-relativistic regime. Recently, temperature effects were included in both a non-relativistic[28] and a relativistic[29] extension to the Child-Langmuir law. Unfortunately, the resulting equations had to be numerically solved.

Since most HPM devices use cylindrical or toroidal drift spaces, the need for formulas that considered more than one dimension increased. Unfortunately, self-consistently solving Poisson's equation for SCL flow for anything other than a one-dimensional planar problem requires a numerical approach. Bogdankevich and Rukhadze considered finite-length effects for electron beams in hollow drift tubes. Using a linearization of the two-fluid hydrodynamic equations, they investigated the stability

of both uncompensated and compensated (filling the drift tube with positive ions to reduce the electron space-charge) beams.[30] Later, Voronin *et al.*[31] devised a method to estimate the SCL current, including length-effects. Their approach used Green's second identity to correlate the SCL problem to a two-dimensional Sturm-Liouville eigenvalue problem, which is easily solved by elementary methods. Another benefit to their approach is the facility with which it can be generalized to more general cases. Genoni and Proctor[32] utilized this method to investigate electron beams of arbitrary radius in hollow drift tubes. Since many present-day HPM devices (such as backward-wave oscillators, magnetically insulated line oscillators, etc..) employ coaxial drift space, Stephens and Ordonez extended the theory to annular beams in finite-length coaxial drift tubes, presenting an analytic formula for estimating the SCL current.[33] Another important consideration in analyzing limiting currents in HPM devices is the gyromotion of the beam particles. Drobot and Kim investigated both cylindrical and strip beams (between infinite planar electrodes) and found that the transverse motion of the beam particles reduced the limiting current below that predicted by considering only the axial velocities.[34] The interaction between the electromagnetic waves and electron beam present in gyro-devices (gyrotron, gyro-backward-wave oscillator, etc.) has recently been investigated via computer cimulation by Spencer *et al.*.[3] As a final note, research of limiting currents in solid state materials is becoming another driving force into the understanding of space-charge limited flow.

Overview

The current work discusses space-charge limitations in cylindrical drift tubes and planar sheaths. As mentioned for cylindrical drift tubes, the space-charge present in a plasma sheath also places limitations on the current magnitude that can be

passed through a plasma sheath. Although additional complications arise from the multiple species contributing to the space-charge and the need to self-consistently solve for the potential simply to predict the sheath extent, similar ideas apply to both problems. Chapter 2 discusses approximate techniques to estimate the space-charge limited current in coaxial drift tubes. It first presents a review of the infinite-length approximation, an approach suitable to situations when the drift tube is much longer than the tube radius. It then considers the same configurations but including finite-length effects by extending a theory that estimates an upper bound to the limiting current. The remaining chapters apply to planar sheaths, of which an overview and historical sketch appear in Chap. 3. A theoretical investigation of the planar sheath is presented in Chap. 4. After developing the essential distribution functions, particle densities and fluxes for three sheath electric potential profiles, boundary conditions are applied to derive a set of nonlinear equations describing the electric potential at certain locations within the sheath. To avoid the necessity of solving these nonlinear systems, approximate expressions for the potential are provided to simplify predicting the value of the electric potential. The chapter then concludes with a discussion of the effects of the plasma and surface parameters on the plasma sheath. Finally, Chap. 5 discusses the problem of current limitations with the sheath.

REFERENCES

[1]J. Benford and J. Swagle, *High-Power Microwaves*, Artech House, Boston, MA, 1992.

[2]S. H. Gold and G. S. Nusinovich, "Review of High-Power Microwave Source Research," Rev. Sci. Instrum. **68**, 3945 (1997).

[3]T. A. Spencer, J. J. Hendricks, J. W. Luginsland, and M. D. Stump, "Dynamics of the Space-Charge-Limiting Current in Gyro-Type Devices," IEEE Trans. Plasma Science **26**, 854 (1998).

[4]D. G. Colombant and Y. Y. Lau, "Nonlinear Beam Loading and Dynamical Limiting Currents in a High-Power Microwave Gap," Phys. Rev. Lett. **64**, 2320 (1990).

[5]C. Litwin and R. Rosner, "Relativistic Space-Charge Limited Bipolar Flow," Phys. Rev. E **58**, 1163 (1998).

[6]Y. N. Gartstein and P. S. Ramesh, "Hysteresis and Self-Sustained Oscillations in Space Charge Limited Currents," J. Appl. Phys **83**, 2958 (1998).

[7]M. Mücke, R. Rao, R. Becker, and M. Kleinod, "Study of the Feasibility of Self Focusing of a Relativistic Electron Beam in an Electron Beam Ion Source/Trap," Rev. Sci. Instrum. **69**, 691 (1998).

[8]A. Kponou et al., "Simulation of 10 A Electron-Beam Formation and Collection for a High Current Electron-Beam Ion Source," Rev. Sci. Instrum. **69**, 1120 (1998).

[9]K. F. Stephens, II, C. A. Ordonez, and R. E. Peterkin, Jr., "Virtual Cathode Formations in Nested-Well Configurations," in *Non-Neutral Plasma Physics III*, edited by J. J. Bollinger, R. L. Spencer, and R. C. Davidson (American Institue of Physics, Melville, N. Y., 1999), page 451.

[10]K. L. Jensen, M. A. Kodis, R. A. Murphy, and E. G. Zaidman, "Space Charge Effects on the Current-Voltage Characteristics of Gated Field Emitter Arrays," J. Appl. Phys **82**, 845 (1997).

[11]W. W. Destler, L. E. Floyd, and M. Reiser, "Collective Acceleration of Heavy Ions," Phys. Rev. Lett. **44**, 70 (1980).

[12]P. G. O'Shea, W. W. Destler, J. Rodgers, and Z. Segalov, "Laser-Controlled Collective Ion Accelerator," Appl. Phys. Lett. **49**, 1696 (1986).

[13]C. K. Birdsall and W. B. Bridges, *Electron Dynamics of Diode Regions*, Academic Press, New York, 1966.

[14]C. Langmuir, "Discharge from Hot CaO," Phys. Rev. **32**, 492 (1911).

[15]I. Langmuir, "The Effect of Space Charge and Residual Gases on Thermionic Currents in High Vacuum," Phys. Rev. **2**, 450 (1913).

[16]I. Langmuir, Phys. Zeitschr. **15**, 348 (1914).

[17]I. Langmuir, "The Effect of Space Charge and Initial Velocities on the Potential Distribution and Rhermionic Current between Parallel Plane Electrodes," Phys. Rev. **21**, 419 (1923).

[18]I. Langmuir and K. T. Compton, Rev. Mod. Phys. **3**, 191 (1931).

[19]E. W. B. Gill, Philos. Mag. **49**, 993 (1925).

[20]J. K. Knipp, "Space-Charge Between Parallel Plane Grids," Radiation Lab. Rept. 534 (1944).

[21]C. S. Bull, "Space-Charge Effects in Beam Tetrodes and Other Valves," J. I. E. E., Part III **95**, 17 (1948).

[22]G. B. Walker, "Space-Charge Effects Between a Positive Grid and Anode of a Beam Tetrode," Wireless Engineer **22**, 157 (1945).

[23]L. P. Smith and P. L. Hartman, "The Formation and Maintenance of Electron and Ion Beams," J. Appl. Phys. **11**, 220 (1940).

[24]N. Wax, "Some Properties of Tubular Electron Beams," J. Appl. Phys. **20**, 242 (1949).

[25]G. R. Brewer, "Graphs of the Space-Charge Depression of Potential in a Cylindrical Electron Beam," Etl Memorandum 55-26, Hughes Aircraft Company, Culver City, CA, 1955.

[26]W. B. Bridges, J. I. Frey, and C. K. Birdsall, "Limiting Stable Currents in Bounded Electron and Ion Streams," I. E. E. E. Trans. Electron Devices **ED-12**, 264 (1965).

[27]H. R. Jory and A. W. Trivelpiece, J. Appl. Phys. **40**, 3924 (1969).

[28]P. Martin and G. Donoso, Phys. Fluids B **1**, 247 (1989).

[29]B.-L. Qian, Y.-G. Liu, and C.-L. Li, "Both Temperature and Relativistic Effects on the Langmuir-Child Equation," Phys. Plasmas **1**, 2398 (1994).

[30]L. S. Bogdankevich and A. A. Rukhadze, "Stability of Relativistic Electron Beams in a Plasma and the Problem of Critical Currents," Sov. Phys. Usp. **14**, 163 (1971).

[31]V. S. Voronin, Y. T. Zozulaya, and A. N. Lebedev, "Self-Consistent Stationary State of a Relativistic Electron Beam in a Drift Space," Soviet Phys. Tech. Phys. **17**, 432 (1972).

[32]T. C. Genoni and W. A. Proctor, "Upper Bound for the Space-Charge Limiting Current of Annular Electron Beams," J. Plasma Phys. **23**, 129 (1980).

[33]K. F. Stephens II and C. A. Ordonez, "Upper Bound for the Space-Charge Limited Current of Relativistic Electron Beams in Finite-Length Coaxial Drift Tubes," Phys. Plasmas. **7** (2000).

[34]A. T. Drobot and K. Kim, "Space Charge Effects on the Equilibrium of Guided Electron Flow with Gyromotion," Int. J. Electronics **51**, 351 (1981).

CHAPTER 2

UPPER-BOUND FOR THE SPACE-CHARGE LIMITED CURRENT

Derivation of an exact analytic expression for the space-charge limited (SCL) current is tractable only for one-dimensional problems. The reason for this stems from the nonlinearity introduced into Poisson's equation by relating the charge and current densities to the electric potential through the conservation of energy. To illustrate this, consider finding Poisson's equation for the SCL current of an electron beam travelling down a concentric cylindrical drift tube. Let the particles be injected into the cylinder at $z = 0$ with a kinetic energy

$$(\gamma_b - 1)\, mc^2. \tag{2.1}$$

Assuming a strong axial magnetic field to inhibit radial and azimuthal motion, the current density has only an axial component and is related to the particle density, $n(r, z)$, and axial velocity, $v_z(r) = c\beta(r, z)$, according to

$$J\,(r) = -en\,(r, z)\, c\beta\,(r, z)\,. \tag{2.2}$$

In general, the current density can be a function of radius since the only restriction is that it be independent of z, which follows from conservation of charge. Conservation of energy then relates the injected beam kinetic energy to the energy at any position downstream of the injection plane according to

$$\gamma_b = \gamma\,(r, z) - \frac{e}{mc^2}\phi\,(r, z)\,. \tag{2.3}$$

Using the relation between the relativistic mass factor and the axial velocity,

$$\gamma\left(r,z\right)=\sqrt{\frac{1}{1-\beta^{2}\left(r,z\right)}}, \tag{2.4}$$

the charge density can be expressed in terms of the electric potential by

$$\begin{aligned} -en\left(r,z\right) &= \frac{J\left(r\right)}{c\beta\left(r,z\right)} \\ &= \frac{J\left(r\right)}{c}\frac{\gamma_{b}+\Phi\left(r,z\right)}{\sqrt{\left[\gamma_{b}+\Phi\left(r,z\right)\right]^{2}-1}}, \end{aligned} \tag{2.5}$$

where the normalized potential, $\Phi(r,z)=e\phi(r,z)/mc^{2}$, is introduced. Using cgs-units, Poisson's equation can now be written as

$$\begin{aligned} \nabla^{2}\Phi\left(r,z\right) &= -4\pi\frac{e^{2}}{mc^{2}}n\left(r,z\right) \\ &= 4\pi\frac{J\left(r\right)}{I_{A}}\frac{\gamma_{b}+\Phi\left(r,z\right)}{\sqrt{\left[\gamma_{b}+\Phi\left(r,z\right)\right]^{2}-1}}, \end{aligned} \tag{2.6}$$

with $I_{A}=mc^{3}/e$ the Alfvén current. Equation (2.6) is clearly a highly nonlinear partial differential equation. If the radial dimension is neglected, a self-consistent solution is available.[1] In general, however, an exact analytic solution has not been found for Eq. (2.6). Thus, analysis of the SCL problem in two or three dimesions has been relegated to numerical solution or particle simulations. If an analytic expression is desired, various approximation methods are available. In particular, this chapter reviews the infinite-length approximation for electron beams propagating in coaxial drift tubes and investigates estimating an upper bound for the SCL current, including length effects.

The approach used here was first developed by Voronin *et al.*[2] for an electron beam travelling in and completely filling a hollow cylindrical drift tube. Using Green's second theorem, solving Poisson's equation is transferred to solving a linear eigenvalue boundary value problem. Genoni and Proctor later extended the method to

include solid and annular beams of arbitrary radius.[3] This chapter extends the theory to include coaxial drift tubes. After reviewing the infinite-length approximation, expressions for the SCL current are presented for various beam and drift tube geometries under the infinite-length approximation. The essential theory for estimating an upper-bound for the SCL current is then presented, followed by the general solution of the associated eigenvalue problem. Using the developed theory, specific examples for the SCL current upper-bound are then given for hollow and coaxial tubes. The chapter concludes with a summary of the results.

Space-Charge Limited Current in the Infinite-Length Approximation

Due to the complexity of solving Eq. (2.6), a standard approximation is to neglect axial variations so that only the radial dimension is of concern. This approach provides a realistic model if the drift tube length is much larger than the drift tube radius. Neglecting axial variations, Poisson's equation becomes

$$\frac{1}{r}\frac{d}{dr}r\frac{d\Phi\left(r\right)}{dr}=4\pi\frac{J\left(r\right)}{I_{A}}\frac{\gamma_{b}+\Phi\left(r\right)}{\sqrt{\left[\gamma_{b}+\Phi\left(r\right)\right]^{2}-1}}. \tag{2.7}$$

This differential equation is still quite nonlinear and exact analytic solutions are not known. Typically the problem is not solved self-consistently but a uniform charge density is assumed. However, a useful relation can be self-consistently obtained from this equation by considering a simple charge density profile. In particular, assume the electron beam is injected with the following current density profile:

$$J\left(r\right)=-\frac{I}{2\pi r}\delta\left(r-r_{b}\right), \tag{2.8}$$

where r_b is the beam radius, I the beam current and δ the Dirac delta function. Futhermore, assume that the drift tube is composed of coaxial cylinders of radii

$r_1 \leq r_b \leq r_2$. Letting $\Phi_b = \Phi(r_b)$, Eq. (2.7) can be re-written as

$$\frac{d}{dr} r \frac{d\Phi\left(r\right)}{dr} = -2\frac{I}{I_A} \frac{\gamma_b + \Phi\left(r\right)}{\sqrt{\left[\gamma_b + \Phi\left(r\right)\right]^2 - 1}} \delta\left(r - r_b\right). \tag{2.9}$$

The solution, which is zero at r_1 and r_2 as well as continuous at r_b is

$$\Phi\left(r\right) = \Phi_b \begin{cases} \dfrac{\ln r/r_1}{\ln r_b/r_1}, & r_1 \leq r < r_b, \\ \dfrac{\ln r/r_2}{\ln r_b/r_2}, & r_b < r \leq r_2. \end{cases} \tag{2.10}$$

Note that the problem of a hollow drift tube, in lieu of a coaxial drift tube, can be obtained by letting $r_1 \to 0$ on the right-hand side so that $\Phi(r) = \Phi_b$ for $0 < r < r_b$. It remains to consider the discontinuity in the electric field across the beam. Doing so yields the self-consistent expression for the beam current as

$$I = I_A \frac{\ln r_2/r_1}{2 \ln r_1/r_b \ln r_2/r_b} F\left(\Phi_b\right), \tag{2.11}$$

where $F(\Phi_b)$ is defined according to

$$F\left(\Phi_b\right) = -\frac{\Phi_b}{\gamma_b + \Phi_b} \sqrt{\left[\gamma_b + \Phi_b\right]^2 - 1}. \tag{2.12}$$

Examining the definition of $F(\Phi_b)$ shows that it is zero whenever $\Phi_b = 0$ and $\Phi_b = 1 - \gamma_b$. Furthermore, the value of the maximum is

$$F_{\max} = \left(\gamma_b^{2/3} - 1\right)^{3/2} \tag{2.13}$$

at $\Phi_b = \gamma_b^{1/3} - \gamma_b$. Therefore, the space-charge limited current has the upper-bound value

$$I_{scl} = I_A \frac{\ln r_2/r_1}{2 \ln r_1/r_b \ln r_2/r_b} \left(\gamma_b^{2/3} - 1\right)^{3/2}. \tag{2.14}$$

Note that the SCL current is written as a (beam factor)/(geometric factor). The feature that will be used later in this section is the beam factor, $(\gamma_b^{2/3} - 1)^{3/2}$. It

is common place, particularly when working with non-relativistic beams, to replace the beam factor from the calculation with the beam factor defined here. Albeit *ad hoc*, this replacement typically increases the range of beam energy over which the expression is applicable and has the proper scaling with respect to the potential in the non-relativistic regime, i.e., $I \sim \phi^{3/2}$.

Unfortunately, a thin beam is the only case in which Eq. (2.7) can be solved for an exact analytic expression. To determine the SCL current for other beam configurations in the infinite-length approximation, a different approach is required. Thus, rather than attempt to solve the self-consistent Poisson equation, the source term is taken to be uniform over the beam cross-section. That is, the right-hand side of Eq. (2.7) is replaced with $4\pi e n_0$ which is constant across the beam cross-section and zero outside of it. Appendix A solves Poisson's equation for the general problem of a piece-wise, constant source term bounded by coaxial, grounded cylinders.

For an electron beam with a uniform cross-section, the current, I, and current density, $J = -en_0v$, are related by $I = J \cdot A$, where $A = \pi(r_o^2 - r_i^2)$ is the cross-sectional area for a beam with inner radius r_i and outer radius r_o. From the results of Appendix A, it is found that the potential can be written as the product of the uniform charge density and a geometric function, $\phi(r) = en_0 g(r)$. Conservation of energy relates the electric potential to the beam energy as $-e\phi = (\gamma_b - \gamma)mc^2$. Letting $g_{\max}$ represent the maximum value of $g(r)$, the SCL current is found to be

$$I_{scl} = I_A \beta \left(\gamma_b - 1\right) \frac{A}{g_{\max}}, \tag{2.15}$$

where $\beta = v/c$. As previously mentioned, the range of validity of this expression can

be extended by replacing $\beta(\gamma_b - 1)$. Thus, the SCL current is taken to be

$$I_{scl} = I_A \left(\gamma_b^{2/3} - 1\right)^{3/2} \frac{A}{g_{\max}}. \tag{2.16}$$

Thus, the problem of estimating the SCL current in the infinite-length approximation reduces to determining the value of the geometric factor, $g_{\max}$, for a given beam and drift tube geometry.

Expressions for the Space-Charge Limited Current in the Infinite-Length Approximation

Having developed an expression for the space-charge limited current within the infinite-length approximation, this section uses that result for various beam and drift tube geometries. Appendix A considers Poisson's equation for a piece-wise constant potential in order to model the uniform cross-section beam. After solving Poisson's equation for the geometric function, it is found that the maximum value is given by

$$g_{\max} = \frac{a_0}{2} \ln \frac{a_0}{2\pi r_2^2} + \pi \left(r_o^2 - \frac{a_0}{2\pi}\right) - 2\pi r_o^2 \ln \frac{r_o}{r_2}, \tag{2.17}$$

where the constant a_0 is given by

$$a_0 = -\frac{2\pi \left(r_o^2 - r_i^2\right)}{\ln\left(r_1/r_2\right)} \left[\frac{1}{2} - \ln \frac{r_o}{r_2} + \frac{r_i^2}{r_o^2 - r_i^2} \left(\ln \frac{r_o}{r_2} - \ln \frac{r_i}{r_1}\right)\right]. \tag{2.18}$$

Using these expressions, the SCL current for beams in hollow and coaxial drift tubes is easily determined.

To examine a hollow tube, the inner radius of the drift tube is allowed to approach zero, $r_1 \to 0$. However, the constant a_0 defined in Eq. (2.18) cannot be accurately determined without more information. Thus consider the case of a solid beam, where $r_i = r_1 \to 0$. Then the constant $a_0 = 0$ and the potential maximum, from Eq. (2.17),

is proportional to

$$\phi_{\max} \sim g_{\max} = \pi r_o^2 \left[1 - 2\ln\frac{r_o}{r_2}\right]. \tag{2.19}$$

Using this with Eq. (2.16), the space-charge limited current for a solid beam in a hollow drift tube is

$$I_{scl} = \frac{I_A}{1 - 2\ln\left(r_o/r_2\right)} \left(\gamma_b^{2/3} - 1\right)^{3/2}. \tag{2.20}$$

If the outer radius of the beam approaches the outer cylinder radius, $r_o \to r_2$, the case of a full beam is obtained. In this case, $a_0 = 0$ and $g_{\max} = \pi r_2^2$. The SCL current for a full beam is then

$$I_{scl} = I_A \left(\gamma_b^{2/3} - 1\right)^{3/2}. \tag{2.21}$$

If the restriction of $r_i \to 0$ is released, then the constant a_0 has the value $2\pi r_i^2$. The potential maximum is then given by

$$\phi_{\max} \sim g_{\max} = \pi\left(r_o^2 - r_i^2\right)\left[1 - 2\ln\frac{r_i}{r_2}\right] - 2\pi r_o^2 \ln\frac{r_i}{r_o}, \tag{2.22}$$

and the space-charge limited current for an annular beam in a hollow drift tube is

$$I_{scl} = \left[1 + 2\ln\frac{r_2}{r_o} - 2\frac{r_i^2}{r_o^2 - r_i^2}\ln\frac{r_o}{r_i}\right]^{-1} \left(\gamma_b^{2/3} - 1\right)^{3/2}. \tag{2.23}$$

The case of a thin annular beam, $r_i \to r_o$, cannot be determined from this expression since the required discontinuity in the electric field is not present. However, this beam configuration was treated self-consistently in the previous section and is repeated here for convenience:

$$I_{scl} = I_A \frac{\ln\left(r_2/r_1\right)}{2\ln\left(r_1/r_b\right)\ln\left(r_2/r_b\right)} \left(\gamma_b^{2/3} - 1\right)^{3/2}. \tag{2.14}$$

For the case of a coaxial tube, no simplifications with respect to r_1 and r_2 need be made. In general for an annular beam, the constant a_0 cannot be simplified so that

the geometric factor is given by

$$g_{\max} = \frac{a_0}{2} \ln \frac{a_0}{2\pi r_2^2} + \pi \left(r_o^2 - \frac{a_0}{2\pi} \right) - 2\pi r_o^2 \ln \frac{r_o}{r_2}, \tag{2.24}$$

with a_0 given by Eq. (2.18). As for the hollow drift tube, the case of a thin annular beam cannot be determined from this expression. A full beam, however, can be handled. Letting $r_i \to r_1$ and $r_o \to r_2$ gives

$$a_0 = \frac{\pi \left(r_2^2 - r_1^2 \right)}{\ln \left(r_2 / r_1 \right)}. \tag{2.25}$$

The geometric factor then becomes, after some simplification,

$$g_{\max} = \frac{\pi \left(r_2^2 - r_1^2 \right)}{2 \ln \left(r_1 / r_2 \right)} \left[1 + \frac{2 r_2^2}{r_2^2 - r_1^2} - \ln \frac{r_2^2 - r_1^2}{2 r_2^2 \ln \left(r_2 / r_1 \right)} \right]. \tag{2.26}$$

The space-charge limited current for a full annular beam can then be written in terms of the ratio of cylinder radii, $\rho = r_1 / r_2$, as

$$I_{scl} = \frac{I_A}{\ln \rho} \left[1 + \frac{2}{1 - \rho^2} \ln \rho - \ln \frac{\rho^2 - 1}{2 \ln \rho} \right]^{-1} \left(\gamma_b^{2/3} - 1 \right)^{3/2}. \tag{2.27}$$

Upper Bound for the SCL Current

The general problem geometry consists of concentric, cylindrical conductors of length L with the inner conductor at radius r_1 and outer conductor at radius r_2. The cylinders are capped with an anode foil at $z = 0$ and a collector plate at $z = L$. All boundaries are grounded. An annular electron beam of inner radius r_i and outer radius r_o is emitted from the foil with a uniform density and travels to the collector plate. To prevent radial or azimuthal motion, a strong, axial magnetic field is externally applied. The magnetic self-field of the beam is neglected. Equation (2.6) can be modified for a uniform beam with current I_0 to yield

$$\left[\frac{1}{r} \frac{\partial}{\partial r} r \frac{\partial}{\partial r} + \frac{\partial^2}{\partial z^2} \right] \Phi \left(r, z \right) = \begin{cases} \dfrac{K}{\beta \left(r, z \right)}, & r_i \le r \le r_o,\ 0 \le z \le L, \\ 0, & \text{otherwise.} \end{cases} \tag{2.28}$$

subject to the boundary conditions

$$\begin{aligned} \Phi(r,0) = \Phi(r,L) &= 0, \qquad r_1 \le r \le r_2, \\ \Phi(r_1,z) = \Phi(r_2,z) &= 0, \qquad 0 \le z \le L. \end{aligned} \tag{2.29}$$

The constant K is given by

$$K = \frac{4}{r_o^2 - r_i^2}\frac{I_0}{I_A}, \tag{2.30}$$

and $\beta(r,z)$ is found from Eq. (2.5) to be

$$\beta(r,z) = \frac{\sqrt{[\gamma_b + \Phi(r,z)]^2 - 1}}{\gamma_b + \Phi(r,z)}. \tag{2.31}$$

Note that the beam radii explicitly appear in the constant K. This implies another assumption of this theory: the beam must maintain a constant cross-section. However, this assumption is implicitly stated by the presence of the infinitely strong magnetic field. Since the field inhibits all radial motion, the beam cannot diverge or constrict. Therefore, the cross-section will remain constant.

To determine the upper bound estimate for the SCL current, Green's second identity is applied to the region occupied by the beam,

$$\underbrace{\int_V \left[\psi\nabla^2\Phi - \Phi\nabla^2\psi\right] dv}_{\tau} = \underbrace{\oint_S \left[\psi\frac{\partial\Phi}{\partial n} - \Phi\frac{\partial\psi}{\partial n}\right] ds}_{\Sigma}. \tag{2.32}$$

The underbraces indicate that τ equals the volume integral and Σ the surface integral. The function Φ is the normalized electric potential satisfying Eqs. (2.28) and (2.29) and the function ψ satisfies the eignenvalue problem defined by

$$\nabla^2\psi(r,z) = \Lambda\psi(r,z), \qquad r_i \le r \le r_o, 0 \le z \le L, \tag{2.33}$$

and subject to the boundary conditions

$$\begin{aligned} \psi(r,0) = \psi(r,L) = 0, \qquad & r_i \le r \le r_o, \\ a_1 r_i \left.\frac{\partial \psi(r,z)}{\partial r}\right|_{r=r_i} - a_2 \psi(r_i,z) = 0, \qquad & 0 \le z \le L, \\ b_1 r_o \left.\frac{\partial \psi(r,z)}{\partial r}\right|_{r=r_o} - b_2 \psi(r_o,z) = 0, \qquad & 0 \le z \le L. \end{aligned} \tag{2.34}$$

The constants a_1, a_2, b_1 and b_2 are determined in the next section such that

1) the surface integral Σ in Eq. (2.32) is zero,

2) Equation (2.33) has an eigenfunction that is non-zero interior to the problem domain, and

3) The corresponding eigenvalue is negative.

Assuming that these conditions are met, then the volume integral must also be zero:

$$\tau = 2\pi \int_0^L \int_{r_i}^{r_o} \left[\frac{K}{\beta(r,z)} - \Lambda_0 \Phi(r,z) \right] \psi(r,z)\, r dr dz = 0, \tag{2.35}$$

where Λ_0 is the fundamental eigenvalue for the associated eigenvalue boundary value problem. Since $\psi(r,z)$ can only be zero along the boundaries, the integrand in square brackets must change sign during the integration in order that the volume integral be zero. Denoting the point where the argument in square brackets is zero by (r',z'), the constant K at this point is

$$K = |\Lambda_0| \beta(r',z') \Phi(r',z'). \tag{2.36}$$

Since there is no source of energy to the beam particles within the drift tube, the fact that $1 < \gamma(r',z') < \gamma_b$ implies that

$$\beta(r',z') \Phi(r',z') = \sqrt{1 - \frac{1}{\gamma^2(r',z')}} \left[\gamma_b - \gamma(r',z') \right] \tag{2.37}$$

cannot exceed the value $(\gamma_0^{2/3} - 1)^{3/2}$. This value is determined by setting the derivative of $\beta(r',z')\Phi(r',z')$ with respect to $\gamma(r',z')$ equal to zero and solving for the root.

Therefore, since the right-hand side of Eq. (2.36) has an upper bound, so does $K \sim I_0$. Inserting the value of K from Eq. (2.30) and solving for I_0 gives the upper bound estimate for the SCL current as

$$I_0 \leq I_{ub} \equiv \frac{r_o^2 - r_i^2}{4} I_A |\Lambda_0| \left(\gamma_b^{2/3} - 1\right)^{3/2}. \tag{2.38}$$

Determining an expression for I_{ub} is dependent upon solving the linear eigenvalue problem defined by Eqs. (2.33) and (2.34). The general solution for this boundary value problem is developed in the next section.

General Solution of the Associated Eigenvalue Problem

To validate the expression for the upper bound SCL current, the assumption that the surface integral in Eq. (2.32) is zero must now be shown true. This will be accomplished by choosing appropriate values for the constants a_1, a_2, b_1 and b_2 in Eq. (2.34). These values must correspond to a solution Λ_0, ψ_0 of the eigenvalue problem where Λ_0 is negative and ψ_0 is zero only on the boundaries. The eigenfunction can be determined from separation of variables to be of the form

$$\psi_0 (r, z) = \rho (r) \sin (\kappa_1 z), \tag{2.39}$$

where $\kappa_n = n\pi/L$; this form automatically satisfies the boundary conditions at the ends. Inserting this function into the surface integral yields

$$\Sigma = 2\pi\xi \int_0^L \left[\rho (\xi) \left. \frac{\partial \Phi (r, z)}{\partial r} \right|_{r=\xi} - \Phi (\xi, z) \left. \frac{d\rho (r)}{dr} \right|_{r=\xi} \right] \sin (\kappa_1 z)\, dz \Bigg|_{\xi=r_i}^{r_o}. \tag{2.40}$$

The lower and upper limits on ξ represent the contributions from the inner and outer conducters to the surface integral.

Considering only the charge-free regions, the solution to Eq. (2.28) can be written as

$$\Phi(r,z) = \begin{cases} \sum_{n=1}^{\infty} A_n g_n(r,r_1)\sin(\kappa_n r), & r_1 \le r \le r_i, \\ \sum_{n=1}^{\infty} B_n g_n(r,r_2)\sin(\kappa_n r), & r_o \le r \le r_2, \end{cases} \tag{2.41}$$

where

$$g_n(r,r') = I_0(\kappa_n r) - \frac{I_0(\kappa_n r')}{K_0(\kappa_n r')} K_0(\kappa_n r). \tag{2.42}$$

Here, I_0 and K_0 are the modified Bessel functions of the first and second kind, respectively, of order zero. It is clear that $g_n(r,r_1)$ and $g_n(r,r_2)$ automatically satisfy the boundary conditions at r_1 and r_2. Furthermore, $g_n(r,r')$ reduces to the proper solution when $r_1 \to 0$.

The differential equation for $\rho(r)$ can be determined by substituting from Eqs. (2.39) and (2.41) into Eq. (2.40). With this, it is found that the surface integral, Σ, is zero if $\rho(r)$ non-trivially satisfies the eigenvalue problem defined by

$$\frac{d}{dr} r \frac{d\rho(r)}{dr} + \lambda r \rho(r) = 0, \qquad r_i \le r \le r_o, \tag{2.43}$$

with the boundary conditions

$$\begin{aligned} a_1 r_i \rho'(r_i) - a_2 \rho(r_i) &= 0, \\ b_1 r_o \rho'(r_o) - b_2 \rho(r_o) &= 0. \end{aligned} \tag{2.44}$$

The coefficients in Eq. (2.44) are given by

$$\begin{aligned} a_1 &= g_1(r_i,r_1), & b_1 &= g_1(r_o,r_2), \\ a_2 &= r_i \left.\frac{dg_1(r,r_1)}{dr}\right|_{r=r_i}, & b_2 &= r_o \left.\frac{dg_1(r,r_2)}{dr}\right|_{r=r_o}. \end{aligned} \tag{2.45}$$

Since $I_\nu(z)$ ($K_\nu(z)$) is a monotonically increasing (decreasing) function of z for real arguments, one can show that the coefficient b_1 is negative while the other coefficients are positive by using the fact that $r_1 \le r_i$ and $r_2 \ge r_o$.

Noting that the differential equation for $\rho(r)$ is Bessel's equation of order zero, the solution can be written

$$\rho\left(r\right) = J_0\left(kr\right) + C\left(k\right) N_0\left(kr\right), \tag{2.46}$$

where $k^2 = \lambda_0$ and J_0 (N_0) is the order zero Bessel function of the first (second) kind. Applying the boundary conditions given in Eq. (2.44), the coefficient $C(k)$ and eigenvalue k are determined from the nonlinear system

$$\begin{aligned} &a_2\left[J_0\left(kr_i\right) + C\left(k\right) N_0\left(kr_i\right)\right] + a_1 kr_i\left[J_1\left(kr_i\right) + C\left(k\right) N_1\left(kr_i\right)\right] = 0, \\ &b_2\left[J_0\left(kr_o\right) + C\left(k\right) N_0\left(kr_o\right)\right] + b_1 kr_i\left[J_1\left(kr_o\right) + C\left(k\right) N_1\left(kr_o\right)\right] = 0. \end{aligned} \tag{2.47}$$

Since the value of $C(k)$ is not always necessary for determining the SCL current upper-bound, a single equation for k is given by

$$\frac{a_2 J_0\left(kr_i\right) + a_1 kr_i J_1\left(kr_i\right)}{a_2 N_0\left(kr_i\right) + a_1 kr_i N_1\left(kr_i\right)} = \frac{b_2 J_0\left(kr_o\right) + b_1 kr_o J_1\left(kr_o\right)}{b_2 N_0\left(kr_o\right) + b_1 kr_o N_1\left(kr_o\right)}, \tag{2.48}$$

where the coefficients a and b in Eq. (2.48) are defined in Eq. (2.45). For cases when $C(k)$ is zero, e.g., a hollow drift tube, Eq. (2.47) must be used. Once Eq. (2.47) or (2.48) is solved for k, the expression for the SCL current upper bound is given by

$$I_{ub} = I_A \frac{r_o^2 - r_i^2}{4}\left[k^2 + \kappa_1^2\right]\left(\gamma_b^{2/3} - 1\right)^{3/2}. \tag{2.49}$$

SCL Upper Bound for Hollow Drift Tubes

Having determined the form of the SCL current upper bound, its remains to determine how the upper bound depends upon the geometry. This is accomplished by solving the determinantal equation, Eq. (2.47), for the eigenvalue k for the specific geometry at hand. This section investigates various cases of hollow drift tubes, i.e., $r_1 = 0$. When the inner conductor is absent, the boundary condition coefficients a_1

and a_2 defined in Eq. (2.45) must be modified since the Bessel function K_0 logarithmically diverges at the origin. In this case, these coefficients become

$$\begin{aligned} a_1 &\to I_0\left(\kappa_1 r_i\right), \\ a_2 &\to \kappa_1 r_i I_1\left(\kappa_1 r_i\right). \end{aligned} \tag{2.50}$$

With these modifications, various beam geometries in a hollow drift tube can be considered.

Solid Beam

For a solid beam, the inner radius is zero, $r_i = 0$. The parameter $C(k)$ in the radial solution of the associated eigenvalue problem, Eq. (2.46), must be zero to avoid the divergent N_0 at the origin. Setting $C(k) = r_i = 0$ in Eq. (2.48) gives the determinantal equation for a solid beam in a hollow drift tube to be

$$J_0\left(kr_o\right) + \frac{b_1}{b_2} kr_o J_1\left(kr_o\right) = 0. \tag{2.51}$$

Without further simplifying assumptions, Eq. (2.51) is a transcendental equation for k and must be numerically solved to determined the SCL current upper bound.

Full Solid Beam

If the beam completely fills the drift tubes, i.e., a full beam, then the outer radius of the beam coincides with the drift tube wall, $r_o = r_2$, and Eq. (2.51) can be simplified. If r_o is set equal to r_2 in the coefficients b_1 and b_2, it is found that $b_1 = g_1(r_2, r_2) = 0$ while b_2 remains non-zero. Therefore, the determinantal equation becomes

$$J_0\left(kr_2\right) = 0. \tag{2.52}$$

This equation is satisfied if k/r_2 equals the lowest root of J_0. Therefore, the upper bound for the SCL current of a full solid beam in a hollow drift tube is

$$I_{ub} = \frac{I_A}{4}\left[(2.405)^2 + \left(\frac{\pi r_2}{L}\right)^2\right]\left(\gamma_b^{2/3} - 1\right)^{3/2}. \tag{2.53}$$

This result was given in Voronin *et al.*[2] by using the same method.

Thin Solid Beam

The next beam geometry in a hollow drift tube which leads to an algebraic expression for the SCL current upper bound is a thin beam. For a thin beam, the inner beam radius, r_i, is again allowed to approach zero while the length of the tube is increased until it is much larger than the tube radius, $r_2/L \ll 1$. If this limit is applied to the coefficients b_1 and b_2 defined in Eq. (2.45) and the small argument expansion of the modified Bessel functions is used, these coefficients reduce to

$$\frac{b_1}{b_2} \sim \ln\left(\frac{r_o}{r_2}\right). \tag{2.54}$$

If the ratio b_1/b_2 in Eq. (2.51) is replaced by this expression, the determinantal equation is written

$$J_0\left(kr_o\right) + kr_o J_1\left(kr_o\right)\ln\left(\frac{r_o}{r_2}\right) = 0. \tag{2.55}$$

Expanding the Bessel functions to fourth order in kr_o, the root to this equation is approximated by

$$\left(kr_o\right)^2 \approx \frac{8}{1 + 4\ln\left(r_2/r_o\right)}. \tag{2.56}$$

With k determined, the SCL current upper bound for a thin beam propagating in a hollow drift tube is found to be

$$I_{ub} = \frac{I_A}{\frac{1}{2} + 2\ln\left(r_2/r_o\right)}\left(\gamma_b^{2/3} - 1\right)^{3/2}. \tag{2.57}$$

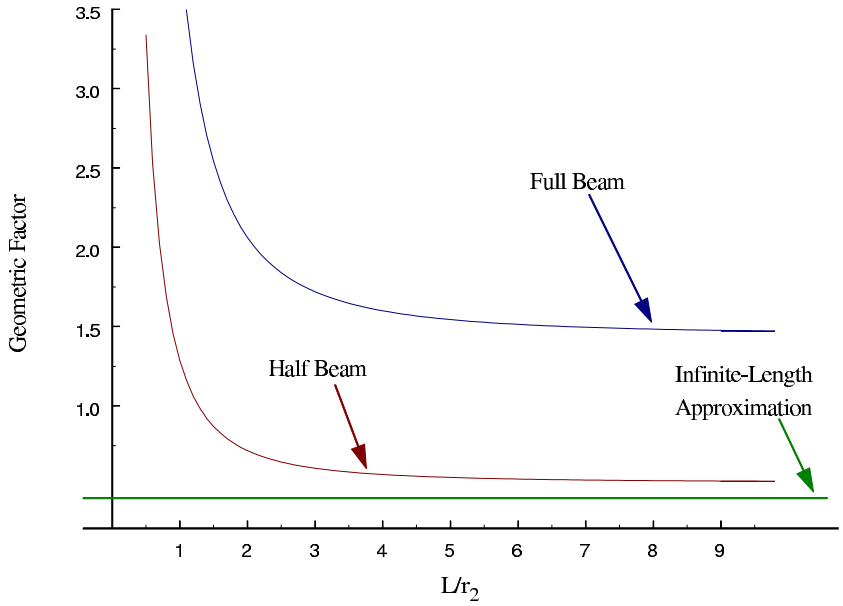

FIG. 2.1. Length effects on the geometric factor for the SCL current of solid beams propagating in a hollow drift tube of radius $r_2 = 10$ mm. The cases shown are a full beam ($r_o = r_2$), a half beam ($r_o = r_2/2$) and the value under the infinite-length approximation.

A similar expression was obtained by considering a thin beam in the infinite-length approximation,

$$I_{ub} = \frac{I_A}{1 + 2\ln\left(r_2/r_o\right)} \left(\gamma_b^{2/3} - 1\right)^{3/2} . \tag{2.20}$$

Comparing these two expressions, it is clear that a finite-length places a higher upper bound on the SCL current compared to the case when finite-length effects are not considered. The finite-length effect is demonstrated in Fig. 2.1, which shows the geometric factor for different beam configurations in a hollow drift tube of radius $r_2 = 10$ mm. Obviously, the full solid beam can propagate a larger current due to the larger cross-section and is always approximately three times the half beam current. Neither the half nor full solid beam ever approach the value predicted by the infinite-length approximation, as discussed above. However, they do approach the values

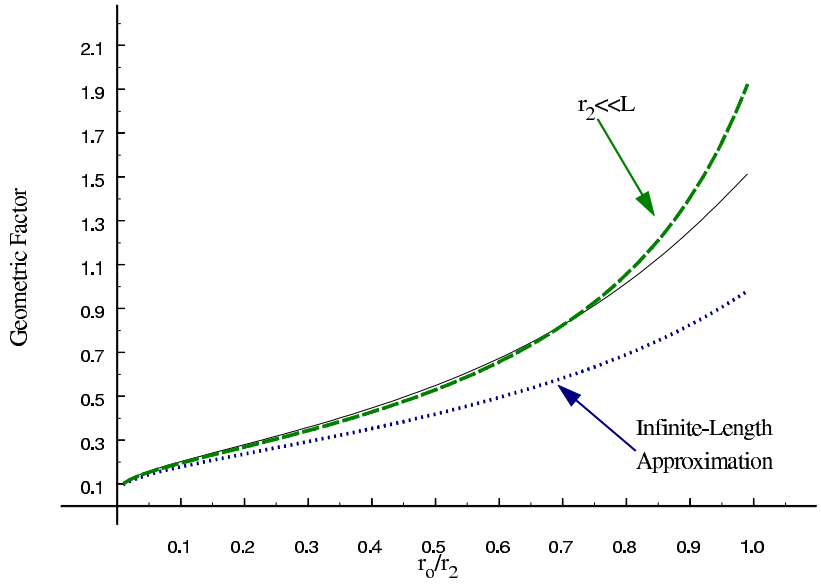

FIG. 2.2. Effect of beam radius on solid beams propagating in a hollow drift tube of radius $r_2 = 10$ mm and length $L = 50$ mm. The thin beam approximation, $r_2 \ll L$, agrees with the result obtained from the determinantal equation for a solid beam, Eq. (2.51). The infinite-length expression under-estimates the finite-length expressions.

predicted by Eq. (2.57).

The effects of beam radius on solid beams is illustrated in Fig. 2.2, for a drift tube of radius $r_2 = 10$ mm and $L = 50$ mm. The cases shown correspond to the general expression for a solid beam (where the determinantal equation, Eq. (2.51), is numerically solved), the case of a thin solid beam, Eq. (2.57), and the infinite-length approximation, Eq. (2.20). Also, the thin beam expression agrees well with the general result below $r_o \sim 0.75 r_2$.

SCL Upper Bound for Coaxial Drift Tubes

Having developed expressions for the SCL current upper bound in hollow drift tubes, this section investigates various beam geometries travelling in coaxial drift tubes. In general, Eqs. (2.47) or (2.48) must be numerically solved to determine the

eigenvalue k required in Eq. (2.49). However, for limiting cases of the beam's radii, approximations can be made to yield analytical expressions.

Thin Annular Beam

To analyze a thin beam, the inner beam radius, r_i, is replaced by $r_o(1-\delta/r_o)$, where $\delta = r_o - r_i$ is the beam thickness. The beam thickness is then allowed to go to zero. Making this substitution in Eq. (2.45) and expanding the Bessel functions to first order in δ, the boundary condition coefficients a_1 and a_2 become

$$\begin{aligned} a_1 &\approx g_1(r_o, r_1) - \kappa_1 r_o \delta g_1'(r_o, r_1), \\ a_2 &\approx \kappa_1 r_o \left[g_1'(r_o, r_1) - \kappa_1 r_o \delta g_1(r_o, r_1) \right], \end{aligned} \tag{2.58}$$

where

$$g_1'(r_o, r_1) = \left. \frac{\partial g_1(r, r_1)}{\partial r} \right|_{r=r_o}. \tag{2.59}$$

It can be shown that as the beam thickness approaches zero, the eigenvalue $k \to \infty$ while the product $k\delta$ remains finite. It is therefore reasonable to approximate the circular Bessel functions in Eq. (2.48) by the leading term of their asymptotic expansions. The result can be rearranged to give the expression

$$\cot(k\delta) = -\frac{a_2 b_2 + a_1 b_1 r_i r_o k^2}{a_1 b_2 r_i k - a_2 b_1 r_o k}. \tag{2.60}$$

The right-hand side of this expression can be further simplified by inserting the expressions from Eq. (2.58), replacing r_i with $r_o(1-\delta/r_o)$ and then taking the limit $\delta \to 0$. The leading term from the resulting expression gives

$$\cot(k\delta) \approx -\frac{b_1 r_o \left[I_0(\kappa_1 r_o) - K_0(\kappa_1 r_o) \right]}{b_1 \kappa_1^2 r_o \left[I_1(\kappa_1 r_o) + K_1(\kappa_1 r_o) \right] - b_2 \left[I_0(\kappa_1 r_o) + K_0(\kappa_1 r_o) \right]}. \tag{2.61}$$

If b_1 and b_2 are now replaced by their expressions from Eq. (2.45), the result becomes

$$\cot(k\delta) = \left[-\frac{r_o}{\delta} \frac{g_1(r_o, r_1)\, g_1(r_o, r_2)}{g_1(r_1, r_2)} K_0(\kappa_1 r_1) \right] (k\delta), \tag{2.62}$$

where the Wronskian for the modified Bessel functions was used to simplify the expression.

Examination of the right-hand side of Eq. (2.62) shows that it is a linear function of $k\delta$ whose slope increases without bound as δ approaches zero. In order for such a line to intersect $\cot(k\delta)$, it must do so for $k\delta \ll 1$. Hence, the cotangent can be replaced by the approximate expression $\cot(z) \sim 1/z$, which holds for $z \ll 1$. An explicit expression for the eigenvalue k can be written as

$$\delta r_o k^2 \sim \frac{g_1(r_1, r_2)}{g_1(r_o, r_1)\, g_1(r_o, r_2)\, K_0(\kappa_1 r_1)}. \tag{2.63}$$

In order to use this in the formula for the upper-bound, the geometric factor in Eq. (2.49) can be recast into the following form:

$$\begin{aligned} \frac{r_o^2 - r_i^2}{4}\left[k^2 + \kappa_1^2\right] &= \frac{(r_o - r_i)(r_o + r_i)}{4}\left[k^2 + \kappa_1^2\right] \\ &= \frac{\delta r_o}{2}\left[k^2 + \kappa_1^2\right]. \end{aligned} \tag{2.64}$$

Thus, the upper bound for SCL current for a thin beam propagating in a coaxial drift tube is give by

$$I_{ub} = I_A \frac{g_1(r_1, r_2)}{2 g_1(r_o, r_1)\, g_1(r_o, r_2)\, K_0(\kappa_1 r_1)} \left(\gamma_b^{2/3} - 1\right)^{3/2}. \tag{2.65}$$

Long Thin Annular Beam

As for the thin beam in the hollow drift tube, a long thin annular beam in a coaxial drift tube leads to more simplifications over the simple thin beam case. As before, for a long beam the outer tube radius is taken to be much smaller than the tube length, $r_2 \ll L$. Taking this to be true and using the small argument expansion for the modified Bessel functions in Eq. (2.65), the geometric factor for a long thin

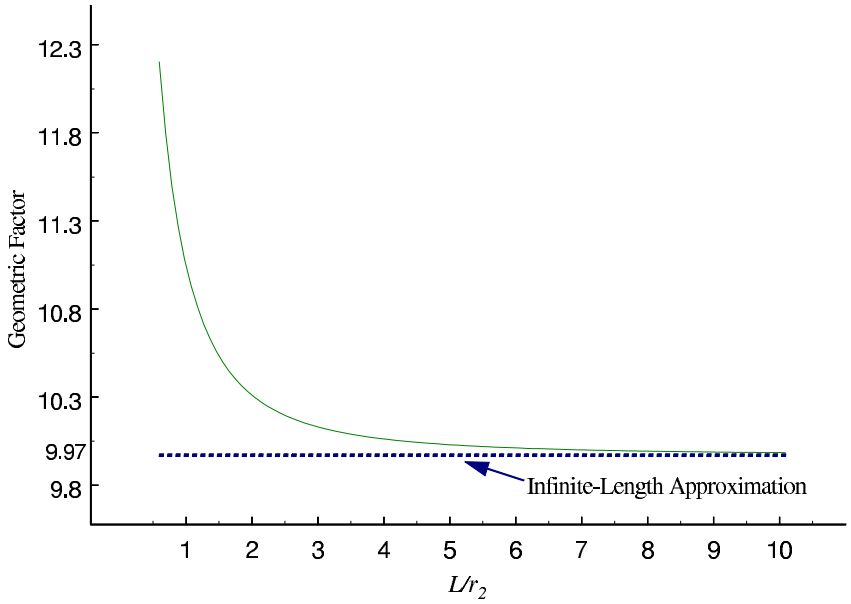

FIG. 2.3. Geometric factor for the SCL current of a long thin beam in a coaxial drift tube, Eq. (2.67). The tube radii are $r_1 = 1\,\text{mm}$ and $r_2 = 10\,\text{mm}$ with a beam radius $r_b = 9.5\,\text{mm}$. The infinite-length expression, Eq. (2.14), is shown for comparison and has the value 9.97.

beam is found to be

$$\frac{\ln\left(\frac{r_1}{r_2}\right)}{2\ln\left(\frac{r_1}{r_o}\right)\ln\left(\frac{r_o}{r_2}\right)} \tag{2.66}$$

and the upper bound for the SCL current is

$$I_{ub} = I_A \frac{\ln\left(\frac{r_1}{r_2}\right)}{2\ln\left(\frac{r_1}{r_o}\right)\ln\left(\frac{r_o}{r_2}\right)} \left(\gamma_b^{2/3} - 1\right)^{3/2}. \tag{2.67}$$

This expression exactly matches the corresponding expression obtained for a thin beam propagating in a coaxial drift tube, Eq. (2.14), based on the infinite-length approximation. Figure 2.3 shows a comparison of the geometric factor of Eqs. (2.65) and (2.67) for $r_1 = 1\,\text{mm}$, $r_2 = 10\,\text{mm}$ and $r_b = 9.5\,\text{mm}$. It is clear that as the tube length approaches ten times the gap distance (i.e., $r_2 - r_1$), the two expressions are very similar. However, the tube length at which this occurs depends upon the

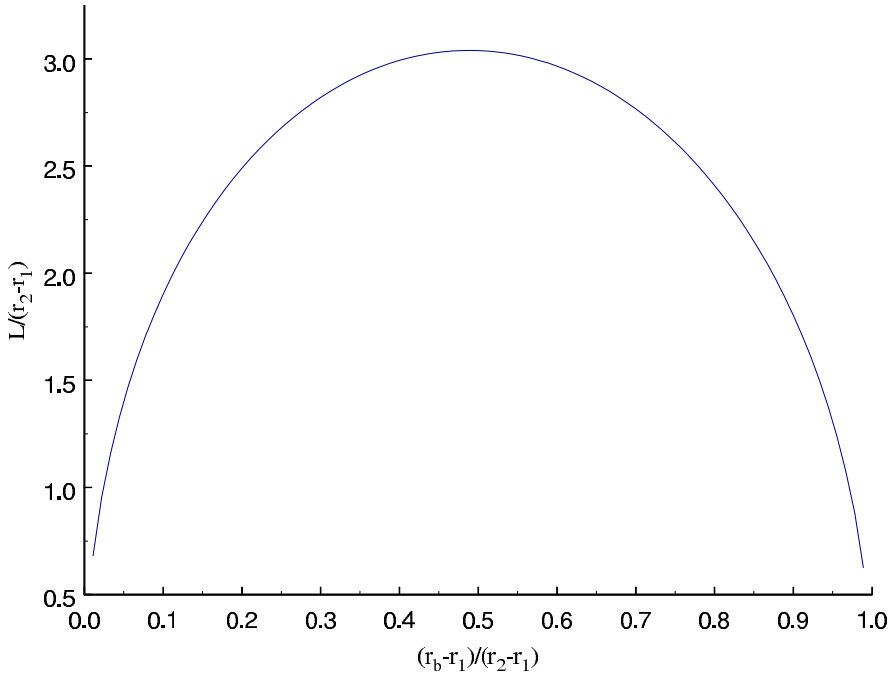

FIG. 2.4. Profile of the tube length, as a function of beam radius, for the finite-length expression and infinite-length expressions to agree within 0.1%. As the beam nears the wall, the two expressions agree for shorter tubes.

beam radius. This fact is illustrated in Fig. 2.4, which compares the tube length and beam radius for the infinite-length expression to be within 0.1% of the finite-length expression. It is clear that as the beam nears the tube walls, the necessary tube length for the two expressions to approximately agree decreases.

Full Annular Beam

As previously found, if the beam completely fills a hollow drift tube the expression for the upper bound SCL current becomes quite simple. A similar statement holds for an annular beam completely filling a coaxial drift tube. However, the presence of the inner conductor slightly complicates the analysis. If the inner and outer beam radii are set equal to the respective tube radii, $r_i = r_1$ and $r_o = r_2$, the coefficients

a_1 and b_1 in Eq. (2.45) are zero. Retaining only those terms multiplying a_2 and b_2 in Eq. (2.47), the eigenvalue k must satisfy the equation

$$J_0(kr_1)\,N_0(kr_2) - J_0(kr_2)\,N_0(kr_1) = 0. \tag{2.68}$$

This equation is a cross product of linearly independent Bessel functions. According to Eq. (9.5.27) of Abramowitz & Stegun,[4] an approximate analytical solution to this equation is available: The s^{th} root of

$$J_\nu(z)\,N_\nu(\lambda z) - J_\nu(\lambda z)\,N_\nu(z) = 0 \tag{2.69}$$

for $\lambda > 1$ is given by

$$\beta + \frac{p}{\beta} + \frac{q - p^2}{\beta^3} + \ldots, \tag{2.70}$$

where

$$\begin{gathered} \beta = \frac{s\pi}{\lambda - 1} \qquad p = \frac{4\nu^2 - 1}{8\lambda} \\ q = \frac{(4\nu^2 - 1)(4\nu^2 - 25)(\lambda^3 - 1)}{4(16\nu)^3(\lambda - 1)}. \end{gathered} \tag{2.71}$$

Taking $z = kr_1$ and $\lambda = r_2/r_1$, the lowest root of Eq. (2.68) is found to be

$$k \approx \frac{\pi}{r_2 - r_1}\frac{r_2 - r_1}{8\pi r_1 r_2}. \tag{2.72}$$

Using this value in Eq. (2.49), the upper bound SCL current for a full annular beam in a coaxial drift tube is

$$I_{ub} = I_A \frac{r_2^2 - r_1^2}{4}\left\{\left[\frac{\pi}{r_2 - r_1} - \frac{r_2 - r_1}{8\pi r_1 r_2}\right]^2 + \left[\frac{\pi}{L}\right]^2\right\}\left(\gamma_b^{2/3} - 1\right)^{3/2}. \tag{2.73}$$

Summary

One of the most important features in charged particle beam applications is the ability to accurately predict the space-charge limited current. For situations where

two or more dimensions must be considered, a self-consistent analytic expression is not available. To avoid the need of numerically solving the nonlinear Poisson equation under conditions of space-charge limited flow, approximate expressions are highly desirable. One common approach, the infinite-length approximation, considers the problem domain to be much longer than the problem radius. This method, however, avoids the key question of length effects on the current. Using Green's second identity, the nonlinear Poisson equation can be related to a linear eigenvalue problem which is easily solved as a boundary value problem. Although this theory cannot predict the exact value, it does place an upper limit on the SCL current. At its most general level, the theory applies to coaxial drift tubes and annular beams of arbitrary radius. For drift tubes whose length is more than five times the radius, it is found that the SCL current differs from that obtained by the infinite-length approximation only slightly. Furthermore, the relative length of the tube at which this occurs depends upon the location of the beam within the drift tube. As the beam nears the tube walls, the required length for the infinite-length approximation to become valid decreases.

REFERENCES

[1]H. R. Jory and A. W. Trivelpiece, J. Appl. Phys. **40**, 3924 (1969).

[2]V. S. Voronin, Y. T. Zozulaya, and A. N. Lebedev, "Self-Consistent Stationary State of a Relativistic Electron Beam in a Drift Space," Soviet Phys. Tech. Phys. **17**, 432 (1972).

[3]T. C. Genoni and W. A. Proctor, "Upper Bound for the Space-Charge Limiting Current of Annular Electron Beams," J. Plasma Phys. **23**, 129 (1980).

[4]M. Abramowitz and I. A. Stegun, editors, *Handbook of Mathematical Functions*, National Bureau of Standards, Washington, D.C., 1964.

CHAPTER 3

INTRODUCTION TO PLASMA SHEATHS

The electrostatic potential within an unbounded, neutral plasma at equilibrium is essentially constant. Such a plasma is well described by a Maxwellian velocity distribution. Even if the plasma is bounded by a material surface, far from the surface the velocity distribution is nearly Maxwellian. Near the surface, however, large electric fields develop and a Maxwellian is no longer appropriate. This region of high electric fields is known as the plasma sheath and extends several Debye lengths into the plasma. The sheath is typically divided into two regions. The region nearest the surface is called the Debye sheath, collector sheath or simply the sheath. The remaining region is entitled the presheath or source sheath. Although precisely defining the boundary between the sheath and presheath or between the presheath and bulk plasma is difficult, some qualitative statements can be made. The electric field in the sheath is typically much larger than in the presheath. Furthermore, the sheath is non-neutral and non-Maxwellian whereas the presheath is typically considered to be globally quasi-neutral.

Perhaps the closest "precise" definition of the sheath/presheath interface stems from the Bohm criterion.[1] In this interpretation, the presheath is considered as a region of slowly-varying electric potential that serves to accelerate plasma ions into the sheath. This acceleration must be sufficient that the ions reach their acoustic speed by the time they reach the sheath edge (i.e., the sheath/presheath interface). Considering a mono-energetic beam of ions, Bohm expressed this criterion as $v \geq v_s$,

where v is the ion velocity directed towards the sheath and v_s is the ion acoustic wave speed. Furthermore, this transition is also evident by a field singularity at the sheath edge, implying the transition between two regions described by vastly different length scales. The presheath is described on scales of the ion mean free path while the sheath follows scales given by the Debye length. Therefore, the sheath edge (the interface between the sheath and presheath) is determined by the position of the field singularity. From this, the presheath must extend sufficiently far into the edge plasma (the plasma extending beyond the presheath) such that the Bohm criterion is satisfied.

The two main approaches to solving the sheath problem employ either a kinetic approach or one based on the fluid equations. The fluid equations are derived by multiplying the evolution equation for the phase-space distribution function (DF), the Vlasov equation, by various powers of the velocity and then integrating over velocity space. Although these equations provide a convenient starting point, subtle details are lost due to the averaging process used to derive the equations and a complete description is not available. A theory based on the kinetic theory attempts to determine information about the phase-space DF, which contains the complete information of the system. Unfortunately, directly solving for the phase-space DF is a formidable task and an analytical result is rarely available. Some approaches obtain an integro-differential equation which can be solved in certain limiting cases but must, in general, be numerically solved. An alternative to directly solving Vlasov's equation is to consider sheaths with a particular electric potential profile and then, using the planar-source model,[2] determine the forbidden regions of phase-space. This allows the DF in the sheath (i.e., sheath and presheath) to be determined. The latter approach

is used in the present work. But before discussing that, a brief history of fully kinetic sheath theory is in order.

History of Fully Kinetic Sheath Theory

The sheath problem has been an active area of research for nearly a century. Originating in the seminal study of gaseous arc discharges by Tonks and Langmuir,[3] it has covered fields ranging from scrape-off layers and divertor plates in fusion devices,[4–6] to electronic devices and plasma processing,[7,8] plasma diagnostic probes,[9–12] and free burning arcs.[13] Because of this widespread interest, a thorough discussion of sheath theory history is beyond the scope of most works, including the present. Therefore, only an outline of the history of fully kinetic sheath theory is presented.

The first kinetic description of the sheath was given by Tonks and Langmuir,[3] who investigated the effect of probes submersed into the plasma of an arc discharge. They derived an integro-differential equation describing the electrostatic potential throughout the sheath and plasma by assuming a Maxwellian distribution for the electrons and that the ion density followed from the ionization of cold neutrals. Neglecting terms lowest-order in the Debye to system length ratio, they obtained an integral equation describing the potential distribution in the plasma up to the sheath edge. A power-series solution was then obtained for the plasma equation under various limits of the ion mean free path (compared to the system length) and ion generation methods for different geometries (planar, cylindrical and spherical). Harrison and Thompson[14] obtained an analytic solution to the plasma equation for the case of a collisionless plasma in planar geometry. An analytic solution to the plasma-sheath equation for the sheath region was obtained by Caruso and Cavaliere.[15] However, joining the sheath solution to the plasma solution is difficult because of the field

singularity at the sheath edge.[16]

Other formulations of the plasma-sheath equation have been presented by various authors. Kinetic theories that considered warm ions began appearing around 1980. Riemann[17] developed a collision-dominated counterpart to the collisionless Tonks-Langmuir model. Considering Maxwellian electrons and ions generated from the ionization of warm neutrals, Emmert *et al.*[2] found no field singularity at the sheath edge, a prevalent feature in theories restricted to cold ions. Later, Bissell and Johnson[18] investigated the same problem but, using a Maxwellian source, found the field singularity persisted for warm ions. Results from other theories[19,20] that considered warm ions also maintained the existence of the field singularity. It was later pointed out by Bissell[21] that Emmert's theory did not contain the familiar field singularity because his source function created no ions with zero velocity. Having ions born with zero velocity causes the electric field at the plasma/sheath boundary to become infinitely large to sufficiently accelerate the ions to maintain quasineutrality. The absence of such ions allows the electric field at this boundary to remain finite. Bissell also demonstrated that Emmert's theory yields a proper solution to the sheath problem by showing it satisfies the generalized Bohm criterion and concluded that the field singularity must exist if ions, born with zero velocity, are to be accelerated so that quaisneutrality is maintained.

Despite this controversial result from Emmert *et al.*, their work contained a significant contribution. Numerically solving their plasma-sheath equation for various ratios of the Debye length to system length, they demonstrated that the width of the plasma source does not affect the electric potential at the wall if this ratio is sufficiently small ($< 10^{-3}$). With this, the source region can be replaced with a planar source at

the plasma edge (i.e., the interface between tha plasma and presheath). Thus, the sheath problem can be solved by using truncated particle DFs without consideration of the source region. Use of truncated distributions predates the work by Emmert *et al.* in the field of thermionic convertors and Q-machines.[22–26] A thermionic convertor uses a hot cathode to partially ionize a neutral gas to form a plasma allowing current to flow to the anode. Depending upon the applied diode voltage and the ratio of emitted ions to electrons, a variety of stable and unstable potential profiles are possible. Auer[22] used a plane-diode model to model a low-pressure thermionic converter while characterizations of the possible profiles were presented by McIntyre.[23,24] The plane-diode model was used by Rynn[25] to model the sheaths in the end columns of a Q-machine. Considering single-ended Q-machines, Kuhn[26] investigated the equilibrium properties of "non-wavy" potential profiles, based on the categorization of stable and unstable profiles presented by Ott.[27] The collisionless, kinetic plane-diode model was later verified by particle simulation of single-emitter plasma devices (i.e., single-ended Q-machines or thermionic converters with a negatively biased collector) with a monotonically decreasing potential profile.[28] Schwager and Birdsall,[29] using the planar-source model, considered the effect of finite ion temperature on the entire sheath, citing better agreement with Emmert's[2] theory than with Bissell and Johnson's.[18]

Depending upon the properties of the material surface bounding the plasma, the impact of plasma particles on the surface could cause the emission of secondary electrons. Also, externally heating the surface or surface heating by these impacts could likewise produce thermionic emission of electrons. The effects of such processes on the plasma sheath is another area of prime interest. In 1929, Langmuir[30] investigated

the effects of surface-emitted electrons on probe characteristics. If a wire or probe is attached to a voltage supply and immersed in a plasma, local properties of the plasma can be determined by measuring the current carried by the wire. Langmuir discovered that the space potential could be determined by heating the probe, causing thermionic emission. If the probe could be sufficiently heated while the applied voltage decreased, the point where the cold and hot probe measurements disagreed would yield the space potential.[11] Sizonenko[31] noted that for secondary electron emission coefficients (the ratio of emitted electrons to impacting electrons) exceeding unity, positive or negative charge accumulated, relative to the plasma, near the surface. He showed that such emission coefficients could reduce the amount of sputtering from the divertor plates of a thermonuclear reactor since the loss of electrons to the divertor artificially cooled the plasma periphery. Investigating the influence of secondary electrons on the stability of the plasma sheath, Franklin and Han[32] determined that the wall potential could be decreased by increasing the secondary electron emission coefficient. Electrons emitted from the plasma-facing surface, which is not assumed to be electrically floating, with zero energy was considered by Ordonez.[33] He found that the electron emission decreased the floating potential and the presence of a current directed toward (away from) the surface increased (decreased) the floating potential. The effect of surface-emitted electrons with non-zero temperature was later investigated by Schwager[34] and Ordonez[35] for electrically floating surfaces and demonstrated the same relationship between the electron emission and floating potential. Stephens and Ordonez[36] extended the theory to include warm secondary electrons and non-zero currents. They found that the material surface could become positive with respect to the plasma (as opposed to the familiar negative bias for floating surfaces) but

required either a large secondary electron emission coefficient or large currents for a non-emissive surface. Furthermore, they also demonstrated that the current in such sheaths are nearer the ion current saturation limit as opposed to the electron current saturation limit.

Chapter 4 derives the DF for particles entering various potential energy profiles. Choosing to work with potential energy rather than electric potential profiles permits the same potential energy profile to be used for different electric potential profiles, depending upon the sign of the particle's charge. After deriving the DF and a few moments, these results are applied to particular electric potential profiles. For each potential profile, boundary conditions are applied to the charge density and particle flux to derive a set of nonlinear equations for the potential at the plasma edge, the solid surface and the potential minimum (if appropriate). These equations are then simultaneously solved for a variety of parameter values (ion temperature and charge state, electron temperature, secondary electron emission coefficient and temperature, as well as the ion-to-electron mass ratio). Approximate expressions for the potential at these three locations are then determined to avoid the necessity of solving the nonlinear set of equations. The dependence of the electric potential upon the mentioned parameters are then discussed. Also, profiles of the particle density, normalized temperature and energy flux are given for each species.

REFERENCES

[1]D. Bohm, "Minimum ionic kinetic energy for a stable sheath," in *The Characteristics of Electrical Discharges in Magnetic Fields*, edited by A. Guthry and R. K. Wakerling (McGraw-Hill, New York, 1949), chapter 3.

[2]G. A. Emmert, R. M. Wieland, A. T. Mense, and J. N. Davidson, "Electric Sheath and Presheath in a Collisionless, Finite Ion Temperature Plasma," Phys. Fluids **23**, 803 (1980).

[3]L. Tonks and I. Langmuir, "A General Theory of the Plasma of an Arc," Phys. Rev. **34**, 876 (1929).

[4]P. C. Stangeby, "Plasma Sheath Transmission Factors for Tokomak Edge Plasmas," Phys. Fluids **27**, 682 (1984).

[5]P. C. Stangeby, "Large Probes in Tokomak Scrape-off Plasmas. Analytic Model for the Collisionless Scrape-off Layer," Phys. Fluids **28**, 644 (1985).

[6]G. F. Matthews, G. M. McCracken, P. Sewell, M. Woods, and B. J. Hopkins, "The Determination of Sheath Potential from Retarding Field Analyser Measurements in Tokomak Edge Plasmas," J. Nucl. Mater. **145–147**, 225 (1987).

[7]G. R. Misium, A. J. Lichtenberg, and M. A. Lieberman, "Macroscopic Modeling of Radio-frequency Plasma Discharges," J. Vac. Sci. Technol. A **7**, 1007 (1989).

[8]T. E. Nitschke and D. B. Graves, "Matching an RF Sheath Model to a Bulk Plasma Model," IEEE Trans. Plas. Sci. **23**, 717 (1995).

[9]P. C. Stangeby, "Edge Probes," J. Nucl. Mater. **145–147**, 105 (1987).

[10]O. Biblarz and G. S. Brown, "Plasma-sheath Approximate Solutions for Planar and Cylindrical Anodes and Probes," J. Appl. Phys. **73**, 8111 (1993).

[11]F. Chen, "Electric Probes," in *Plasma Diagnotic Techniques*, edited by R. H. Huddlestone and S. L. Leonard (Academic Press, New York, 1965), chapter 4.

[12]I. H. Hutchinson, *Principles of plasma diagnostics*, Cambridge University Press, Cambridge, 1987.

[13]P. Zhu, J. J. Lowke, and R. Morrow, "A Unified Theory of Free Burning Arcs, Cathode Sheaths and Cathodes," J. Phys. D: Appl. Phys **25**, 1221 (1992).

[14]E. R. Harrison and W. B. Thompson, Proc. Phys. Soc. London **74**, 145 (1959).

[15]A. Caruso and A. Cavaliere, "Velocity Anisotropy of the Sheath Region," Nuovo Cimento **26**, 1389 (1962).

[16]S. A. Self, Phys. Fluids **6**, 1762 (1963).

[17]K.-U. Riemann, "Kinetic Theory of the Plasma Sheath in a Weakly Ionized Plasma," Phys. Fluids **24**, 2163 (1981).

[18]R. C. Bissell and P. C. Johnson, "The Solution of the Plasma Equation in Plane Parallel Geometry with a Maxwellian Source," Phys. Fluids **30**, 779 (1987).

[19]S. Biehler, G. Ecker, and K.-U. Riemann, "Theory of the Presheath in a Weakly Ionized Plasma with Hot Neutrals," Phys. Fluids **31**, 1999 (1988).

[20]J. T. Sheuer and G. A. Emmert, "Sheath and Presheath in a Collisionless Plasma with a Maxwellian Source," Phys. Fluids **31**, 3645 (1988).

[21]R. C. Bissell, "The Application of the Generalized Bohm Criterion to Emmert's Solution of the Warm Ion Collisionless Plasma Equation," Phys. Fluids **30**, 2264 (1987).

[22]P. Auer, J. Appl. Phys. **13**, 2096 (1960).

[23]R. G. McIntyre, "Extended Space-Charge Theory in Low-Pressure Thermionic Converters," J. Appl. Phys **33**, 2485 (1962).

[24]R. G. McIntyre, Proc. IEEE **51**, 760 (1963).

[25]N. Rynn, "Plasma Column End Effects," Phys. Fluids **9**, 165 (1966).

[26]S. Kuhn, "Axial Equilibria, Disruptive Effects, and Buneman Instability in Collisionless Single-Ended Q-machine," Plas. Phys. **23**, 881 (1981).

[27]W. Ott, "Investigation of a Cesium Plasma Diode Using an Electron Beam Probing Technique," Z. Naturforsch. **22**, 1057 (1967).

[28]T. L. Crystal, P. C. Gray, W. S. Lawson, C. K. Birdsall, and S. Kuhn, "Trapped-electron Effects on Time-independent Negative-bias States of a Collisionless Single-emitter Plasma Device: Theory and Simulation," Phys. Fluids B **3**, 244 (1991).

[29]L. A. Schwager and C. K. Birdsall, "Collector and Source Sheaths of a Finite Ion Temperature Plamsa," Phys. Fluids B **2**, 1057 (1990).

[30]I. Langmuir, "The Interaction of Electron and Positive Ion Space Charges in Cathode Sheaths," Phys. Rev. **33**, 964 (1929).

[31]V. L. Sizonenko, "Effects of Strong Secondary Electron Emission of a Plasma Layer," Sov. Phys. Tech. Phys. **26**, 1345 (1981).

[32]R. N. Franklin and W. E. Han, "The Stability of the Plasma-Sheath with Secondary Emission," Plasma Phys. Controlled Fusion **30**, 771 (1988).

[33]C. A. Ordonez, "Fully Kinetic Plasma-sheath Theory for a Cold-electron Emitting Surface," Phys. Fluids B **4**, 778 (1992).

[34]L. A. Schwager, "Effects of Secondary and Thermionic Electron Emission on the Collector and Source Sheaths of a Finite Ion Temperature Plasma using Kinetic Theory and Numerical Simulation," Phys. Fluids B **5**, 631 (1993).

[35]C. A. Ordonez, "Boundary Conditions Including Sheath Effects at a Plasma-Facing Surface," Phys. Rev. E **55**, 1858 (1997).

[36]K. F. Stephens, II and C. A. Ordonez, "Sheath and Presheath Potentials for Anode, Cathode and Floating Plasma-Facing Surface," J. Appl. Phys. **85**, 2522 (1999).

CHAPTER 4

THEORETICAL INVESTIGATION OF PLANAR SHEATHS

To obtain the most information about a planar sheath, fully kinetic sheath theory is the natural choice since the distribution function provides a maximum amount of information on the system. From a practical point of view, the most relevant features of the sheath are the value of the electric potential at the surface as well as the transition from the edge plasma to the presheath. Using the planar-source model along with truncated Maxwellians, three profiles of the electric potential within the sheath are studied. These three profiles exhaust the possible non-oscillatory profiles for a sheath with a single minimum. To facilitate the distribution function construction for the three particle species considered (plasma ions, plasma electrons and secondary electrons), potential energy profiles are first considered. These results are then applied to the three electric potential profiles in question, yielding the necessary quantities that define the value of the potential at the edge-plasma/presheath and sheath/surface interfaces, along with the electric potential minimum for cases where space-charge saturation are present. Since these values must be determined from a system of nonlinear equations, approximate expressions for these quantities are also provided. The effect of varying the plasma and surface parameters on the value of the electric potential at the edge-plasma, surface and minimum are described. Profiles for the particle density, normalized temperature and energy flux through the sheath are then presented.

Distribution Function and Moments for Three Potential Energy Profiles

This section uses the planar-source model to determine the distribution function for particles in various potential energy profiles. Once the distribution functions are found, the first two moments along with the normalized temperature and energy flux are calculated for each case. Using a potential energy profile rather than specific electric potential profiles avoids consideration of the particle's charge. For example, a plasma electron entering a monotonically decreasing electric potential exhibits similar phase space properties to a positive ion entering a monotonically increasing potential. Rather than computing each of these cases, using the potential energy profile allows the distribution function to be found once and used for those combinations of electric potential and particle charge that yield the same potential energy profile. Specifically, three potential energy profiles will be considered: 1) an accelerating, non-reflecting profile; 2) an initially retarding profile; and 3) an initially accelerating profile with reflection. These three profiles were found to comprise all non-oscillatory electric potential profiles that correspond to single minimum sheaths.

Consider a potential energy, $U(x)$, defined between the points x_0 and x_n such that $x_0 < x_n$. Let particles be injected at x_0 with only positive velocities. The distribution function at x_0 for particles of mass m has the form $f_0(\mathbf{v})\Theta(v_x)$ where Θ is the Heaviside step function and

$$f_0(\mathbf{v}) = n_0 \left(\frac{\beta}{\pi}\right)^{3/2} e^{-\beta v^2}. \tag{4.1}$$

Here, $\beta = m/2T_0$ and n_0 (T_0) is the density (temperature) associated with the full Maxwellian $f_0(\mathbf{v})$. By conservation of energy and momentum, the velocity of a particle at x_0 can be written in terms of the particle's velocity, v_x, while located at x according

to

$$v_{0,x} = \sqrt{{v_x}^2 + 2\frac{U(x) - U(x_0)}{m}}. \tag{4.2}$$

Considering only steady state configurations, the distribution function must first satisfy the Vlasov equation,

$$mv_x \frac{\partial f(x, \mathbf{v})}{\partial x} = \frac{\partial U(x)}{\partial x} \frac{\partial f(x, \mathbf{v})}{\partial v_x}.$$

The distribution function $f(x, \mathbf{v}) = f(v_{0,x}, v_y, v_z)$ satisifies this condition, where $v_{0,x}$ is replaced by the right-hand side of Eq. (4.2). The distribution function must also take into account inaccessible regions of phase space. To accomplish this, the explicit form of the potential energy must be known. The remainder of this section considers specific potential energy profiles in order to describe these inaccessible regions.

As mentioned, four different moments of the distribution function are computed for each potential energy profile. In terms of the distribution function $f(\mathbf{x}, \mathbf{v})$ for a particle of mass m, the definitions of these moments are:

Particle Density:

$$n(\mathbf{x}) = \int f(\mathbf{x}, \mathbf{v}) \; d^3\mathbf{v}. \tag{4.3}$$

Particle Flux:

$$\mathbf{F}(\mathbf{x}) = \int \mathbf{v} f(\mathbf{x}, \mathbf{v}) \; d^3\mathbf{v}. \tag{4.4}$$

Normalized Temperature:

$$T = \frac{m}{3} \left[\frac{\int v^2 f(\mathbf{x}, \mathbf{v}) \, d^3\mathbf{v}}{\int f(\mathbf{x}, \mathbf{v}) \, d^3\mathbf{v}} - \left(\frac{\int \mathbf{v} f(\mathbf{x}, \mathbf{v}) \, d^3\mathbf{v}}{\int f(\mathbf{x}, \mathbf{v}) \, d^3\mathbf{v}} \right)^2 \right]. \tag{4.5}$$

Energy Flux:

$$\mathbf{Q} = \frac{m}{2} \int v^2 \mathbf{v} f(\mathbf{x}, \mathbf{v}) \, d^3\mathbf{v}. \tag{4.6}$$

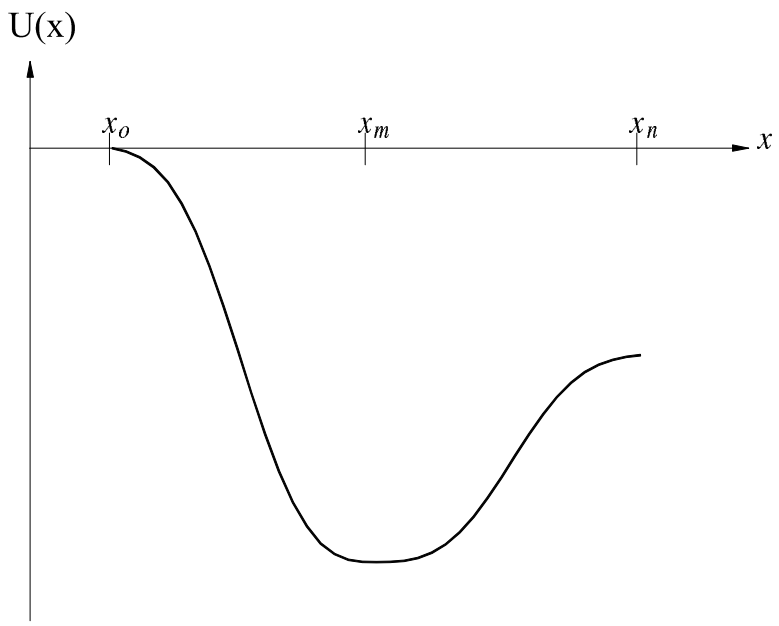

FIG. 4.1. Potential energy profile considered in this section. A planar source of particles is located at x_o and injects particles toward x_n. All particles injected at x_o pass through to x_n.

Potential Energy Profile 1

Figure 4.1 shows the first potential energy profile. Particles injected at x_0 will pass through to x_n and will only have positive velocities. However, the particles must have a velocity $v_x > \sqrt{2[U(x_0) - U(x)]/m}$ in order to enter the region between x_0 and x_n. Therefore, the distribution function is

$$f\left(x, \mathbf{v}\right) = f_0\left(v_{0,x}, v_y, v_z\right) \Theta\left(v_x - \sqrt{2\frac{U\left(x_0\right) - U\left(x\right)}{m}}\right).$$

Using the substitution $\psi_{0x} = [U(x_0) - U(x)]/T_0$, the distribution function can be re-written as

$$f\left(x, \mathbf{v}\right) = n_0 \left(\frac{\beta}{\pi}\right)^{3/2} e^{-\beta v^2 + \psi_{0x}} \Theta\left(v_x - \sqrt{\frac{\psi_{0x}}{\beta}}\right). \tag{4.7}$$

The moments defined in Eqs. (4.3)–(4.6) can now be calculated using Eq. (4.7). Dropping the explicit position dependence, these moments are:

Particle Density:

$$n = \frac{1}{2} n_0 G_1 \left(\psi_{0x}\right). \tag{4.8}$$

Particle Flux:

$$F = \frac{n_0}{2\sqrt{\pi\beta}}. \tag{4.9}$$

Normalized Temperature:

$$\frac{T}{T_0} = 1 + \frac{2}{3G_1\left(\psi_{0x}\right)}\sqrt{\frac{\psi_{0x}}{\pi}} - \frac{2}{3\pi\left[G_1\left(\psi_{0x}\right)\right]^2}. \tag{4.10}$$

Energy Flux:

$$Q = n_0 T_0 \frac{2 + \psi_{0x}}{2\sqrt{\pi\beta}}. \tag{4.11}$$

Here, $G_1(z) = e^z \operatorname{erfc}(\sqrt{z})$ where $\operatorname{erfc}(z) = \frac{2}{\sqrt{\pi}} \int_z^\infty e^{-t^2}\, dt$ is the complementary error function.

Potential Energy Profile 2

Figure 4.2 shows the second potential energy profile considered. First, examine the region $x_m < x < x_n$. It is clear that this is identical to the profile considered in the previous section with $U(x_0)$ replaced by $U(x_m)$. Thus, for this region, the distribution function is

$$f\left(x, \mathbf{v}\right) = f_0\left(v_{0,x}, v_y, v_z\right) \Theta\left(v_x - \sqrt{\frac{\psi_{mx}}{\beta}}\right),$$

where $\psi_{mx} = [U(x_m) - U(x)]/T_0$.

For the region $x_0 < x < x_m$, particles with energy less than $U(x_m) - U(x_0)$ are reflected; particles with energy greater than this continue toward x_n. The fastest reflected particle has energy exactly equal to this. Thus, this value represents the

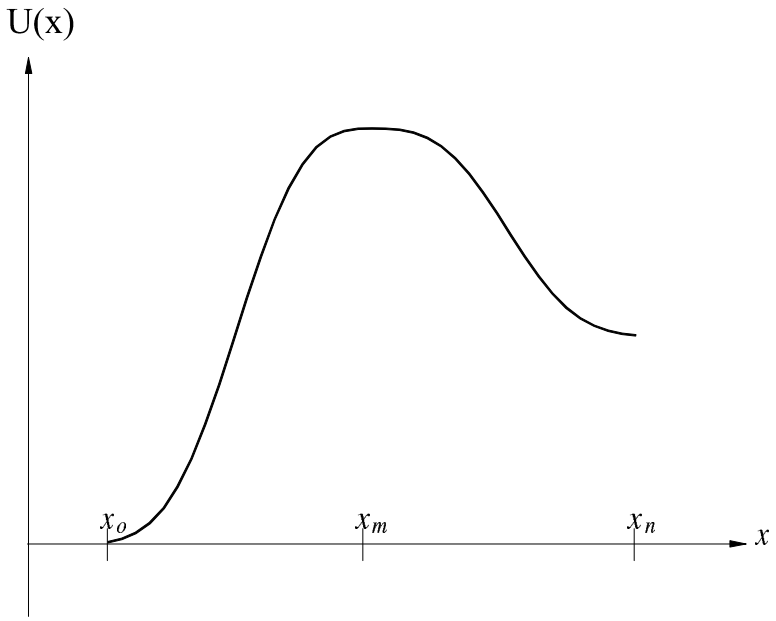

FIG. 4.2. Potential energy profile considered in this section. A planar source of particles is located at x_o and injects particles toward x_n. Particles injected at x_o with kinetic energy less than $U(x_m)$ are reflected back towards x_n. The remaining particles reach x_n.

maximum negative velocity. Hence, the distribution function for this region is

$$f\left(x,\mathbf{v}\right)=f_0\left(v_{0,x},v_y,v_z\right)\Theta\left(v_x+\sqrt{\frac{\psi_{mx}}{\beta}}\right).$$

Therefore, the distribution function for particles in the potential energy profile shown in Fig. 4.2 is

$$f\left(x,\mathbf{v}\right)=n_0\left(\frac{\beta}{\pi}\right)^{3/2}e^{-\beta v^2+\psi_{0x}}\begin{cases}\Theta\left(v_x+\sqrt{\frac{\psi_{mx}}{\beta}}\right), & x_0<x<x_m,\\ \Theta\left(v_x-\sqrt{\frac{\psi_{mx}}{\beta}}\right), & x_m<x<x_s.\end{cases}\tag{4.12}$$

The desired moments are now found to be:

Particle Density:

$$n=\frac{1}{2}n_0\,e^{-\psi_{m0}}\begin{cases}G_2\left(\psi_{mx}\right), & x_0<x<x_m,\\ G_1\left(\psi_{mx}\right), & x_m<x<x_n.\end{cases}\tag{4.13}$$

Particle Flux:

$$F = \frac{n_0}{2\sqrt{\pi\beta}} e^{-\psi_{m0}}. \tag{4.14}$$

Normalized Temperature:

$$\frac{T}{T_0} = \begin{cases} 1 - \dfrac{2}{3G_2\left(\psi_{mx}\right)}\sqrt{\dfrac{\psi_{mx}}{\pi}} - \dfrac{2}{3\pi\left[G_2\left(\psi_{mx}\right)\right]^2}, & x_0 < x < x_m, \\ 1 + \dfrac{2}{3G_1\left(\psi_{mx}\right)}\sqrt{\dfrac{\psi_{mx}}{\pi}} - \dfrac{2}{3\pi\left[G_1\left(\psi_{mx}\right)\right]^2}, & x_m < x < x_n. \end{cases} \tag{4.15}$$

Energy Flux:

$$Q = n_0 T_0 \frac{2 + \psi_{mx}}{2\sqrt{\pi\beta}} e^{-\psi_{m0}}. \tag{4.16}$$

The definitions $\psi_{m0} = [U(x_m) - U(x_0)]/T_0$ and $G_2(z) = e^z \operatorname{erfc}(-\sqrt{z})$ were used.

Potential Energy Profile 3

The final potential energy profile to be considered is shown in Fig. 4.3. Because there is a barrier proceeding the potential well, this profile has more complicated forbidden regions in phase space. First consider the region $x_r < x < x_n$. The potential in this range is similar to the range $x_0 < x < x_m$ of the profile considered in the previous section. Thus the distribution function for $x_r < x < x_n$ is given by

$$f\left(x, \mathbf{v}\right) = f_0\left(v_{0,x}, v_y, v_z\right) \Theta\left(v_x + \sqrt{\frac{\psi_{nx}}{\beta}}\right), \tag{4.17}$$

where $\psi_{nx} = [U(x_n) - U(x)]/T_0$.

The region $x_0 < x < x_r$ introduces two disjoint allowed regions of phase space. The first allowed region corresponds to particles with positive velocities. In order for injected particles to pass x_0, there velocities must satisfy $v_x > \sqrt{\psi_{0x}/T_0}$. The second allowed region pertains to negative velocity particles. The particles with the

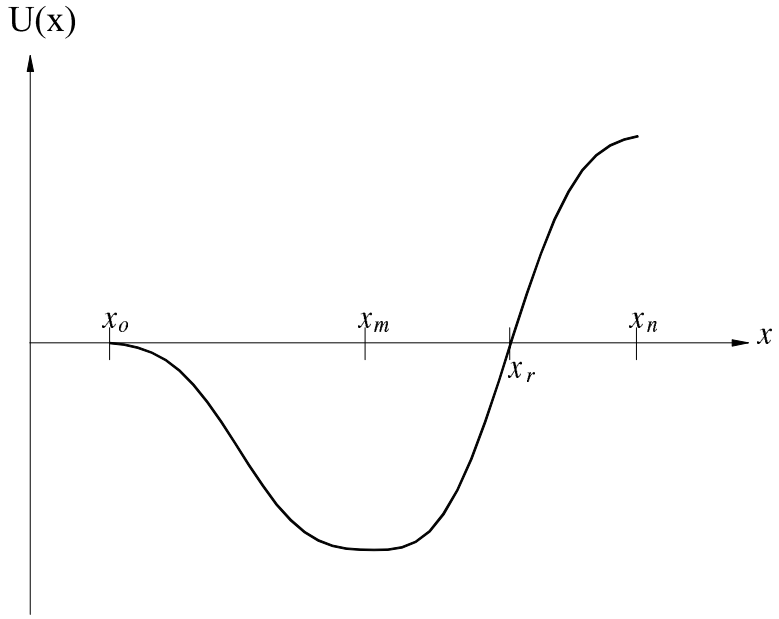

FIG. 4.3. Potential energy profile considered in this section. A planar source of particles is located at x_o and injects particles toward x_n. Particles injected at x_o with kinetic energy less than $U(x_n)$ are reflected back towards x_n. The remaining particles reach x_n.

largest negative velocity are those that have kinetic energy equal to $U(x_n) - U(x_0)$. The particles with the smallest negative velocity have kinetic energy equal to $U(x_0)$. Thus, the distribution function for particles between x_0 and x_r can be written as

$$f\left(x, \mathbf{v}\right) = f_0\left(v_{0,x}, v_y, v_z\right) \Theta\left(v_x + \sqrt{\frac{\psi_{nx}}{\beta}}\right) \Theta\left(|v_x| + \sqrt{\frac{\psi_{0x}}{\beta}}\right).$$

Collecting the results of this section, the distribution functions for particles injected into the potential energy profile shown in Fig. 4.3 is

$$\begin{aligned} f\left(x, \mathbf{v}\right) &= n_0 \left(\frac{\beta}{\pi}\right)^{3/2} e^{-\beta v^2 + \psi_{0x}} \\ &\times \begin{cases} \Theta\left(v_x + \sqrt{\frac{\psi_{nx}}{\beta}}\right) \Theta\left(|v_x| - \sqrt{\frac{\psi_{0x}}{\beta}}\right), & x_0 < x < x_r, \\ \Theta\left(v_x + \sqrt{\frac{\psi_{nx}}{\beta}}\right), & x_r < x < x_s. \end{cases} \end{aligned} \tag{4.18}$$

Using this distribution function, the moments defined in Eqs. (4.3)–(4.6) are found to be:

Particle Density:

$$n = \frac{1}{2} n_0 \, e^{-\psi_{n0}} \begin{cases} 2e^{\psi_{n0}} G_1 \left(\psi_{0x}\right) - G_1 \left(\psi_{nx}\right), & x_0 < x < x_r, \\ G_2 \left(\psi_{nx}\right), & x_r < x < x_n. \end{cases} \tag{4.19}$$

Particle Flux:

$$F = \frac{n_0}{2\sqrt{\pi\beta}} e^{-\psi_{n0}}. \tag{4.20}$$

Normalized Temperature:

$$\frac{T}{T_0} = \begin{cases} 1 + \dfrac{2}{3G_1 \left(\psi_{0x}\right)} \sqrt{\dfrac{\psi_{0x}}{\pi}} - \dfrac{2}{3\pi \left[G_1 \left(\psi_{0x}\right)\right]^2}, & x_0 < x < x_r, \\ & v_x > 0, \\ 1 - \dfrac{2}{3G_2 \left(\psi_{nx}\right)} \sqrt{\dfrac{\psi_{nx}}{\pi}} - \dfrac{2}{3\pi \left[G_2 \left(\psi_{nx}\right)\right]^2}, & x_r < x < x_n. \end{cases} \tag{4.21}$$

Energy Flux:

$$Q = n_0 T_0 \frac{2 + \psi_{nx}}{2\sqrt{\pi\beta}} e^{-\psi_{n0}}. \tag{4.22}$$

Distribution Function and Moments for Three Electric Potential Profiles

For a particle of charge q in a static electric potential ϕ, with no other forces acting on the particle, the particle's potential energy is simply $q\phi$. Thus, given an electric potential profile the distribution function is easily determined by comparing the potential energy profile, resulting from the specified electric potential profile, with those discussed in the previous section. For example, a negatively charged particle, $q < 0$, in an electric potential that monotonically decreases from x_o to x_n corresponds to the first potential energy profile with $x_n = x_m$. Knowing this, the distribution function and first few moments can be written down by inspection of

the formulas from the previos section. This section applies this procedure to the three electric potential profiles illustrated in Fig. 4.4. These particular profiles are chosen because they represent the complete set of non-oscillatory solutions for a single minimum sheath. Also, these three cases correspond to different levels of electron space-charge saturation. The profile shown in Fig. 4.4(a) can only occur when the emission coefficient of secondary electrons from the surface is less than a critical value. If the emission coefficient exceeds this value, the increase in negative space-charge near the surface produces an electric potential minimum near, but not coincident with, the surface. The potential profile then resembles that shown in Fig. 4.4(b). The characteristic minimum in the potential is present whenever the emission coefficient exceeds this critical value, and the sheath is called "space-charge saturated." If the emission coefficient is increased further yet, the surface will eventually become positive compared to the plasma edge and the electric potential profile is similar to that shown in Fig. 4.4(c). Increasing the secondary electron emission coefficient further still, the qualitative shape of the potential profile does not change: there is still a potential minimum near the surface and the surface is positive with respect to the edge plasma.

To simplify the expressions derived in this chapter, some new notation is now introduced. The symbol ψ continues to represent the normalized electric potential for each species, as determined by the subscripts: i—plasma ions; e—plasma electrons; and δ—secondary electrons. For example, the normalized potential for plasma electrons is given by $\psi_e = -e\phi/T_{pe}$, for the plasma ions by $\psi_i = Ze\phi/T_{pi}$ for charge state Z and for the secondary electrons by $\psi_\delta = -e\psi/T_{s\delta}$. Several new subscripts are used to represent the position at which the potential is evaluated. These are defined as:

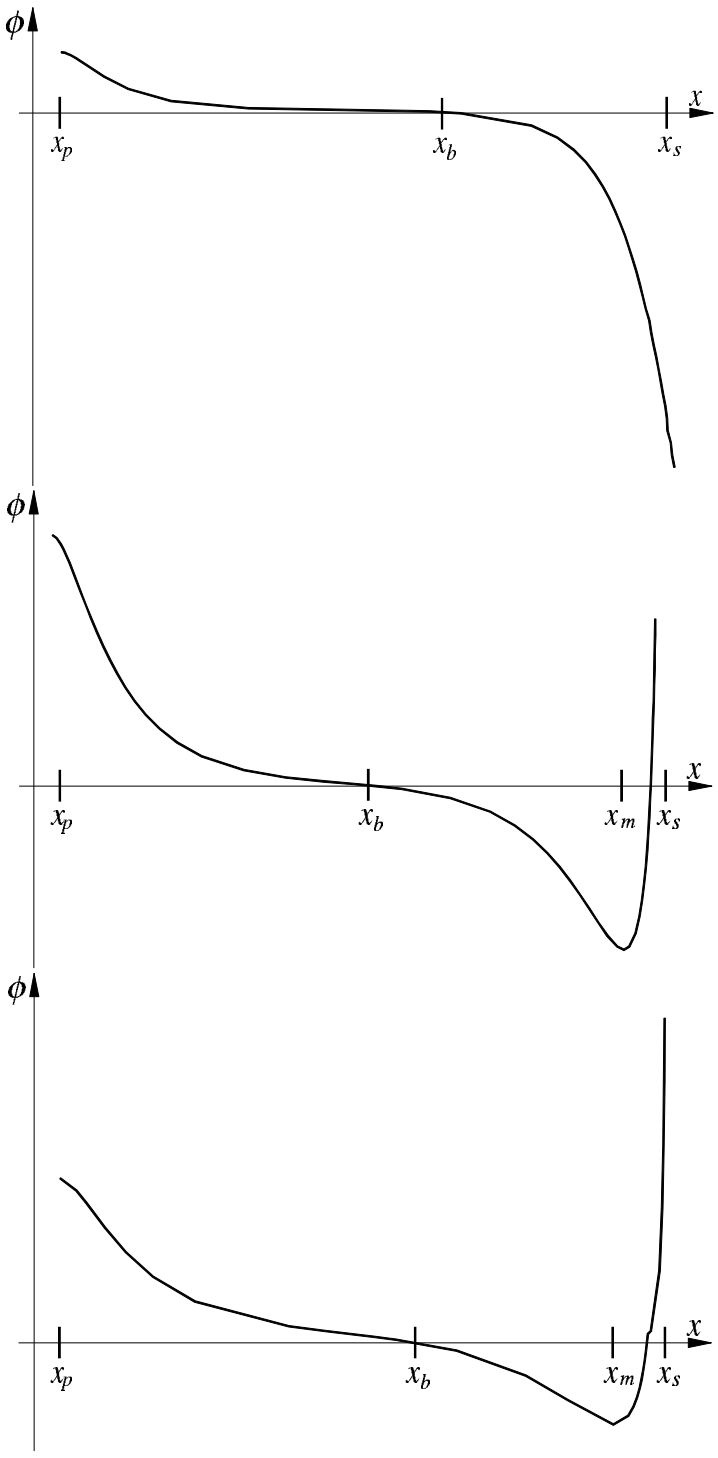

FIG. 4.4. The electric potential profiles considered in this section. These correspond to (a) no space-charge saturation, (b) space-charge saturation with a surface negatively biased with respect to the plasma, and (c) space-charge saturation with the surface positively biased with respect to the plasma.

p — edge-plasma/presheath interface, x_p,

b — presheath/sheath interface, x_b,

m — electric potential minimum, x_m,

r — position in the sheath where the potential equals $\phi(x_p,\, x_r)$,

s — sheath/surface interface, x_s, and

x — arbitrary location within the sheath, x.

Two adjacent position subscripts represents a difference. For example, the sheath potential, defined as the difference between the potential at the edge-plasma and the surface is denoted as $\phi_{ps} = \phi_p - \phi_s$. The inverse-square of the thermal velocities are given by $\beta_e = m_e/2T_{pe}$ for plasma electrons, $\beta_i = m_i/2T_{pi}$ for plasma ions and $\beta_\delta = m_e/2T_{s\delta}$ for secondary electrons. The charge state of the ions is Z. To illustrate this notation, the difference in normalized potential energy for secondary electrons between the surface and the edge-plasma is $\psi_{sp\delta} = -e\phi_{sp}/T_{s\delta} = -e[\phi(x_s) - \phi(x_p)]/T_{s\delta}$.

Monotonically Decreasing Profile

The first electric potential profile considered is shown in Fig. 4.4(a). The positive plasma ions entering at x_p experience a monotonically descreasing potential profile. Using the expressions appropriate for this profile, the plasma ions are described by

Plasma Ions

Distribution function:

$$f_i\left(x, \mathbf{v}\right) = n_{pi}\left(\frac{\beta_i}{\pi}\right)^{3/2} e^{-\beta_i v^2 + \psi_{pxi}} \Theta\left(v_x - \sqrt{\frac{\psi_{pxi}}{\beta_i}}\right), \tag{4.23}$$

Particle Density:

$$n_i = \frac{1}{2} n_{pi} G_1 \left(\psi_{pxi} \right), \tag{4.24}$$

Particle Flux:

$$F_i = \frac{n_{pi}}{2\sqrt{\pi \beta_i}}, \tag{4.25}$$

Normalized Temperature:

$$\frac{T_i}{T_{pi}} = 1 + \frac{2}{3G_1 \left(\psi_{pxi} \right)} \sqrt{\frac{\psi_{pxi}}{\pi}} - \frac{2}{3\pi \left[G_1 \left(\psi_{pxi} \right) \right]^2}, \tag{4.26}$$

Energy Flux:

$$Q_i = n_{pi} T_{pi} \frac{2 + \psi_{pxi}}{2\sqrt{\pi \beta_i}}. \tag{4.27}$$

For the negative plasma electrons, the profile appears as a monotonically increasing barrier. This corresponds to the potential energy profile shown in Fig. 4.2 where the maximum occurs at the surface, $x_m = x_n$. Using the appropriate expressions given above, the description of the plasma electrons is given by

Plasma Electrons

Distribution function:

$$f_e \left(x, \mathbf{v} \right) = n_{pe} \left(\frac{\beta_e}{\pi} \right)^{3/2} e^{-\beta_e v^2 - \psi_{xpe}} \Theta \left(v_x + \sqrt{\frac{\psi_{sxe}}{\beta_e}} \right), \tag{4.28}$$

Particle Density:

$$n_e = \frac{1}{2} n_{pe} \, e^{-\psi_{spe}} G_2 \left(\psi_{sxe} \right), \tag{4.29}$$

Particle Flux:

$$F_e = \frac{n_{pe}}{2\sqrt{\pi \beta_e}} e^{-\psi_{spe}}. \tag{4.30}$$

Normalized Temperature:

$$\frac{T_e}{T_{pe}} = 1 - \frac{2}{3G_2\left(\psi_{sxe}\right)}\sqrt{\frac{\psi_{sxe}}{\pi}} - \frac{2}{3\pi\left[G_2\left(\psi_{sxe}\right)\right]^2}, \tag{4.31}$$

Energy Flux:

$$Q_e = n_{pe}T_{pe}\frac{2+\psi_{sxe}}{2\sqrt{\pi\beta_e}}e^{-\psi_{spe}}. \tag{4.32}$$

The secondary electrons enter at x_s so that an electric potential that monotonically increases from x_p appears to the secondary electrons as a potential energy profile that monotonically decreases from x_s to x_p. Using the expressions determined above for this profile yields the following description of the secondary electrons

Secondary Electrons

Distribution function:

$$f_\delta\left(x,\mathbf{v}\right) = n_{s\delta}\left(\frac{\beta_\delta}{\pi}\right)^{3/2} e^{-\beta_\delta v^2+\psi_{sx\delta}}\Theta\left(v_x - \sqrt{\frac{\psi_{sx\delta}}{\beta_\delta}}\right), \tag{4.33}$$

Particle Density:

$$n_\delta = \frac{1}{2}n_{s\delta}G_1\left(\psi_{sx\delta}\right), \tag{4.34}$$

Particle Flux:

$$F_\delta = \frac{n_{s\delta}}{2\sqrt{\pi\beta_\delta}}, \tag{4.35}$$

Normalized Temperature:

$$\frac{T_\delta}{T_{s\delta}} = 1 + \frac{2}{3G_1\left(\psi_{sx\delta}\right)}\sqrt{\frac{\psi_{sx\delta}}{\pi}} - \frac{2}{3\pi\left[G_1\left(\psi_{sx\delta}\right)\right]^2}, \tag{4.36}$$

Energy Flux:

$$Q_\delta = n_{s\delta}T_{s\delta}\frac{2+\psi_{sx\delta}}{2\sqrt{\pi\beta_\delta}}. \tag{4.37}$$

Single Minimum, Negative-Wall Profile

The next electric potential profile to be considered is shown in Fig. 4.4(b). As the plasma ions enter the region at x_p, they again encounter an accelerating force. No ions are reflected after passing x_m and the appropriate potential energy profile is still that shown in Fig. 4.1. Thus, the plasma ions obey the same system of equations as for a monotonically decreasing potential. For completeness, these equations are repeated here:

Plasma Ions

Distribution function:

$$f_i\left(x,\mathbf{v}\right)=n_{pi}\left(\frac{\beta_i}{\pi}\right)^{3/2}e^{-\beta_i v^2+\psi_{pxi}}\Theta\left(v_x-\sqrt{\frac{\psi_{pxi}}{\beta_i}}\right), \tag{4.38}$$

Particle Density:

$$n_i=\frac{1}{2}n_{pi}G_1\left(\psi_{pxi}\right), \tag{4.39}$$

Particle Flux:

$$F_i=\frac{n_{pi}}{2\sqrt{\pi\beta_i}}, \tag{4.40}$$

Normalized Temperature:

$$\frac{T_i}{T_{pi}}=1+\frac{2}{3G_1\left(\psi_{pxi}\right)}\sqrt{\frac{\psi_{pxi}}{\pi}}-\frac{2}{3\pi\left[G_1\left(\psi_{pxi}\right)\right]^2}, \tag{4.41}$$

Energy Flux:

$$Q_i=n_{pi}T_{pi}\frac{2+\psi_{pxi}}{2\sqrt{\pi\beta_i}}. \tag{4.42}$$

Inverting the potential profile shows that it most closely resembles the potential energy profile of Fig. 4.2. Unlike the previous electric potential profile, the potential

minimum is located away from the surface. Thus, the plasma electrons are described by

Plasma Electrons

Distribution function:

$$f_e(x,\mathbf{v}) = n_{pe}\left(\frac{\beta_e}{\pi}\right)^{3/2} e^{-\beta_e v^2-\psi_{xpe}} \times \begin{cases} \Theta\left(v_x+\sqrt{\dfrac{\psi_{mxe}}{\beta_e}}\right), & x_p<x<x_m, \\ \Theta\left(v_x-\sqrt{\dfrac{\psi_{mxe}}{\beta_e}}\right), & x_m<x<x_s. \end{cases} \tag{4.43}$$

Particle Density:

$$n_e = \frac{1}{2} n_{pe}\, e^{-\psi_{mpe}} \begin{cases} G_2(\psi_{mxe}), & x_p<x<x_m, \\ G_1(\psi_{mxe}), & x_m<x<x_s. \end{cases} \tag{4.44}$$

Particle Flux:

$$F_e = \frac{n_{pe}}{2\sqrt{\pi\beta_e}} e^{-\psi_{mpe}}. \tag{4.45}$$

Normalized Temperature:

$$\frac{T_e}{T_{pe}} = \begin{cases} 1-\dfrac{2}{3G_2(\psi_{mxe})}\sqrt{\dfrac{\psi_{mxe}}{\pi}}-\dfrac{2}{3\pi\left[G_2(\psi_{mxe})\right]^2}, & x_p<x<x_m, \\ 1+\dfrac{2}{3G_1(\psi_{mxe})}\sqrt{\dfrac{\psi_{mxe}}{\pi}}-\dfrac{2}{3\pi\left[G_1(\psi_{mxe})\right]^2}, & x_m<x<x_s. \end{cases} \tag{4.46}$$

Energy Flux:

$$Q_e = n_{pe}T_{pe}\frac{2+\psi_{mxe}}{2\sqrt{\pi\beta_e}} e^{-\psi_{mpe}}. \tag{4.47}$$

Since the value of the electric potential at the wall is less than at the edge-plasma, the secondary electrons entering the profile shown in Fig. 4.4(b) at x_s encounter a potential energy profile similar to the one shown in Fig. 4.3. Using the expressions given above, the secondary electrons are described according to

Secondary Electrons

Distribution function:

$$f_\delta(x,\mathbf{v}) = n_{s\delta}\left(\frac{\beta_\delta}{\pi}\right)^{3/2} e^{-\beta_\delta v^2+\psi_{sx\delta}} \times \begin{cases} \Theta\left(v_x-\sqrt{\dfrac{\psi_{mx\delta}}{\beta_\delta}}\right), & x_p<x<x_m, \\ \Theta\left(v_x+\sqrt{\dfrac{\psi_{mx\delta}}{\beta_\delta}}\right), & x_m<x<x_s. \end{cases} \tag{4.48}$$

Particle Density:

$$n_\delta = \frac{1}{2}n_{s\delta}e^{-\psi_{ms\delta}} \begin{cases} G_1(\psi_{mx\delta}), & x_p<x<x_m, \\ G_2(\psi_{mx\delta}), & x_m<x<x_s. \end{cases} \tag{4.49}$$

Particle Flux:

$$F_\delta = \frac{n_{s\delta}}{2\sqrt{\pi\beta_\delta}}e^{-\psi_{ms\delta}}, \tag{4.50}$$

Normalized Temperature:

$$\frac{T_\delta}{T_{s\delta}} = \begin{cases} 1+\dfrac{2}{3G_1(\psi_{mx\delta})}\sqrt{\dfrac{\psi_{mx\delta}}{\pi}}-\dfrac{2}{3\pi\left[G_1(\psi_{mx\delta})\right]^2}, & x_p<x<x_m, \\ 1-\dfrac{2}{3G_2(\psi_{mx\delta})}\sqrt{\dfrac{\psi_{mx\delta}}{\pi}}-\dfrac{2}{3\pi\left[G_2(\psi_{mx\delta})\right]^2}, & x_m<x<x_s. \end{cases} \tag{4.51}$$

Energy Flux:

$$Q_\delta = n_{s\delta}T_{s\delta}\frac{2+\psi_{mx\delta}}{2\sqrt{\pi\beta_\delta}}e^{-\psi_{ms\delta}}. \tag{4.52}$$

Single Minimum, Positive-Wall Profile

For the final electric potential profile, Fig. 4.4(c), the plasma ions experience a potential profile similar to that shown in Fig. 4.3. Thus, using the expressions from that section, the ions are described by

Plasma Ions

Distribution function:

$$f_i(x,\mathbf{v}) = n_{pi}\left(\frac{\beta_i}{\pi}\right)^{3/2} e^{-\beta_i v^2+\psi_{pxi}} \times \begin{cases} \Theta\left(v_x+\sqrt{\frac{\psi_{sxi}}{\beta_i}}\right)\Theta\left(|v_x-\sqrt{\frac{\psi_{pxi}}{\beta_i}}\right), & x_p<x<x_r, \\ \Theta\left(v_x+\sqrt{\frac{\psi_{sxi}}{\beta_i}}\right), & x_r<x<x_s. \end{cases} \tag{4.53}$$

Particle Density:

$$n_i = \frac{1}{2}n_{pi}e^{\psi_{psi}} \begin{cases} 2e^{-\psi_{psi}}G_1(\psi_{pxi})-G_1(\psi_{sxi}), & x_p<x<x_r, \\ G_2(\psi_{sxi}), & x_r<x<x_s. \end{cases} \tag{4.54}$$

Particle Flux:

$$F_i = \frac{n_{pi}}{2\sqrt{\pi\beta_i}}e^{\psi_{psi}}, \tag{4.55}$$

Normalized Temperature:

$$\frac{T_i}{T_{pi}} = \begin{cases} 1+\frac{2}{3G_1(\psi_{pxi})}\sqrt{\frac{\psi_{pxi}}{\pi}}-\frac{2}{3\pi\left[G_1(\psi_{pxi})\right]^2}, & x_p<x<x_r, \\ & v_x>0, \\ 1-\frac{2}{3G_2(\psi_{sxi})}\sqrt{\frac{\psi_{sxi}}{\pi}}-\frac{2}{3\pi\left[G_2(\psi_{sxi})\right]^2}, & x_p<x<x_r. \end{cases} \tag{4.56}$$

Energy Flux:

$$Q_i = n_{pi}T_{pi}\frac{2+\psi_{sxi}}{2\sqrt{\pi\beta_i}}e^{\psi_{psi}}. \tag{4.57}$$

For this profile, the plasma and secondary electron distribution functions and moments are the same as those presented in the section that discussed the second potential profile and are repeated here for completeness.

Plasma Electrons

Distribution function:

$$\begin{aligned} f_e(x,\mathbf{v}) &= n_{pe}\left(\frac{\beta_e}{\pi}\right)^{3/2} e^{-\beta_e v^2-\psi_{xpe}} \\ &\times \begin{cases} \Theta\left(v_x+\sqrt{\dfrac{\psi_{mxe}}{\beta_e}}\right), & x_p<x<x_m, \\ \Theta\left(v_x-\sqrt{\dfrac{\psi_{mxe}}{\beta_e}}\right), & x_m<x<x_s. \end{cases} \end{aligned} \tag{4.58}$$

Particle Density:

$$n_e=\frac{1}{2}n_{pe}\,e^{-\psi_{mpe}}\begin{cases} G_2(\psi_{mxe}), & x_p<x<x_m, \\ G_1(\psi_{mxe}), & x_m<x<x_s. \end{cases} \tag{4.59}$$

Particle Flux:

$$F_e=\frac{n_{pe}}{2\sqrt{\pi\beta_e}}e^{-\psi_{mpe}}. \tag{4.60}$$

Normalized Temperature:

$$\frac{T_e}{T_{pe}}=\begin{cases} 1-\dfrac{2}{3G_2(\psi_{mxe})}\sqrt{\dfrac{\psi_{mxe}}{\pi}}-\dfrac{2}{3\pi\left[G_2(\psi_{mxe})\right]^2}, & x_p<x<x_m, \\ 1+\dfrac{2}{3G_1(\psi_{mxe})}\sqrt{\dfrac{\psi_{mxe}}{\pi}}-\dfrac{2}{3\pi\left[G_1(\psi_{mxe})\right]^2}, & x_m<x<x_s. \end{cases} \tag{4.61}$$

Energy Flux:

$$Q_e=n_{pe}T_{pe}\frac{2+\psi_{mxe}}{2\sqrt{\pi\beta_e}}e^{-\psi_{mpe}}. \tag{4.62}$$

Secondary Electrons

Distribution function:

$$\begin{aligned} f_\delta(x,\mathbf{v}) &= n_{s\delta}\left(\frac{\beta_\delta}{\pi}\right)^{3/2} e^{-\beta_\delta v^2+\psi_{sx\delta}} \\ &\times \begin{cases} \Theta\left(v_x-\sqrt{\dfrac{\psi_{mx\delta}}{\beta_\delta}}\right), & x_p<x<x_m, \\ \Theta\left(v_x+\sqrt{\dfrac{\psi_{mx\delta}}{\beta_\delta}}\right), & x_m<x<x_s. \end{cases} \end{aligned} \tag{4.63}$$

Particle Density:

$$n_\delta = \frac{1}{2} n_{s\delta} e^{-\psi_{ms\delta}} \begin{cases} G_1\left(\psi_{mx\delta}\right), & x_p < x < x_m, \\ G_2\left(\psi_{mx\delta}\right), & x_m < x < x_s. \end{cases} \tag{4.64}$$

Particle Flux:

$$F_\delta = \frac{n_{s\delta}}{2\sqrt{\pi\beta_\delta}} e^{-\psi_{ms\delta}}, \tag{4.65}$$

Normalized Temperature:

$$\frac{T_\delta}{T_{s\delta}} = \begin{cases} 1 + \dfrac{2}{3G_1\left(\psi_{mx\delta}\right)}\sqrt{\dfrac{\psi_{mx\delta}}{\pi}} - \dfrac{2}{3\pi\left[G_1\left(\psi_{mx\delta}\right)\right]^2}, & x_p < x < x_m, \\ 1 - \dfrac{2}{3G_2\left(\psi_{mx\delta}\right)}\sqrt{\dfrac{\psi_{mx\delta}}{\pi}} - \dfrac{2}{3\pi\left[G_2\left(\psi_{mx\delta}\right)\right]^2}, & x_m < x < x_s. \end{cases} \tag{4.66}$$

Energy Flux:

$$Q_\delta = n_{s\delta} T_{s\delta} \frac{2 + \psi_{mx\delta}}{2\sqrt{\pi\beta_\delta}} e^{-\psi_{ms\delta}}. \tag{4.67}$$

Brief Discussion of Surface-Emitted Electrons

Surface-emitted electrons can result due to a variety of causes. The two that are considered to be the most relevant to plasma sheaths are secondary electron emission (ejection of electrons from the surface due to particle impact with the surface) and thermionic emission (ejection of electrons from a heated surface).

For secondary electron emission, the gross flux of secondary electrons, $F_{g\delta}$, can be related to the flux of plasma electrons impacting the surface, F_e, by the secondary electron emission coefficient, δ, according to

$$F_{g\delta} = \delta F_e. \tag{4.68}$$

The gross flux of surface-emitted electrons can be related to the density of surface-emitted electrons, at the surface, by the expression

$$F_{g\delta} = \frac{n_{s\delta}}{2\sqrt{\pi\beta_\delta}}. \tag{4.69}$$

Combining Eqs. (4.68) and (4.69) yields

$$n_{s\delta} = 2\sqrt{\pi\beta_\delta}\delta F_e. \tag{4.70}$$

The present work assumes that secondary electrons do not contribute to the production of later secondary electrons. This is reasonable since the secondary electrons should not be accelerated by the sheath to the point where their energy is comparable to the plasma electron energy. It is further assumed that the plasma ions play no role in the production of secondary electrons.

For thermionic emission, the gross emitted-electron flux is given by the Richardson-Dushman equation,[1,2]

$$F_{s\delta} = AT_{s\delta}^2 e^{-\Phi/T_{s\delta}}. \tag{4.71}$$

Here, A is a material dependent parameter and Φ is the work function for the plasma-facing surface held at temperature $T_{s\delta}$. Equation (4.70) can be used for thermionic emission if

$$\delta = \frac{AT_{s\delta}^2}{F_e} e^{-\Phi/T_{s\delta}} \tag{4.72}$$

is used.

Evaluation of the Sheath and Presheath Potentials

Using the particle density and flux expressions obtained in the previous section, a system of nonlinear equations can be found by applying suitable boundary conditions on the electric potential and charge density. The solution of this system of equations yields the electric potential at the wall and the presheath (along with the potential minimum for cases of space-charge saturation). The boundary conditions to be applied are:

Condition 1: The charge density at the presheath/sheath interface is zero.

Condition 2: The presheath is globally quasineutral.

Condition 3: The electric field at the electric potential minimum is zero.

The first condition imposes a reference value on the potential and gives zero electric field at the presheath/sheath interface. Condition 2 states that the integral of the charge density throughout the presheath is zero. This condition can also be expressed by requiring the electric field be zero at the edge-plasma/presheath and presheath/sheath interfaces. The third condition naturally follows from the relationship between the electric field and potential. However, it is considered only for those cases when the location of the minimum is not coincident with the wall, i.e., when space-charge saturation exists. The remainder of this section develops the necessary system of equations to determine the desired potential values by applying these conditions to the expressions determined above for each of the cases discussed.

Before continuing, some new notation must be introduced. The first step is to construct non-dimensional variables so that the resulting expressions will also be unit-less. Secondly, ratios of these non-dimensional variables are introduced since only particular combinations of the non-dimensional variables appear in the final expressions. Rather than using the ion charge state, Z, and the normalized ion temperature, $\tau_i = T_{pi}/T_{pe}$, separately, they are combined into the variable $\zeta \equiv Z/\tau_i$. The ion-to-electron mass ratio, η, and τ_i are combined into $\xi \equiv \sqrt{\eta/\tau_i}$. The normalized secondary electron temperature, $\tau_\delta \equiv T_{s\delta}/T_{pe}$, is also needed.

To incorporate plasma-facing surfaces that are biased with respect to the plasma, a normalized current density is used and defined by

$$\gamma_i = \frac{ZeF_i - e\left(F_e - F_\delta\right)}{Zen_{pi}/2\sqrt{\pi\beta_i}}. \tag{4.73}$$

As seen in Eq. (4.73), γ_i is the ratio of the total charge flux to the maximum ion

charge flux. Defining the normalized current density in terms of the maximum ion current rather than in terms of the maximum plasma electron current is more suitable for studying the present sheath profiles. The reason is the existence of a strict upper limit on γ_i, namely $\gamma_i = 1$. This represents the ion saturation current and is more suitable for describing the sheath opposed to the electron normalized current density which becomes infinite at the ion saturation current. The electron normalized current is similarly defined as

$$\gamma_e = \frac{ZeF_i - e\left(F_e - F_\delta\right)}{en_{pe}/2\sqrt{\pi\beta_e}}, \tag{4.74}$$

and a relationship between γ_i and γ_e is easily determined from the neutralization factor[3],

$$\alpha = \frac{Zn_{pi}}{n_{pe}}, \tag{4.75}$$

which measures the relative densities of electrons and ions. Using the particle flux expressions, Eqs. (4.25), (4.30), (4.35), (4.40), (4.45), (4.50), (4.55), (4.60) and (4.65), the neutralization factor can be written in terms of the ion normalized current density, Eq. (4.73), as

$$\alpha = \frac{1-\delta}{1-\gamma_i}\xi e^{-\psi_{spe}}, \tag{4.76}$$

$$\alpha = \frac{1-\delta e^{-\psi_{ms\delta}}}{1-\gamma_i}\xi e^{-\psi_{mpe}}, \tag{4.77}$$

$$\alpha = \frac{1-\delta e^{-\psi_{ms\delta}}}{e^{-\psi_{spi}}-\gamma_i}\xi e^{-\psi_{mpe}}. \tag{4.78}$$

These equations apply when, respectively: space-charge saturation is not present [Eq. (4.76)]; space-charge saturation is present and the surface is negatively biased, $\phi_s < \phi_p$ [Eq. (4.77)]; and space-charge is present while the surface is positively biased, $\phi_s > \phi_p$ [Eq. (4.78)]. The neutralization factor can also be written in terms of γ_e by

using the same particle flux expressions with Eq. (4.74) to yield

$$\alpha = \xi \left[\gamma_e + (1 - \delta) \, e^{-\psi_{spe}} \right], \tag{4.79}$$

$$\alpha = \xi \left[\gamma_e + \left(1 - \delta e^{-\psi_{ms\delta}} \right) e^{-\psi_{spe}} \right], \tag{4.80}$$

$$\alpha = \xi \left[\gamma_e + \left(1 - \delta e^{-\psi_{ms\delta}} \right) e^{-\psi_{spe}} \right] e^{-\psi_{psi}}. \tag{4.81}$$

If the expression for α in terms of the ion normalized current is equated to the corresponding expression for α in terms of the electron normalized current, the following relationships between γ_i and γ_e are found:

$$\gamma_e = \frac{1 - \delta}{1 - \gamma_i} \gamma_i e^{-\psi_{spe}}, \tag{4.82}$$

$$\gamma_e = \frac{1 - \delta e^{-\psi_{ms\delta}}}{1 - \gamma_i} \gamma_i e^{-\psi_{mpe}}, \tag{4.83}$$

$$\gamma_e = \frac{1 - \delta e^{-\psi_{ms\delta}}}{e^{\psi_{psi}} - \gamma_i} \gamma_i e^{-\psi_{mpe}}. \tag{4.84}$$

It is clear that at the ion saturation current, the electron normalized current diverges.

It should be noted that Eqs. (4.76)–(4.78) are not suitable expressions at the ion saturation current, $\gamma_i = 1$. Since these expressions are used to determine the sheath potentials, the present theory does not rigorously apply at the ion saturation current. However, some information can be obtained from the steps leading to Eqs. (4.76)–(4.78). For the no space-charge saturation case, Eq. (4.76), the only way such a configuration can reach the ion saturation current is for $\delta = 1$, i.e., complete emission from the surface; such a situation is not expected from typical thermionic or secondary emission materials. Thus, it is unlikely that a sheath without space-charge saturation can reach the limit $\gamma_i = 1$. Whenever space-charge saturation is present within the sheath, this limit is obtainable. If the surface is negatively biased with respect to the plasma the condition on the secondary electron emission coefficient is

relaxed such that $\delta = \exp(e\phi_{sm}/T_{s\delta})$. Since $\phi_m \leq \phi_s$ and for most cases of interest the secondary electron temperature is cooler than the plasma electron temperature, one expects that δ is strictly less than unity. Finally, if the surface is positively biased then the situation becomes more complicated since one must know how the sheath potential, ϕ_{ps}, compares with Ze/τ_i. For some cases there might be no singularity in α when $\gamma_i = 1$.

Returning to the evaluation of the sheath potentials, in order to enforce the boundary conditions the charge density, $\rho = e[Zn_i - n_e - n_\delta]$, must be known. Using the expressions for the particle density, namely Eqs. (4.24), (4.29), (4.34), (4.39), (4.44), (4.49), (4.54), (4.29), and (4.34), along with the neutralization factor, the charge densities for the three potential profiles may be written in the form

$$\frac{2e^{\psi_{spe}}}{en_{pe}}\rho\left(x\right) = \frac{1-\delta}{1-\gamma_i}\xi G_1\left(\psi_{pxi}\right) - G_2\left(\psi_{sxe}\right) - \frac{\delta}{\sqrt{\tau_\delta}}G_1\left(\psi_{sx\delta}\right), \tag{4.85}$$

$$\begin{aligned}\frac{2e^{\psi_{mpe}}}{en_{pe}}\rho\left(x\right) &= \frac{1-\delta e^{-\psi_{ms\delta}}}{1-\gamma_i}\xi G_1\left(\psi_{pxi}\right) - G_2\left(\psi_{mxe}\right) \\ &\quad - \frac{\delta}{\sqrt{\tau_\delta}}e^{-\psi_{ms\delta}}G_1\left(\psi_{mx\delta}\right),\end{aligned} \tag{4.86}$$

$$\begin{aligned}\frac{2e^{\psi_{mpe}}}{en_{pe}}\rho\left(x\right) &= \frac{1-\delta e^{-\psi_{ms\delta}}}{1-\gamma_i e^{-\psi_{psi}}}\xi\left[2e^{-\psi_{psi}}G_1\left(\psi_{pxi}\right) - G_1\left(\psi_{sxi}\right)\right] \\ &\quad - G_2\left(\psi_{mxe}\right) - \frac{\delta}{\sqrt{\tau_\delta}}e^{-\psi_{ms\delta}}G_1\left(\psi_{mx\delta}\right).\end{aligned} \tag{4.87}$$

Note that Eqs. (4.86) and (4.87) apply only for $x_p \leq x \leq x_m$ since it is only through this range that the boundary conditions need be applied.

Having expressions for the charge density, the boundary conditions specified on page 69 can now be enforced. For Condition 1, Eqs. (4.85)–(4.87) are evaluated at the presheath/sheath interface, x_b, and set equal to zero. This gives

$$\frac{1-\delta}{1-\gamma_i}\xi G_1\left(\psi_{pbi}\right) = G_2\left(\psi_{sbe}\right) + \frac{\delta}{\sqrt{\tau_\delta}}G_1\left(\psi_{sb\delta}\right), \tag{4.88}$$

$$\frac{1-\delta e^{-\psi_{ms\delta}}}{1-\gamma_i}\xi G_1\left(\psi_{pbi}\right) = G_2\left(\psi_{mbe}\right) + \frac{\delta}{\sqrt{\tau_\delta}}e^{-\psi_{ms\delta}}G_1\left(\psi_{mb\delta}\right), \tag{4.89}$$

$$\begin{aligned}\frac{1-\delta e^{-\psi_{ms\delta}}}{1-\gamma_i e^{-\psi_{psi}}}\xi\left[2e^{-\psi_{psi}}G_1\left(\psi_{pbi}\right)-G_1\left(\psi_{sbi}\right)\right] \\ = G_2\left(\psi_{mbe}\right)+\frac{\delta}{\sqrt{\tau_\delta}}e^{-\psi_{ms\delta}}G_1\left(\psi_{mb\delta}\right).\end{aligned} \tag{4.90}$$

Requiring a globally quasineutral presheath, Condition 2, is implemented by setting the integral of the charge density from x_p to x_b to zero. Changing the integration variable from x to ψ_{xe}, this boundary condition can be written

$$\int_{x_p}^{x_b}\rho\left(x\right)dx=0 \quad \Rightarrow \quad \int_{\psi_{pe}}^{\psi_{be}}\rho\left(\psi_{xe}\right)d\psi_{xe}=0. \tag{4.91}$$

Using Eqs. (4.85)-(4.87), the second boundary condition yields the equations

$$-\frac{\xi}{\zeta}\frac{1-\delta}{1-\gamma_i}\int_0^{\psi_{pbi}}G_1\left(z\right)dz = \int_{\psi_{spe}}^{\psi_{sbe}}G_2\left(z\right)dz + \delta\sqrt{\tau_\delta}\int_{\psi_{sp\delta}}^{\psi_{sb\delta}}G_1\left(z\right)dz, \tag{4.92}$$

$$-\frac{\xi}{\zeta}\frac{1-\delta e^{-\psi_{ms\delta}}}{1-\gamma_i}\int_0^{\psi_{pbi}}G_1\left(z\right)dz = \int_{\psi_{mpe}}^{\psi_{mbe}}G_2\left(z\right)dz + \delta\sqrt{\tau_\delta}e^{-\psi_{ms\delta}}\int_{\psi_{mp\delta}}^{\psi_{mb\delta}}G_1\left(z\right)dz, \tag{4.93}$$

$$\begin{aligned}-\frac{\xi}{\zeta}\frac{1-\delta e^{-\psi_{ms\delta}}}{1-\gamma_i e^{-\psi_{psi}}}\left\{2e^{-\psi_{psi}}\int_0^{\psi_{pbi}}G_1\left(z\right)dz-\int_{\psi_{spi}}^{\psi_{sbi}}G_1\left(z\right)dz\right\} \\ = \int_{\psi_{mpe}}^{\psi_{mbe}}G_2\left(z\right)dz+\delta\sqrt{\tau_\delta}\int_{\psi_{mp\delta}}^{\psi_{mb\delta}}G_1\left(z\right)dz.\end{aligned} \tag{4.94}$$

To conserve space and simplify the appearance of Eqs. (4.92)–(4.94), the integrals are not expanded. However, they are simply expanded by use of the indefinite integrals

$$\int G_1\left(z\right)dz = G_1\left(z\right)+2\sqrt{\frac{z}{\pi}}, \tag{4.95}$$

and

$$\int G_2(z)\,dz = G_2(z) - 2\sqrt{\frac{z}{\pi}}, \tag{4.96}$$

The final boundary condition only applies when the potential minimum position does not coincide with the surface, i.e., existence of space-charge saturation. Condition 3 states that the electric field be zero at the electric potential minimum. By condition 2, the electric field is zero at the presheath/sheath interface. Hence, the total charge between the presheath/sheath iterface and the potential minimum location is zero,

$$\int_{\psi_{be}}^{\psi_{me}} \rho(\psi_{xe})\,d\psi_{xe} = 0. \tag{4.97}$$

Applying this condition to Eqs. (4.86) and (4.87) yields

$$\begin{aligned} -\frac{\xi}{\zeta}\frac{1-\delta e^{-\psi_{ms\delta}}}{1-\gamma_i}\int_{\psi_{pbi}}^{\psi_{pmi}} G_1(z)\,dz &= \int_0^{\psi_{mbe}} G_2(z)\,dz \\ &\quad + \delta\sqrt{\tau_\delta}e^{-\psi_{ms\delta}}\int_0^{\psi_{mb\delta}} G_1(z)\,dz, \end{aligned} \tag{4.98}$$

$$\begin{aligned} -\frac{\xi}{\zeta}\frac{1-\delta e^{-\psi_{ms\delta}}}{1-\gamma_i e^{-\psi_{psi}}}\left\{2e^{-\psi_{psi}}\int_{\psi_{pbi}}^{\psi_{pmi}} G_1(z)\,dz - \int_{\psi_{sbi}}^{\psi_{smi}} G_1(z)\,dz\right\} \\ = \int_0^{\psi_{mbe}} G_2(z)\,dz + \delta\sqrt{\tau_\delta}e^{-\psi_{ms\delta}}\int_0^{\psi_{mb\delta}} G_1(z)\,dz. \end{aligned} \tag{4.99}$$

For the above expressions to be useful, a reference value for the electric potential must be chosen. For simplicity, the potential at the presheath/sheath interface, x_b, is taken to be zero: $\phi(x_b) = 0$. This choice yields ψ_{pe} as the normalized potential drop across the presheath and ψ_{se} across the sheath. The values of ψ_{pe} and ψ_{se} are determined by Eqs. (4.88) and (4.92) for an electric potential that montonically decreases from the edge plasma/presheath interface — no space-charge saturation. Similarly, Eqs. (4.89), (4.93) and (4.98) [Eqs. (4.90), (4.94) and (4.99)] are simultaneously solved to determine ψ_{pe}, ψ_{me} and ψ_{se} for a single-minimum potential profile

under the conditions of space-charge saturation with a negatively (positively) biased surface.

To compute the self-consistent electric potential profile for a given set of parameters (ζ, ξ, δ, γ_i and τ_δ), Poisson's equation must be self-consistently solved. In one-dimension, this is easily accomplished. First re-write Poisson's equation in terms of the normalized potential and $y = x/\lambda_D$, where λ_D is the Debye length, $\lambda_D^2 = \epsilon_0 T_{pe}/n_{pe}e^2$:

$$\frac{d^2\phi\left(x\right)}{dx^2} = -\frac{\rho\left(x\right)}{\epsilon_0} \qquad \rightarrow \qquad \frac{d^2\psi_{xe}}{dy^2} = \frac{\rho\left(y\right)}{en_{pe}}. \tag{4.100}$$

Multiplying this by $2d\psi_{xe}/dy$, the second derivative can be written as a first derviative

$$2\frac{d\psi_{xe}}{dy}\frac{d^2\psi_{xe}}{dy^2} = \frac{d}{dy}\left[\frac{d\psi_{xe}}{dy}\right]^2 \tag{4.101}$$

so that the first integral is

$$\left[\frac{d\psi_{xe}}{dy}\right]^2 = \int^{\psi_{xe}} \frac{2\rho\left(\psi'_{xe}\right)}{en_{pe}} d\psi'_{xe}. \tag{4.102}$$

Note that a change of variables from y to ψ_{xe} was performed in the ρ integration and that ψ'_{xe} is used to distinguish the integration variable from the value of ψ_{xe} on the left-hand side. This expression can be integrated again to yield

$$y = \int^{\psi_{xe}} \left[\int^{\psi'_{xe}} \frac{2\rho\left(\psi''_{xe}\right)}{en_{pe}} d\psi''_{xe}\right]^{-1/2} d\psi'_{xe}. \tag{4.103}$$

Using Eq. (4.103), the appropriate expression of the charge density [that is, Eqs. (4.85)–(4.87)] is integrated from x_p to x to yield

$$\frac{x}{\lambda_D} = \int_{\psi_{pe}}^{\psi_{xe}} \left[\int_{\psi_{pe}}^{\psi'_{xe}} \frac{2\rho\left(\psi''_{xe}\right)}{en_{pe}} d\psi''_{xe}\right]^{-1/2} d\psi'_{xe}. \tag{4.104}$$

Recall that Eqs. (4.86) and (4.87) are only valid between x_p and x_m so that the charge density expression must be re-evaluated using the particle densities appropriate for

$x_m \leq x \leq x_s$ to determine the correct form of the charge density for use in Eq. (4.104).

Another point of interest beyond the value of the potentials is the transition to space-charge saturation as well as from a negatively to a positively biased surface. These situations can also be determined from the expressions presented above. One difference between the absence and presence of space-charge saturation is the location of the electric potential minimum. If there is no space-charge saturation, the minimum coincides with the surface yielding a monontonic profile. However, when space-charge saturation is present the value of the electric potential differs from the value at the surface, Thus, if the replacement $\psi_{me} = \psi_{se}$ is made in Eqs. (4.89), (4.93) and (4.98) and the resulting equations are simultaneously solved for ψ_{pe}, ψ_{se} and δ, then the value of δ is the desired critical value, δ_c. Similarly, the transition from a negatively biased to a positively biased surface occurs when ψ_{se} equals ψ_{pe}. Thus, replacing each occurence of ψ_{pe} with ψ_{se} in Eqs. (4.90), (4.94) and (4.99) and solving for ψ_{me}, ψ_{se} and δ yields the desired values at the transition.

Approximate Expressions

With the appropriate system of equations from the previous section, the value of the electric potential throughout the the presheath and sheath can be determined. Unfortunately, a highly non-linear system of equations must be simultaneously solved. To facilitate the evaluation of the presheath, minimum and sheath potentials as well as the critical electron emission coefficient, approximate expressions for these values are presented. These approximate expressions were obtained by solving the system of equations over a range of parameter values and determining a suitable formula that reproduces the calculated values within an acceptable amount of error. The parameter

$\zeta = \dfrac{Z}{\tau_i} = \dfrac{ZT_{pe}}{T_{pi}}$	0.2, 1, 5
$\xi = \sqrt{\dfrac{\eta}{\tau_i}} = \sqrt{\dfrac{m_i T_{pe}}{m_e T_{pi}}}$	20, 50, 100, 500, 1000
$\gamma_i = \dfrac{eZF_i - e\left(F_e - F_\delta\right)}{Zen_{pi}\sqrt{2\pi m_i / T_{pi}}}$	-0.5, 0.0, +0.5
$\tau_\delta = \dfrac{T_{s\delta}}{T_{pe}}$	0.01

Table 4.1. Parameter values used in obtaining the fits.

values used for these fits are presented in Table 4.1 except where specifically noted. For each parameter value, all other parameters were varied over their entire specified ranges. The single value of τ_δ is chosen since the potentials are effectively independent of the surface-emitted electron temperature when $\tau_\delta < 0.1$.

When the secondary electron emission coefficient is less than a critical value, δ_c, the electric field at the material surface is non-zero and points away from the surface while the electric potential minimum coincides with the surface. If $\delta > \delta_c$, there is still a non-zero electric field at the surface. However, it now points toward the surface and impedes the escape of more surface-emitted electrons. Furthermore, the electric potential minimum no longer coincides with the surface. For the particular case that the emission coefficient equals this critical value, the potential is still a minimum at the surface but the surface electric field is now zero. An expression that describes the critical secondary electron emission coefficient value is

$$\delta_c = 1 - \frac{2.9\zeta^{0.28}\left(1-\gamma_i\right)^{0.7}}{\xi^{0.79}}. \tag{4.105}$$

$$\left(0.2 \leq \zeta \leq 5,\ 20 \leq \xi \leq 1000,\ |\gamma_i| \leq 0.5\right)$$

Determined by solving Eqs. (4.89), (4.93) and (4.98), under the condition that $\psi_{me} = \psi_{se}$, for the values stated in Table 4.1, this expression agrees to within 4% of the numerically determined values. Beneath the expression for δ_c are the parameter ranges for which this expression lies within the stated error. As expected, the value of δ_c is less than one.

For sheaths that are not space-charge saturated, the electric potential monotonically decreases from its value at the edge-plasma/presheath interface, as previously shown in Fig. 4.4(a). When $\delta < \delta_c$, the following two expressions yield the values for the normalized presheath and sheath potentials to within 7% of the numerically determined values from Eqs. (4.88) and (4.92):

$$\psi_{pe} = -0.288 \ln\left[1 + 2.07\zeta\right] \left(1 + \frac{0.45\zeta\gamma_i}{\xi}\right) \left(1 + \frac{0.19\delta^{1.4}}{\zeta^{0.3}}\right), \tag{4.106}$$

$$\begin{aligned} \psi_{se} \;\; = \;\; & \ln\left[0.4715\xi\frac{1-\delta}{1-\gamma_i}\right] \\ & - 0.5 \ln\left[1 + 1.61\zeta\right] \left(1 + \frac{1.3\gamma_i}{\zeta^{0.56}\xi}\right) \left(1 + 0.208\xi^{0.041}\delta^{1.3}\right). \end{aligned} \tag{4.107}$$

$$(0.2 \leq \zeta \leq 5,\ 20 \leq \xi \leq 1000,\ |\gamma_i| \leq 0.5,\ \delta \leq \delta_c)$$

Having set the electric potential to zero at the presheath/sheath interface, $\psi_{be} = 0$, one location subscript is used since $\psi_{pbe} = \psi_{pe}$. Note that two values of the secondary electron emission coefficient were used to determine these fits, $\delta = 0,\ \delta_c$.

Under conditions of space-charge saturation, the secondary electron emission coefficient must exceed a critical value, $\delta > \delta_c$. For such cases, an electric potential minimum occurs within the sheath. If the surface remains negatively biased with respect to the edge plasma, the normalized presheath, minimum and sheath potentials

can be described by the following expressions:

$$\psi_{pe} = -0.271 \ln\left[1 + 3\zeta\right] \left(1 + \frac{0.57\zeta\gamma_i}{\xi}\right), \tag{4.108}$$

$$\begin{aligned} \psi_{me} &= 0.0864 - 0.0101\zeta + \left(0.626 + 0.121\zeta - 0.0181\zeta^2\right)\delta_c \\ &\quad - \left(0.128 + 0.0416\zeta - 0.00549\zeta^2\right)\delta_c^2, \end{aligned} \tag{4.109}$$

$$\psi_{se} = \psi_{me} - 0.00693\left(1 - 0.074\delta\right)\delta. \tag{4.110}$$

$$\left(0.2 \le \zeta \le 5,\ 20 \le \xi \le 1000,\ |\gamma_i| \le 0.5,\ \delta_c \le \delta \le 6\right)$$

These expression agree to within 7%, 3.5% and 3%, respectively, of the numerical values determined by simultaneously solving Eqs. (4.89), (4.93) and (4.98) for the parameter values specified in Table 4.1 as well as $\delta = \delta_c$, 1.5, 3.0, 6.0.

To obtain a surface positively biased with respect to the edge plasma, a significant flux of emitted electrons is necessary. Although this phenomenon has been observed,[4] it is expected to occur only for floating surfaces with large thermionic current densities and anode surfaces with large current densities. Equations (4.108)–(4.110) do not apply to such cases and are limited to $\psi_{pe} < \psi_{se}$.

Effects of Parameters on the Sheath Potential

Having presented the equations required to determine the value of the sheath potentials and the approximate expressions, it remains to demonstrate how the parameter values affect the value of the sheath potentials. This section investigates these effects by numerically solving the appropriate system of sheath potential equations as the value of one parameter is varied while the other parameters are held constant. As before, the case of a positively biased surface is not considered due to the extreme

conditions required to achieve such a potential profile. Thus, only the cases of no space-charge saturation and space-charge saturation with a negatively biased surface are examined.

A common set of parameter values (excluding the secondary electron emission coefficient) is chosen for both cases of space-charge saturation. Since the actual physical parameters, such as the ion temperature (T_{pi}), ion charge state (Z) and ion mass (m_i), occur only within certain combinations, i.e., $\zeta = ZT_{pe}/T_{pi}$, these aggregrate parameters are discussed. This allows a broader range of phenomena to be discussed since variation in ζ can be realized by varying the ion charge state, ion temperature or the plasma electron temperature. The only physical parameter that is directly considered is the secondary electron emission coefficient, δ, since it never appears in combination with any other parameters. The base parameter values are $\tau_\delta = 0.01$, $\xi = 200$, $\zeta = 5$ and $\gamma_i = 0$. Since δ is the primary indicator of the existence of space-charge saturation, its value is either 0 when space-charge saturation is absent or 1 when it is not. Furthermore, to effectively discuss the effect of δ, the secondary electron temperature must be sufficient for these particles to take an active role within the sheath. Therefore, $\tau_\delta = 0.25$ is used when the effect of δ is considered. It would be reasonable to discuss the two cases of space-charge saturation separately, it is just as reasonable to discuss them simultaneously in order to demonstrate how significantly the degree of space-charge saturation affects the sheath. Finally, to continue the generality for applicability over a broad range of physical phenomena, the normalized potentials, $\psi_{se} = -e\phi(x_s)/T_{pe}$ and $\psi_{pe} = -e\phi(x_p)/T_{pe}$, are plotted as opposed to the electric potential itself.

A convenient starting point in discussing the parameter effects on the sheath po-

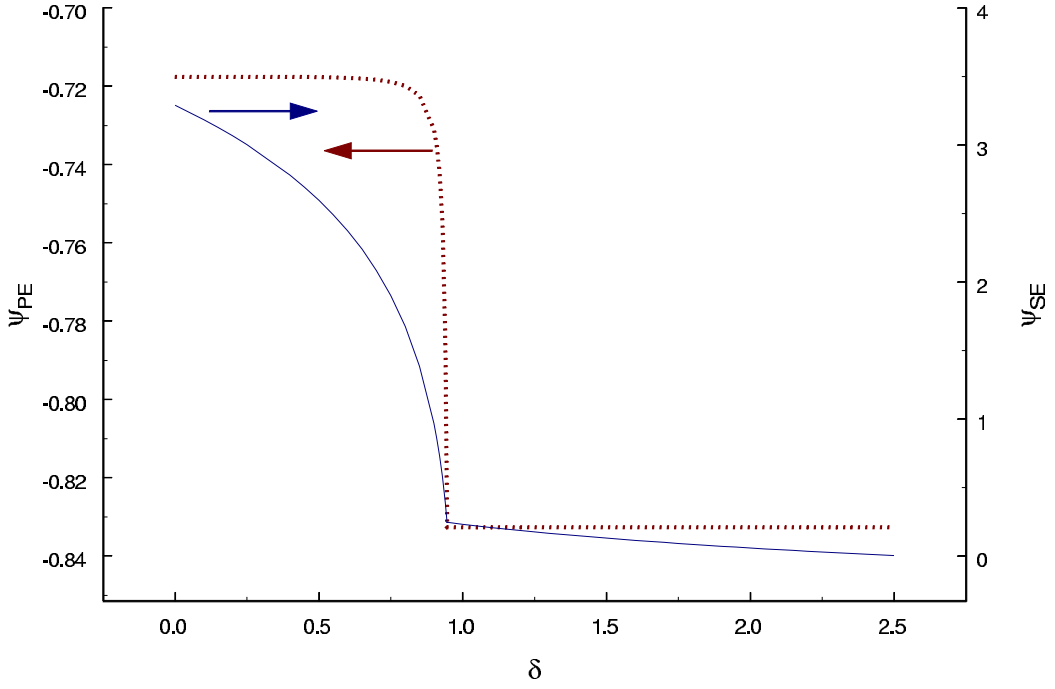

FIG. 4.5. Edge plasma (dashed) and surface (solid) potential variation for changes in the secondary electron emission coefficient. The transition to space-charge saturation occurs near $\delta = 0.95$. The potential at the edge plasma suffers a drastic change as the sheath becomes space-charge saturated but then remains effectively constant. The surface potential continues to be effected by δ past the transition, although to a lesser extent.

tentials is the secondary electron emission coefficient, δ, since it is perhaps the most important parameter in distinguishing the degree of space-charge saturation. Figure 4.5 shows the edge plasma and surface potentials as the secondary electron emission coefficient is varied from 0 to 2.5. For the other parameter values stated earlier, the transition to space-charge saturation occurs around $\delta = 0.95$ and is clearly evident from the figure. Although the surface potential has the larger change in value, the potential at the edge plasma displays the greatest dependence on δ. Although remaining essentially constant within the regimes of space-charge saturation, ψ_{pe} changes drastically as the transition point is approached. Figure 4.5 also demonstrates the rather

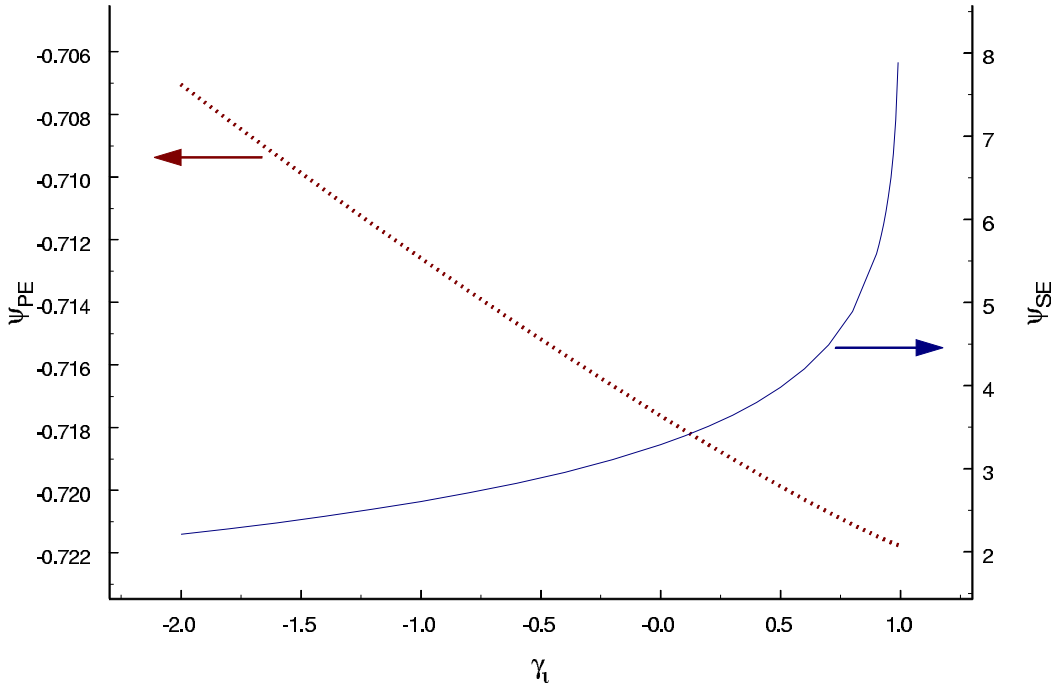

FIG. 4.6. Normalized edge plasma (dashed) and surface (solid) potential dependence on the normalized current density. The edge plasma bears little effect from variations in γ_i. The surface potential displays an asymptote at $\gamma_i = 1$, at which point the theory breaks down.

large emission coefficient required for the surface to become positively biased with respect to the edge plasma. Since ψ_{se} varies linearly with δ in the space-charge saturation regime and ψ_{pe} is essentially constant, the value of δ for this second transition is estimated by linearly extrapolating ψ_{se} to be equal to ψ_{pe} and is found to be ~ 6.9.

Perhaps the second-most important parameter for distinguishing the regimes of space-charge saturation is the normalized current density, γ_i. As the emission coefficient controls the amount of negative charge present near the surface, γ_i dictates the direction of charge flow and therefore whether the surface acquires more or less negative charge. To demonstrate this, Fig. 4.6 shows the edge plasma and surface potential as the normalized current density is varied up to the ion saturation current,

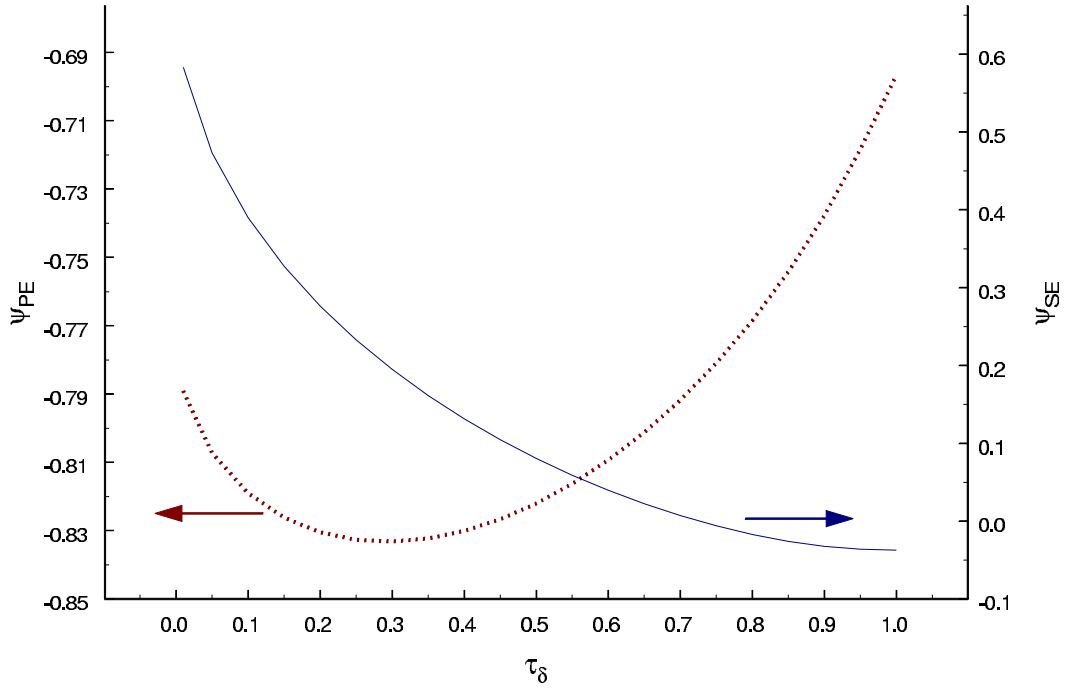

FIG. 4.7. Normalized edge plasma (dashed) and surface (solid) potential variation for changes in the secondary electron temperature under conditions of space-charge saturation ($\delta = 1$). The edge plasma has an inflection point near $\tau_\delta = 0.3$ while the surface potential monotonically decreases as the secondary electron temperature approaches the plasma electron temperature.

$\gamma_i = 1$. As the normalized current density moves aways from this saturation value, the number of ions travelling toward the surface decreases, effectively increasing the amount of negative charge there. Therefore, near $\gamma_i = 1$ the normalized surface potential should be larger than for $\gamma_i \ll 1$. As for the secondary electron emission coefficient, the potential at the edge plasma shows only slight variation.

Figure 4.7 shows the normalized edge plasma and surface potentials as functions of the secondary electron temperature in the space-charge saturated regime. When the space-charge saturation is absent, there are insufficient secondary electrons to significantly affect the potentials and that case is thus not considered. As expected

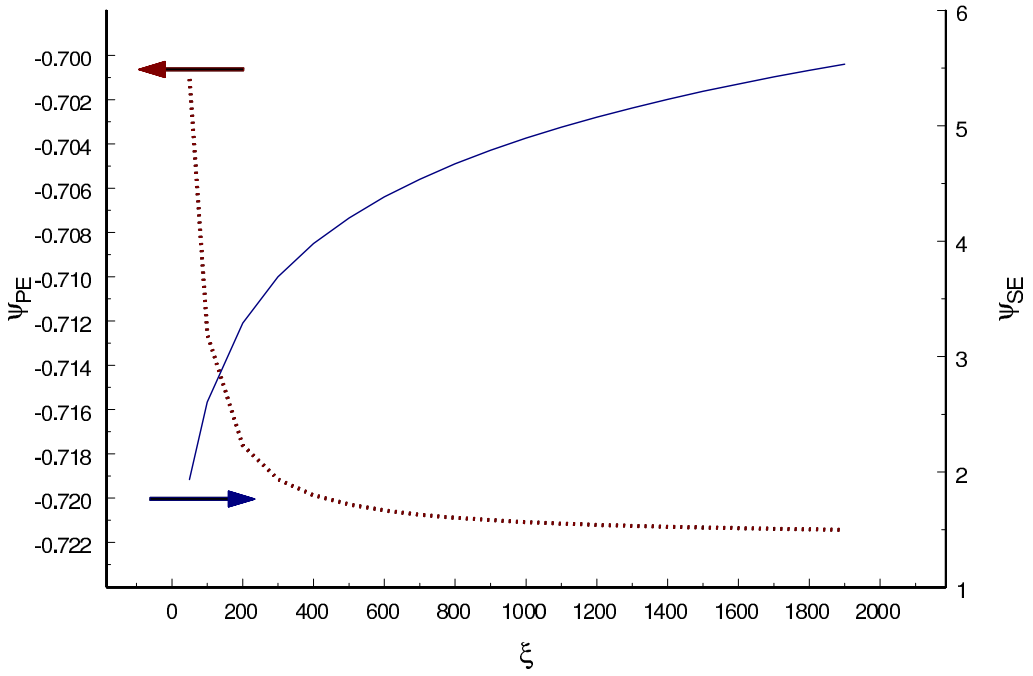

FIG. 4.8. Normalized edge plasma (dashed) and surface (solid) potential variation for changes in the parameter $\xi = \sqrt{m_i T_{pe}/m_e T_{pi}}$ for space-charge densities below saturation. The normalized surface potential varies linearly with $\ln(\xi)$ whereas the normalized potential at the edge plasma rapidly decreases with increasing ξ.

and shown in the figure, τ_δ has a major effect on the surface potential. Secondary electrons emitted with larger kinetic energies enables them to travel farther into the sheath and the surface becomes increasingly more positive (recall that the normalized potential is proportional to the negative of the electric potential, $\psi_{se} = -e\phi(x_s)/T_{pe}$).

The effect of varying the ion mass or temperature is demonstrated by plotting the normalized edge plasma and surface potentials against the parameter ξ, as shown in Fig. 4.8 when space-charge saturation is absent and Fig. 4.9 when it is present. The similarities between these two cases are that both boundaries depend monotonically on ξ with ψ_{pe} decreasing and ψ_{se} increasing as ξ increases. Also, the potential at the edge plasma displays only minor changes over the entire range. For the no saturation

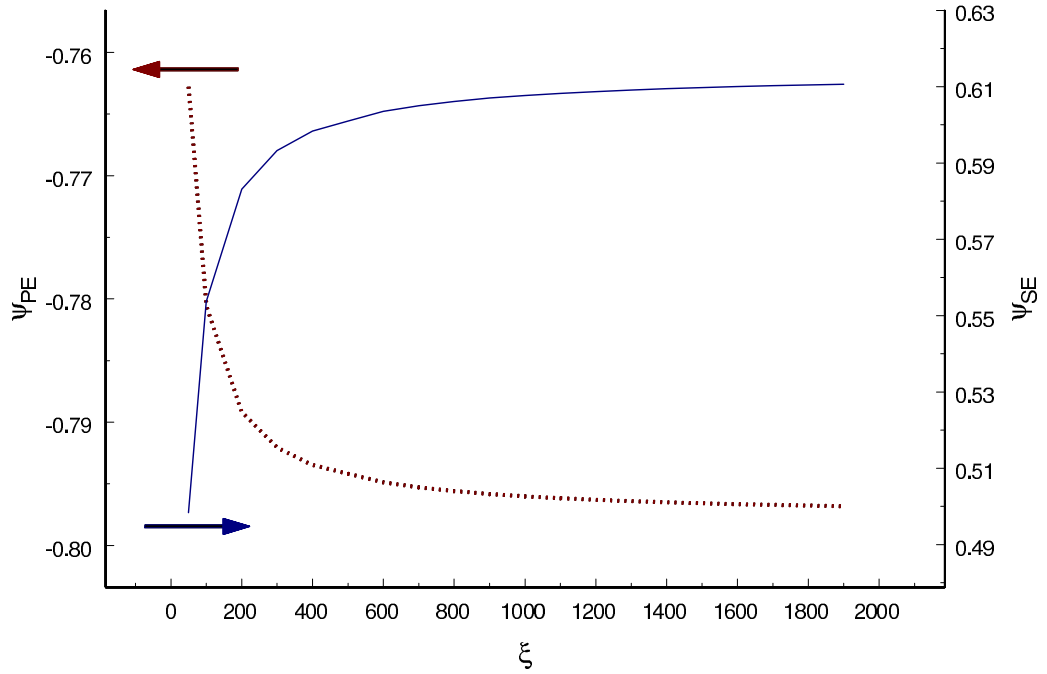

FIG. 4.9. Normalized edge plasma (dashed) and surface (solid) potential variation for changes in the parameter $\xi = \sqrt{m_i T_{pe}/m_e T_{pi}}$ when space-charge saturation is present. The edge plasma potential varies similarly as in the no space-charge saturation case. The surface potential depends on ξ much more heavily when space-charge saturation is present.

case, the normalized surface potential shows a linear dependence on $\ln(\xi)$ whereas the dependence is much stronger when in the space-charge saturation regime.

The final parameter to be discussed involves the ion charge state as well as the plasma ion to electron temperature ratio, $\zeta = ZT_{pe}/T_{pi}$. The manner in which ψ_{pe} and ψ_{se} depend on ζ is shown in Fig. 4.10 for no space-charge saturation and Fig. 4.11 for space-charge saturation. For both cases, the normalized edge plasma potential monotonically decreases with increasing ζ. The numerical values for these two curves are very similar, starting at -0.053 (-0.074) and ending at -0.854 (-0.927) when space-charge saturation is absent (present). On the other hand, the surface potential

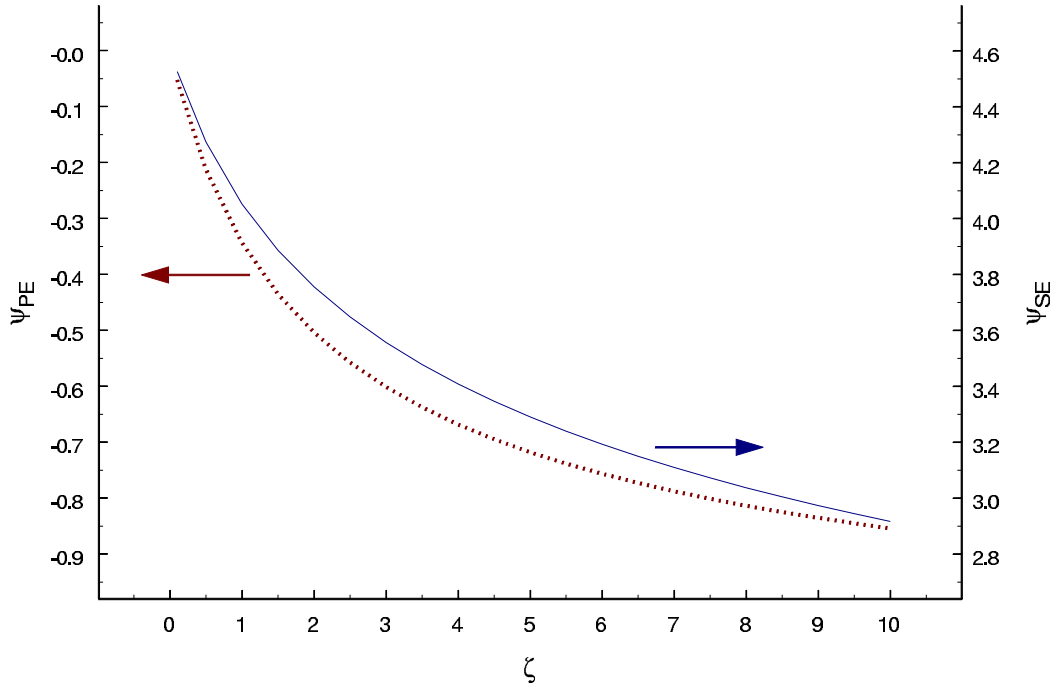

FIG. 4.10. Normalized edge plasma (dashed) and surface (solid) potential variation for changes in the parameter $\zeta = ZT_{pe}/T_{pi}$ when space-charge saturation is absent. Both potentials display a similar dependence on ζ with the surface potential carrying a much stronger dependence.

shows a marked difference between the two cases of space-charge saturation. When the sheath is space-charge saturated, ψ_{se} shows a symmetry line at $\zeta = 1$ in terms of $\ln \zeta$, i.e., the value of ψ_{se} is essentially the same for ζ and $1/\zeta$.

Profiles of Some Distribution Function Moments

Having discussed the effect of varying the plasma and surface parameters on the electric potential at the edge-plasma and material surface, it is also instructive to consider the profiles of the particle density, normalized temperature and energy flux. The profiles of these quantities are given for each species and are determined by the expressions given on pages 61–68. Since these moments depend upon the potential

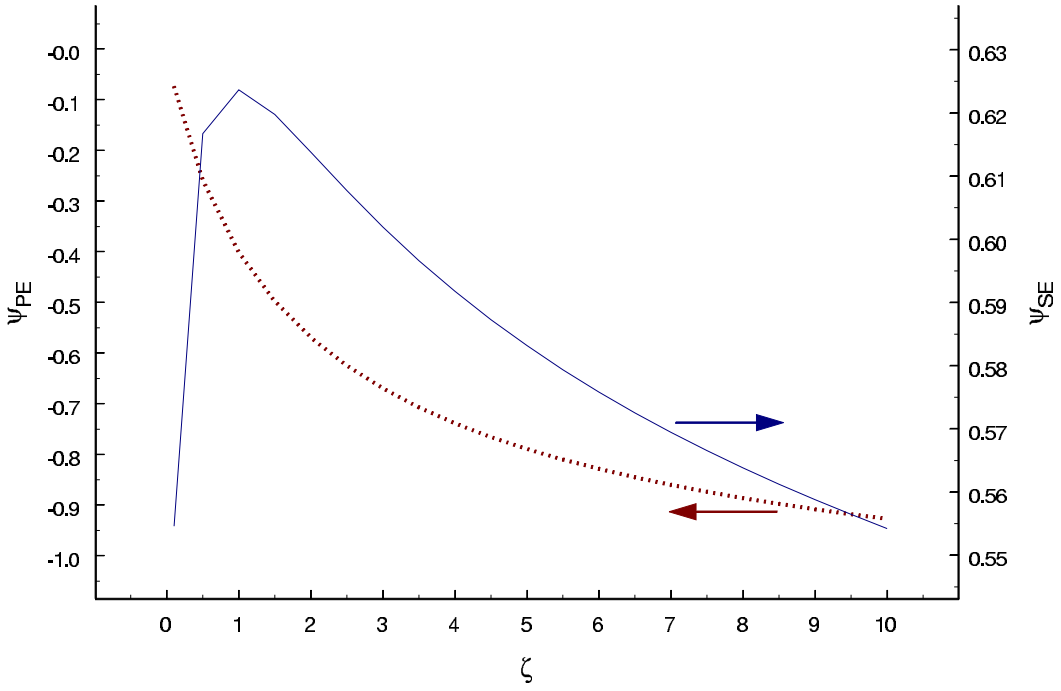

FIG. 4.11. Normalized edge plasma (dashed) and surface (solid) potential variation for changes in the parameter $\zeta = ZT_{pe}/T_{pi}$ when space-charge saturation is present. The normalized edge potential shows the same dependence on ζ regardless of the degree of space-charge saturation. The normalized surface potential is essentially symmetrical in $|\ln \zeta|$ about $\zeta = 1$.

throughout the sheath, Poisson's equation, Eq. (4.104), must be integrated using the appropriate values of the potential, ψ_{pe} and ψ_{se} (as well as ψ_{me} for the case of space-charge saturation). As previously mentioned, Eq. (4.86) cannot be used to determine the potential between x_m and x_s since it only applies for $x_p \leq x \leq x_m$. The appropriate terms from Eqs. (4.39), (4.44) and (4.49) can be used, however, to reconstruct $\rho(x)$ for the range $x_m \leq x \leq x_s$ and Poisson's equation can then be integrated again to yield the remaining portion of the electric potential profile.

Once all the relevant charge densities have been constructed, the task of integrating Poisson's equation can then be tackled. Since the first integral of Poisson's

equation involves simply integrating the charge density with respect to ψ_{xe}, this can be performed algebraically. Unfortunately, the second integral requires the integration of the inverse square-root of the first integral and must be handled numerically. Furthermore, some care must be taken in actually integrating this result. By Condition 1 on page 69, the charge density is zero at x_b, the presheath/sheath interface. This implies that the first integral is likewise zero at x_b. Thus, the integrand for the second integral of Poisson's equation diverges near this point and the numerical integration must be able to handle such a situation. For the case of space-charge saturation, the integrand also diverges at x_m. The normalized potential profiles used in this section were calculated by separately integrating Poisson's equation on each side of the singularities and then combining the results to form the complete profile. Once the normalized electric potential is known throughout the sheath, the moments (particle density, normalized temperature and energy flux) were calculated for each particle species (plasma ions, plasma electrons and surface electrons). In order to maintain uniformity for each profile and to avoid specifying any specific particle densities, each moment was normalized. For the plasma electrons, for example, the particle density was divided by n_{pe} while the energy flux was divided by $n_{pe}T_{pe}/\sqrt{\beta_e}$. The same was done for the plasma ions and secondary electrons using their respective values.

Figure 4.12 shows the normalized electric potential as well as the particle density, normalized temperature and energy flux for each species when space-charge saturation is absent. Since $\psi_{xe} = -e\phi(x)/T_{pe}$, the monotonically decreasing electric potential is shown as a monotonically increasing profile. The parameter values used to create these profiles are $\tau_\delta = 0.25$, $\delta = 0.5$, $\xi = 200$, $\zeta = 5$ and $\gamma_i = 0$, resulting in $\psi_{pe} = -0.7177$ and $\psi_{se} = 2.597$. For this case, the sheath extends over 32 Debye

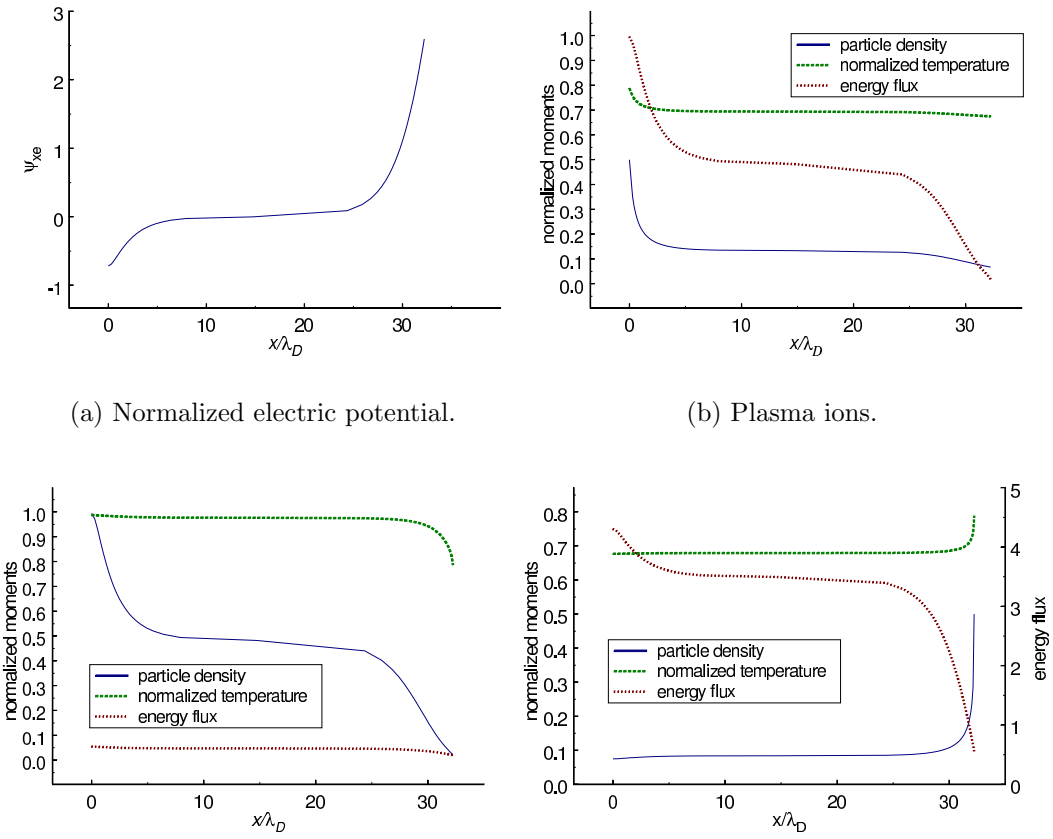

(a) Normalized electric potential.

(b) Plasma ions.

(c) Plasma Electrons

(d) Surface electrons

FIG. 4.12. Profiles of the normalized electric potential and of some normalized moments for the three particles species under the condition of no-space-charge saturation.

lengths away from the surface. In order to determine the Debye length, however, specific values for the temperature and particle density within the edge-plasma must be given. Lying below the space-charge saturation regime, the low surface electron density shown in Fig. 4.12(d) is expected with the particle density equaling 0.5 at the surface. Note the large surface electron energy flux away (recall that positive fluxes for the surface electrons are positive away from the surface) from the surface. This is expected since only energetic electrons can escape from the surface due to the large

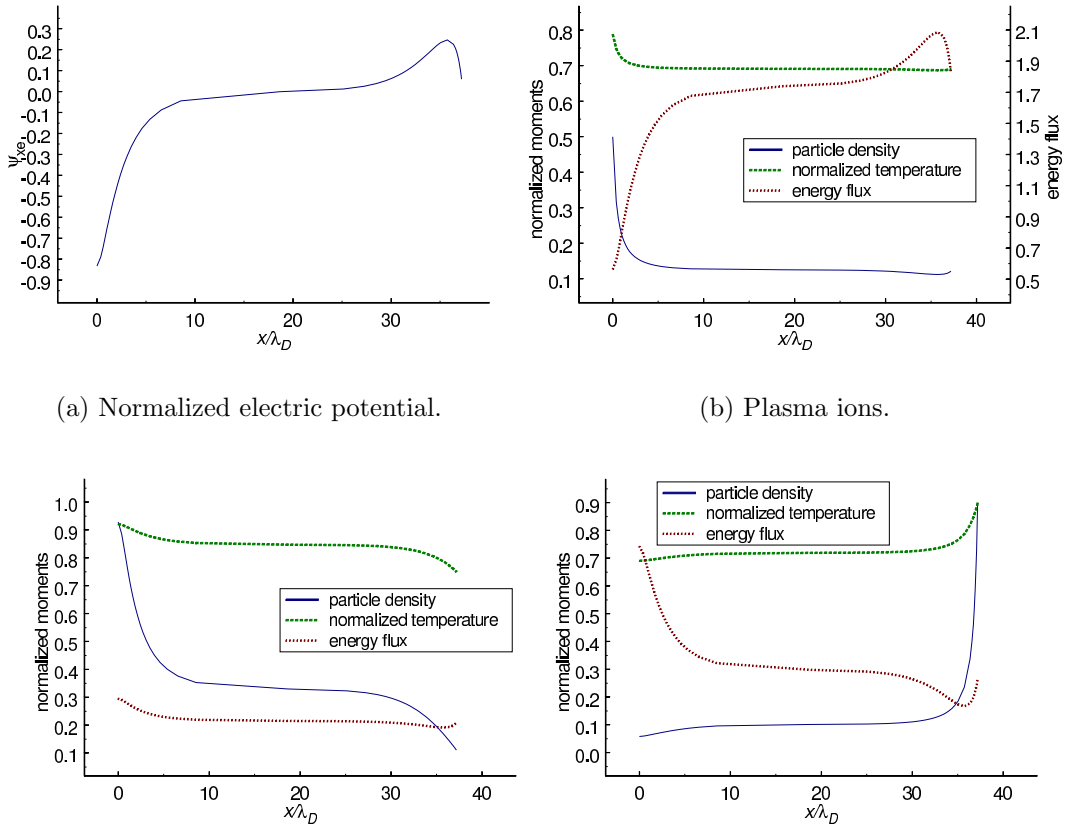

(a) Normalized electric potential.

(b) Plasma ions.

(c) Plasma Electrons

(d) Surface electrons

FIG. 4.13. Profiles of the normalized electric potential and of some normalized moments for the three particles species when the sheath is space-charge saturated.

surface potential, $\psi_{se} = 2.597$.

The same profiles for the normalized electric potential and moments are shown in Fig. 4.13 for the case of space-charge saturation and a negative bias surface. The presence of a potential depression near the surface, indicating the presence of space-charge saturation, is evident from the normalized potential profile shown in Fig. 4.13(a). The parameters used to creates these profiles are the same as before, except that $\delta = 2$. This value of the secondary electron emission coefficient is approximately

twice that of the transition value, $\delta_c \sim 0.945$. The entire sheath extends more than 37 Debye lengths into the edge-plasma and the normalized potential has the values $\psi_{pe} = -0.8327$, $\psi_{me} = 0.2472$ and $\psi_{se} = 0.05978$. These values indicate that the sheath is in the space-charge saturation regime but far from the transition to a positive surface (for which ψ_{se} would equal ψ_{pe}). Inspection of the plasma electron particle density shows a significant decrease compared to the no space-charge saturated case. Likewise, the surface electrons display a much higher concentration. However, compared to the no saturation case, the surface electron energy flux is considerably smaller, especially near the surface. Since the surface potential for the present case is only a couple percent of that for the no space-charge saturation value, more low energy electrons escape the surface and the half-Maxwellian distribution weighs them more heavily than the more energetic particles.

Having discussed the normalized potential, particle density, normalized temperature and energy flux profiles as a function of position, their parameter dependence at the edge-plasma and material surface are now presented. For simplicity, only the secondary electron emission coefficient is considered. Since δ plays most dominately in affecting the degree of space-charge saturation, it seems the most suitable parameter to discuss. Thus, using the parameter values $\tau_\delta = 0.25$, $\xi = 200$, $\zeta = 5$ and $\gamma_i = 0$, each moment is presented at the edge-plasma, x_p, and the material surface, x_s, for each species. The plasma ions are not shown at x_p since these moments are constant for the two cases of space-charge saturation considered. Recall that the transition to space-charge saturation occurs at $\delta = 0.945$.

Figure 4.14 shows the particle densities at the edge plasma for the electrons and at the surface for all three species. The plasma electrons maintain a very high den-

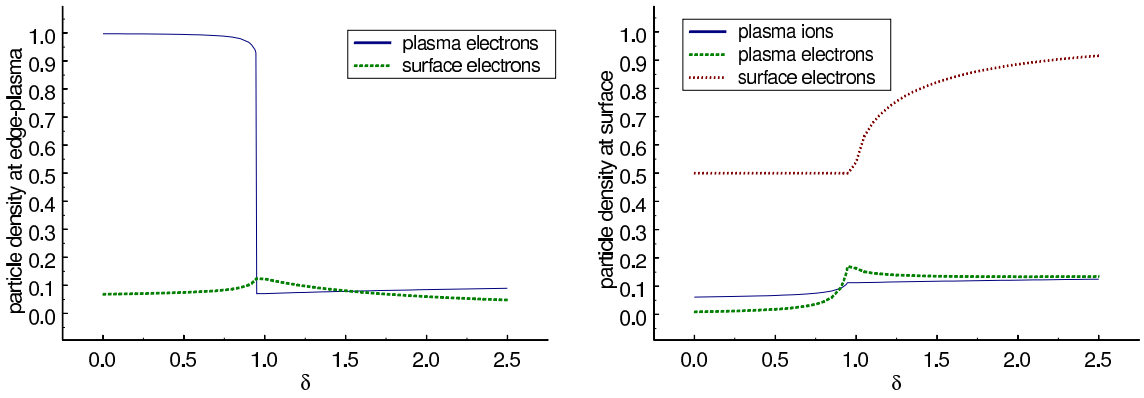

(a) At the edge-plasma.

(b) At the material surface.

FIG. 4.14. Profiles of the normalized particle density for each species at the edge-plasma and the material surface as a function of the secondary electron emission coefficient.

sity at the edge-plasma until the sheath becomes space-charge saturated, at which point their density diminishes significantly. Similarly, the surface electron density increases until the transition and then decreases below its pre-transition value. This behavior can be explained by recalling that the electron particle densities depend most heavily on the surface potential as well as how ψ_{se} depends upon δ, Fig. 4.5. As the emission coefficient is increased, the surface potential decreases because of the increased secondary electron space-charge. This allows more surface electrons to be emitted (because of the greater number of low-velocity electrons able to overcome the potential barrier) and allows fewer plasma electrons to be reflected by the surface potential. This change in ψ_{se} also explains the profiles at the material surface. The small plasma electron density below δ_c results from the large surface potential, which prevents these electrons from nearing the surface. As for the plasma ions near the surface, their density profile closely follows the potential profile. Hence, as the surface

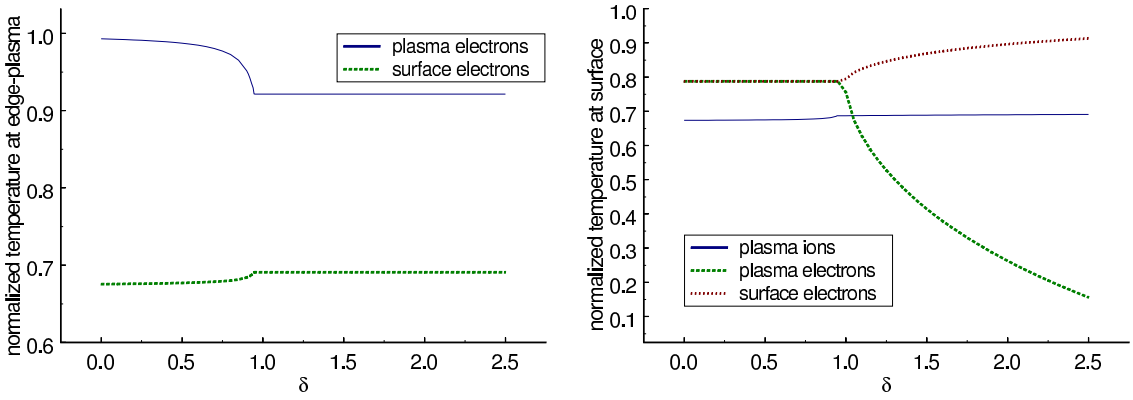

(a) At the edge-plasma.

(b) At the material surface.

FIG. 4.15. Profiles of the normalized temperature for each species at the edge-plasma and the material surface as a function of the secondary electron emission coefficient. Note the different vertical scales between the two positions.

potential increases, the ion density also increases.

The normalized temperature profiles are shown in Figure 4.15. Comparing the electron temperatures at both interfaces indicates a complementary effect: While the temperature at one interface changes, the temperature at the other remains constant. This behavior results from the variation of ψ_{pe} and ψ_{se} (or ψ_{me} for space-charge saturation), shown in Fig. 4.5, and the fact that the spatial variation of T_e and T_δ is through ψ_{se} or ψ_{me}. Since the temperatures are evaluated only at the edge-plasma and the surface, this dependence reduces to the total sheath potential: ψ_{spe} for no space-charge saturation and ψ_{mpe} for space-charge saturation. Since neither the edge-plasma potential nor the potential minimum significantly vary after the transition to space-charge saturation, the temperatures at x_p reflect this lack of change. In the same regime, the surface potential continues to change and produces the seen variations at x_s. As for the plasma ions, their large inertia prevents much change in

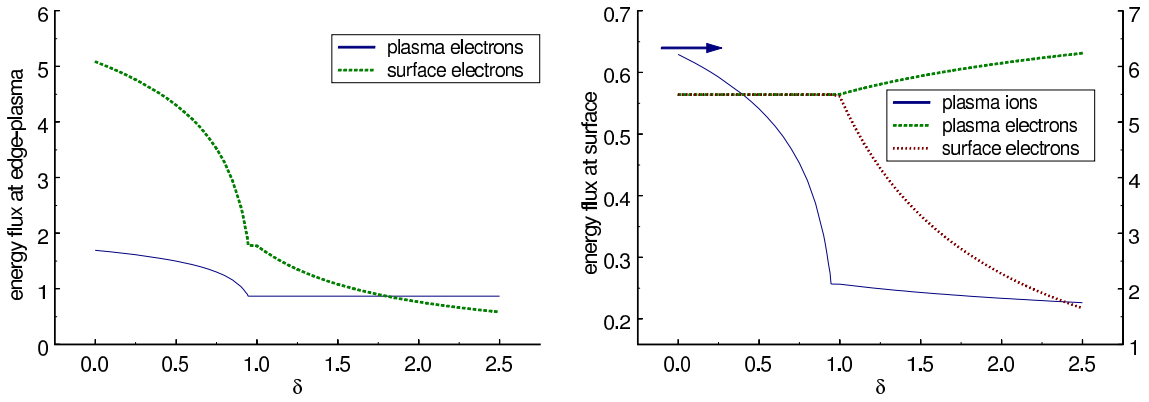

(a) At the edge-plasma.

(b) At the material surface.

FIG. 4.16. Profiles of the normalized energy flux for each species at the edge-plasma and the material surface as a function of the secondary electron emission coefficient.

their temperature at either end of the sheath.

Finally, the energy flux for each species is shown in Fig. 4.16. Although similar to the normalized temperature shown earlier, the most marked difference is the variation of Q_δ at the edge-plasma once the sheath is space-charge saturated and the vast variation in Q_i through the non-saturated sheath. Both of these effects are easily explained by consideration of the potential energies of each species. As the surface potential decreases in magnitude (recall that it is negative), the ion acceleration produced by the sheath potential decreases. This results in a similar decrease in the plasma ion energy flux. Since ψ_{se} varies most quickly for $\delta < \delta_c$ and only slowly after that, Q_i readily parallels that variation (see Fig. 4.5). At the edge-plasma, the surface electron energy flux is quite large near $\delta = 0$ since these particles are quickly accelerated away from the surface by the large surface potential. As this potential decreases, the energy flux likewise diminishes. After the transition to space-charge

saturation, the surface potential might continue to decrease (allowing more surface particles to enter the sheath) but the barrier introduced by the potential minimum reflects many of these particles. Furthermore, the particles that do pass x_m are no longer accelerated as greatly as in the case of no space-charge saturation.

Particle Simulation of Sheath Development

Using the fully kinetic planar sheath model, a theoretical description of the sheath has been obtained. Although numerical solution of the involved equations is required, the theory provides a complete decription of the sheath. In this section, a particle-in-cell (PIC) computer simulation of the sheath is presented. PIC simulations employ thousands of particles to model the collective behavior of the plasma. The program uses Lorentz forces, calculated from the self-consistent particle densities and currents, to advance the particles through phase space. The entire calculation takes place on a fixed mesh and uses a constant timestep for each computational cycle. Appendix B provides more details on PIC methods and provides references for more information.

The simulation models an initially empty region, $0 \leq x \leq L$, between an electrically floating surface and a source of hydrogen plasma. Plasma electrons and ions are injected into this region, at $x = L$, with equal and constant current densities. Since the computation time increases with ion mass, sub-cycling is used on the ions. For a hydrogen plasma, the ion mass is 1836 times the electron mass. Thus, advancing each species every cycle would require an extremely long run-time in order to completely advance the ions. Sub-cycling overcomes this by advancing the ions only every 40 cycles, using a timestep of 40 times that used for the electrons. The value 40 is chosen since $40 < \sqrt{1836}$ — the ion velocities are approximately 40 times less than the electron velocities. Each species is given a thermal velocity associated with the

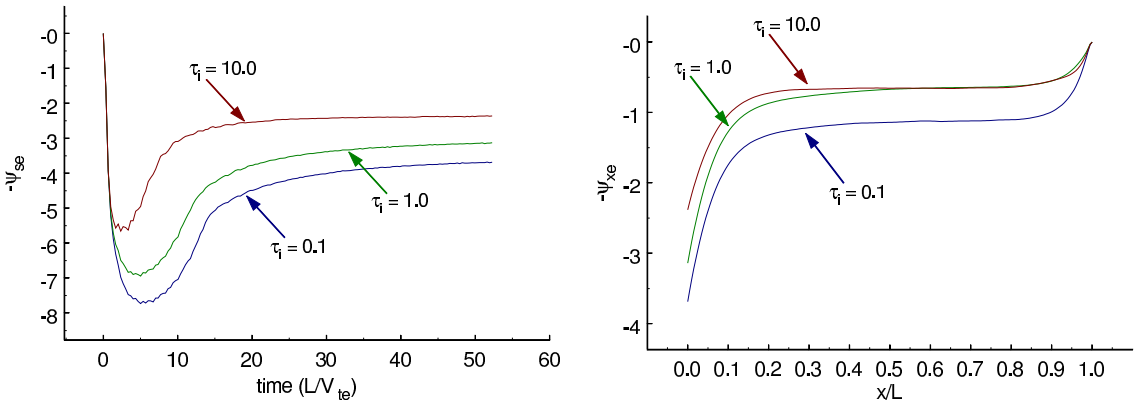

(a) surface potential history

(b) steady-state profiles

FIG. 4.17. History of the normalized surface potential and resulting steady-state sheath profile for a hydrogren plasma with various ion-to-electron temperature ratios: $\tau_i = T_{pi}/T_{pe} = 0.1, 1.0, 10.0$.

plasma source and injected using a half-Maxwellian distribution.

In order to maintain a certain degree of accuracy, several parameters must be properly chosen. Since the simulation employs a fixed timestep, the timestep must be sufficientaly small so that information is not lost by advancing the problem too quickly. Thus, the timestep for every run is less than $0.1/\omega_{pe}$, where ω_{pe} is the electron plasma frequency. In order to minimize fluctuations, there must be a sufficient number of simulation electrons within each Debye length, λ_D. Maintaining at least 400 simulation electrons per λ_D reduces the fluctuations to about 10%. Finally, each problem must use a sufficient number of grid points per λ_D to accurately resolve the problem. A minimum of 6 grid points per λ_D was used for each simulation.

The time history of the normalized electric potential at the electrically floating surface is shown in Fig. 4.17. Each curve corresponds to a different ratio of the plasma ion to plasma electron temperatures, $\tau_i = 0.1, 1.0, 10.0$. The value of ψ_{se} typically

τ_i	ψ_{se}	
	theory	simulation ($\pm 10\%$)
0.1	4.218	3.684
1.0	2.834	3.127
10.0	1.938	2.361

Table 4.2. Comparison between the normalzied surface potential predicted by the fully kinetic theory and the particle-in-cell simulation.

fluctuates at the plasma frequency and depends upon the time-dependent number of electrons within the sheath. The initial rise in $\psi_{se} = -e\phi_s/T_{pe}$, starting from zero, results from the more mobile electrons reaching the surface first. The normalized surface potential decreases as the ions begin impacting the surface and negating the original build-up of negative charge. Eventually, ψ_{se} reaches a steady-state value when the net flux of particles, as well as the number of particles, equalizes. Note that ψ_{se} peaks at a larger value for smaller τ_i since it takes slightly longer for the less-mobile ions to reach the surface. Note that some of the high-frequency variation in ψ_{se} results from the ion sub-cycling (some are also plasma oscillations at the plasma frequency). This effect is numerical and could be completely removed by not sub-cycling the ions. The corresponding stead-state profiles are shown in Fig. 4.17(b). It is clear that increasing τ_i increases the potential throughout the sheath, although the differences are small near the edge plasma, $x = L$. The values for ψ_{se} are given in Table 4.2 for both the theoretical and simulation predictions. The values agree within 20% of the principal simulation values and within 10% under the most favorable conditions.

The phase-space and particle density for each species are shown in Fig. 4.18, corresponding to the $\tau_i = 1$ case. All the ions entering the the region, at $x = L$, pass to the surface — none are reflected. This is expected for a montonically decreasing

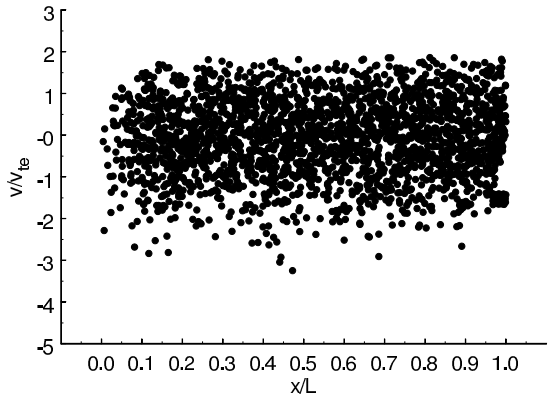

(a) electron phase-space

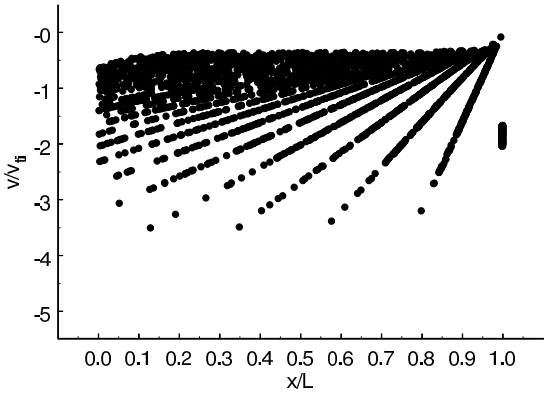

(b) ion phase-space

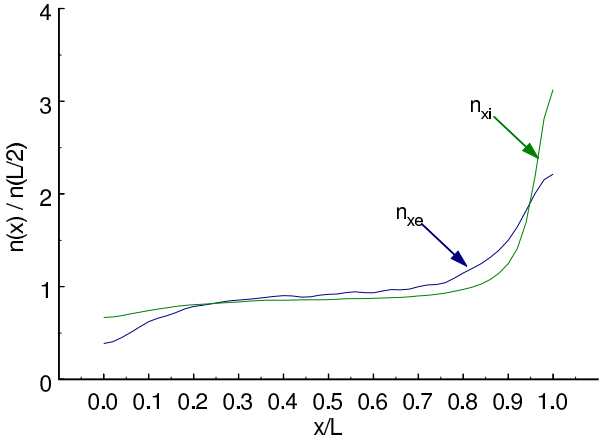

(c) particle density

FIG. 4.18. Phase-space and particle densities for the plasma electrons and ions for $\tau_i = 1$. The scatter plots show only half of the actual simulation particles. The positions are normalized to the system length and the velocities are scaled to the particle's thermal velocity. The particle densities are scaled to the density at the midplane.

profile. Only the fastest electrons impact the surface. The remaining particles are reflected by the potential and return to the plasma. Since these figures are taken from the steady-state, the accumulated negative charge on the surface repels most of the electrons, shown by the low electron density near the surface. It should be noted that the striations in the phase-space plots are an artifact of injecting particles only at discrete times and are exaggerated for the ions due to sub-cycling. The electron and ion particle densities are each normalized to their value at $x = L/2$. This provides for easy comparison since their physical densities are of different scales. The regions near the boundaries are ion-rich ($n_i > n_e$) whereas the central region of the sheath is characterized as slightly electron-rich.

Summary

The ability to accurately predict the sheath structure at the interface between a plasma and a material surface as well as the effects on particle transport to the surface, are relevant for several areas of physics. Two popular approachs to this problem are based upon the fluid equations and kinetic theory. Although modelling the sheath as a fluid provides a convenient starting point and circumvents much of the difficulty contained within kinetic theory, the averaging process used to develop the equations misses detailed information about the system. If a complete description of the sheath is desired, kinetic theory must be used to determine the phase-space distribution functions which contain a complete description of the sheath. To concentrate on the sheath itself and avoid modelling the entire bulk plasma, the planar source model is a convenient tool. Replacing the edge-plasma (that portion of the plasma outside the sheath and presheath) with a planar source of half-Maxwellian particles simplifies the analysis and replaces the nonlinear integro-differential equation for the plasma

potential with a system of algebraic, nonlinear equations which are much simpler to solve.

This chapter has used the fully kinetic sheath theory, including the planar source model, to study plasma sheaths in contact with electron-emitting surfaces for three electric potential profiles: 1) monotonically decreasing; 2) single-minimum, negative surface; and 3) single-minimum, positive surface. Three particle species were considered, each with an arbitrary temperature: 1) plasma ions of a single, positive charge state; 2) plasma electrons; and 3) surface electrons emitted from the surface with an arbitrary electron emission coefficient. The emission model considers only plasma electrons to produce surface emission; the plasma ions and emitted electrons do not participate in the production of surface-emitted electrons.

After constructing the distribution function for each species, including the important effects of forbidden regions of phase-space, expressions for the particle density, flux, normalized temperature and energy flux were determined. The particle fluxes were used to construct a normalized current density which allows a net flux of charge through the sheath to be considered. The densities were then used to determine the total charge density. A system of equations was then developed to describe the electric potential at the edge-plasma, surface and the potential minimum by applying boundary conditions to the charge density (and the electric field, for the case of space-charge saturation). These equations were then numerically solved for a range of parameter values in order to produce approximate expressions for the potential at these locations, as well as the secondary electron emission coefficient for the transition to space-charge saturation. These expressions detour the necessity to solve the nonlinear system in order to estimate the sheath potential.

The dependence of the edge-plasma and surface potentials on the plasma and surface parameters was then investigated. Choosing a base set of parameter values, each parameter was varied, while the others remained constant, over a reasonable range of values and the potential values numerically determined. The variation of the particle density, normalized temperature and energy flux for each species throughout the sheath was then considered for both the presence and absence of space-charge saturation. Since the secondary electron emission coefficient is most prominent in determining the degree of space-charge saturation within the sheath, the change in these three distribution function moments, as functions of this parameter, were considered.

Finally, a simulation of the sheath, evloving to the steady-state, using particle-in-cell methods was presented. PIC methods provide a powerful tool in understanding the development and kinetic properties of plasma sheaths. Considering two different plasma ion-to-electron temperatures, the effect of the ion temeprature on the surface potential of an electrically floating electrode was presented. Although the fully kinetic sheath theory predicted, along with the simulation, that the normalized potential at the surface should decrease as the ion temperature increases, only the simulation detailed how such a state evolved. Being warmer, the ions have a larger velocity upon entering the sheath and reach the surface more quickly, leaving less time for the electrons to "charge-up" the surface. Another benefit of doing PIC simulations is the simplicity with which magnetic fields can be included. Such a task has not yet been achieved for the kinetic theory, due to the complications introduced by the gyrotron motion.

Although the presented theory provides a very thorough basis for investigating plasma sheaths, there are some limitations to its applicability. External magnetic

fields are not explicitly considered. Since the transverse velocity components are described by full-Maxwellians, any magnetic field must intersect the surface at near-normal incidence. More specialized extensions are also possible. For example, ions of different masses or multiple charge states could be considered. Cylindrical or spherical plasma-facing surfaces could be modelled for application to probes. For fusion applications, the theory could be extended to include plasma flow parallel to the surface.

REFERENCES

[1]A. Modinos, *Field, Thermionic, and Secondary Electron Emission Spectroscopy*, Plenum Press, New York, 1984.

[2]K. Ertl and R. Behrisch, "Electron emission from solid surfaces," in *Physics of Plasma-Wall Interactions in Controlled Fusion*, edited by D. E. Post and R. Behrisch (Plenum, New York, 1986).

[3]L. A. Schwager and C. K. Birdsall, "Collector and Source Sheaths of a Finite Ion Temperature Plamsa," Phys. Fluids B **2**, 1057 (1990).

[4]T. Intrator et al., "The Virtual Cathode as a Transient Double Sheath," J. Appl. Phys. **64**, 2927 (1988).

CHAPTER 5

CURRENT LIMITATIONS IN PLANAR PLASMA SHEATHS

Having discussed space-charge limited currents in cylindrical drift tubes and planar sheaths, these two topics are now connected by investigating the sheath at the space-charge limit. It was mentioned in the previous chapter that two quantites play the largest role in determining the degree of space-charge saturation within the sheath: the secondary electron emission coefficient and the normalized current density. For the sheath structures considered, the emission coefficient is most significant since it is the negative space-charge contributed by the surface electrons that dictates whether the sheath is space-charge saturated. Although the normalized current density can be increased to saturate the sheath, in most cases, its affect can be easily overcome by varying the emission coefficient.

To review the problem, consider the sheath electric potential profiles shown in Fig. 5.1. The top curve represents the monotonically increasing potential present in a sheath that is not space-charge saturated. The depression in the bottom curve indicates that this profile corresponds to the presence of space-charge saturation. Finally, the middle curve, whose electric field is zero at the left, represents the space-charge limit.

The procedure for analyzing the space-charge limited current (SCLC) in cylindrical drift tubes involved applying boundary conditions on the electric potential along the problem boundary as well as forcing the electric field to be zero at the electron-emitting surface. A similar method is used for analysing the SCLC in the

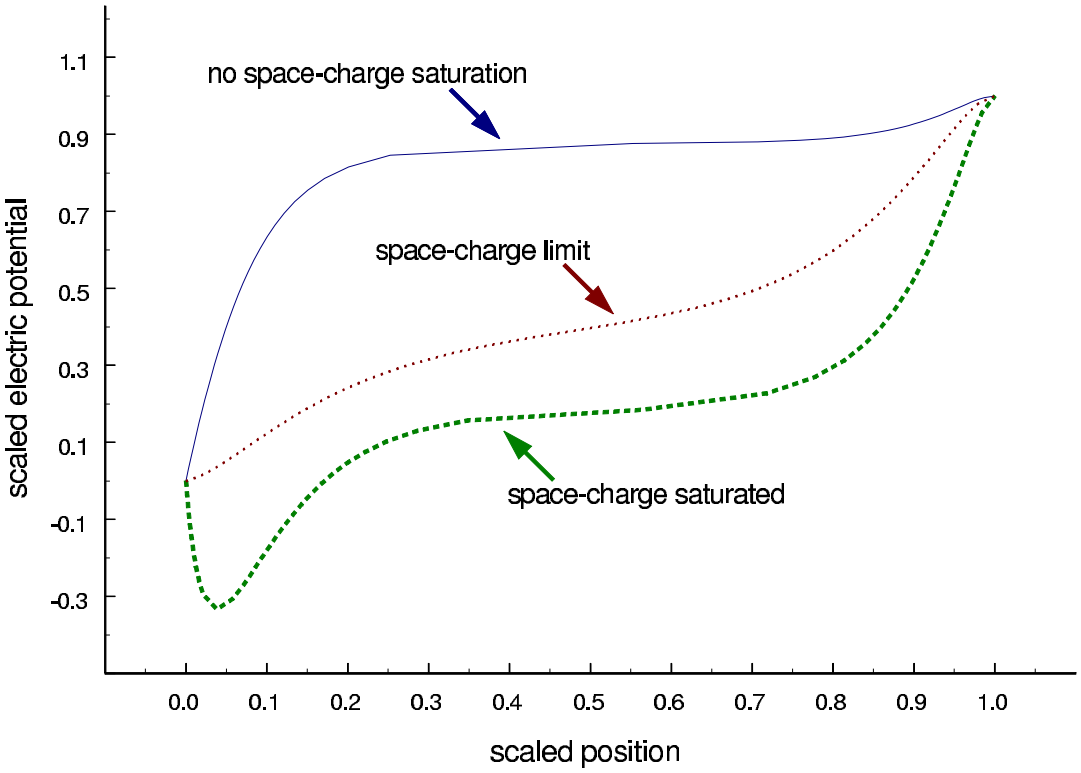

FIG. 5.1. Electric potential profiles for three levels of space-charge saturation within a plasma sheath. The top curve corresponds to the absence of space-charge saturation while the non-monotonicity of the bottom curve indicates the presence of space-charge saturation. The zero electric field at left end of the middle curve indicates that the sheath is at the space-charge limit. (Note: These profiles are normalized in both the potential and position so that they have the same length and maximum value.)

sheath. For this case, however, there are multiple species contributing to the space-charge. In analogy to the drift tube problem, a zero electric field must be imposed at each emitting surface. According to the boundary conditions used to determine the sheath potential (see page 69), the electric field is zero at the presheath/sheath interface. Thus, the plasma particles entering the sheath (that is, the portion of the sheath between the presheath/sheath interface and the material surface) are implicitly space-charge limited. The only remaining condition is to enforce the zero electric field

condition at the electron-emitting surface. Note that this problem is similar to the problem of space-charge limited bipolar flow where positively charged particles enter a diode region from one side while negatively charge particles enter from the other side.[1,2] Similar to the single-species SCLC problem, boundary conditions are imposed on the potential at each boundary and the zero electric field condition is used, at each emitting surface, to determine the maximum current for each species. The differences between space-charge limited bipolar flow and the space-charge limited sheath are the presence of an additional species and the effect of the plasma presheath on the ions entering the sheath. Additionaly, the potential values are self-consistently determined at the sheath boundaries while they are enforced boundary conditions for the bipolar flow. This last difference is the main complication in studying the space-charge limited sheath.

Space-Charge Limited Current in a Plasma Sheath

In order to analyze the space-charge limited current within the sheath, the charge density can be determined using the results of Chap. 4. In particular, Eq. (4.86) can be manipulated to give the desired charge density and is repeated here:

$$\frac{2e^{\psi_{mpe}}}{en_{pe}}\rho\left(z\right)=\frac{1-\delta e^{-\psi_{ms\delta}}}{1-\gamma_i}\xi G_1\left(\psi_{pxi}\right)-G_2\left(\psi_{mxe}\right)-\frac{\delta}{\sqrt{\tau_\delta}}e^{-\psi_{ms\delta}}G_1\left(\psi_{mx\delta}\right). \quad (4.86)$$

Note that the equations appropriate for the single-minimum, negative surface must be used to self-consistently determine the potential values as well as the emission coefficient or the normalized current density (depending on which parameter is chosen to be an independent variable). As previously mentioned, this expression only applies between the edge-plasma (the position where the plasma particles enter the presheath), x_p, and the potential minimum, x_m. However, since for SCL flow the

potential is minimum at the material surface, x_s, the potential minimum coincides with the surface: $x_m = x_s \quad \Rightarrow \psi_{me} = \psi_{se}$. Thus, replacing every occurrence of ψ_{me} with ψ_{se} transforms Eq. (4.86) into the desired expression for the charge density:

$$\frac{2e^{\psi_{spe}}}{en_{pe}}\rho\left(z\right) = \frac{1-\delta}{1-\gamma_i}\xi G_1\left(\psi_{pxi}\right) - G_2\left(\psi_{sxe}\right) - \frac{\delta}{\sqrt{\tau_\delta}}G_1\left(\psi_{sx\delta}\right). \tag{5.1}$$

Notice that this expression is different from that one would obtain by analyzing a diode with the same particle injections. This is because of the presence of the presheath, ψ_{pe}. This *external* potential alters the injection velocities of the plasma ions from that obtained by modelling a planar diode with half-Maxwellian injection-velocity distributions modified to consider the diode potential.

Using this charge density in Poisson's equation, with the position normalized to the Debye length yields

$$\frac{d^2\psi_{xe}}{dx^2} = \frac{2}{en_{pe}}\rho\left(z\right) \tag{5.2}$$

This differential equations can be multiplied by $2\psi'_{xe}$ and integrated once from $\psi_{xe} = 0$ to ψ_{xe} to give the squared electric field as

$$\begin{aligned} e^{-\psi_{spe}}\left(\frac{d\psi_{xe}}{dx}\right)^2 \;=\; & -\frac{\xi}{\zeta}\frac{1-\delta}{1-\gamma_i}\left[G_1\left(\psi_{pxi}\right) + 2\sqrt{\frac{\psi_{pxi}}{\pi}} - G_1\left(\psi_{pi}\right) - 2\sqrt{\frac{\psi_{pi}}{\pi}}\right] \\ & - \left[G_2\left(\psi_{sxe}\right) - 2\sqrt{\frac{\psi_{sxe}}{\pi}} - G_2\left(\psi_{se}\right) + 2\sqrt{\frac{\psi_{se}}{\pi}}\right] \\ & - \delta\sqrt{\tau_\delta}\left[G_1\left(\psi_{sx\delta}\right) + 2\sqrt{\frac{\psi_{sx\delta}}{\pi}} - G_1\left(\psi_{s\delta}\right) - 2\sqrt{\frac{\psi_{s\delta}}{\pi}}\right] \end{aligned} \tag{5.3}$$

Obviously, this first-order differential equation must be solved numerically. But some information can be determined by considering the zero field condition at $x = x_s$. Applying this condition gives the normalized current density as

$$\gamma_i = 1 + \xi\frac{1-\delta}{\zeta}\frac{G_1\left(\psi_{psi}\right) + 2\sqrt{\frac{\psi_{psi}}{\pi}} - G_1\left(\psi_{pi}\right) - 2\sqrt{\frac{\psi_{pi}}{\pi}}}{1 - G_2\left(\psi_{se}\right) + \delta\sqrt{\tau_\delta}\left[1 - G_1\left(\psi_{s\delta}\right)\right] + 2\left[1-\delta\right]\sqrt{\frac{\psi_{se}}{\pi}}}. \tag{5.4}$$

This expression represents the space-charge limited current in terms of the plasma and surface parameters as well as the electric potential at the edge-plasma and material surface. Actually, this is the SCLC in terms of the maximum ion current; multiplying through by $Zen_{pi}/2\sqrt{\pi\beta_i}$ yields the actual current. Note that all the particles depend upon the surface potential whereas only the ions depend upon the edge-plasma potential. This can be expected by consideration of the Bohm criterion: the purpose of the presheath is to accelerate the ions into the sheath. Unfortunately, the values of ψ_{pe} and ψ_{se} must be numerically determined which requires the specification of γ_i. Thus, although Eq. (5.4) displays the functional dependence between the current and the potentials, it is unsuitable for numerical computation. Notice that the ion saturation current, $\gamma_i = 1$, can only be reached if $\delta = 1$ or the numerator is zero.

Having concluded that the space-charge limited current in the sheath must be numerically calculated, the required equations need to be constructed. Since the SCL corresponds to the transition to space-charge saturation, the equations developed in Chap. 4 corresponding to the single-minimum, negative surface profile provide the starting point. As previously mentioned, at the space-charge limit the potential minimum coincides with the surface, yielding a zero electric field there. Thus, Eqs. (4.89), (4.93 and (4.98) are re-written here by setting $\psi_{me} = \psi_{se}$:

$$\frac{1-\delta}{1-\gamma_i}\xi G_1\left(\psi_{pi}\right) = G_2\left(\psi_{me}\right) + \frac{\delta}{\sqrt{\tau_\delta}} G_1\left(\psi_{m\delta}\right), \tag{5.5}$$

$$\begin{aligned} -\frac{\xi}{\zeta}\frac{1-\delta}{1-\gamma_i}\left[G_1\left(\psi_{pi}\right) + 2\sqrt{\frac{\psi_{pi}}{\pi}} - 1\right] = \\ + \left[G_2\left(\psi_{se}\right) - G_2\left(\psi_{spe}\right) - 2\frac{\sqrt{\psi_{se}} - \sqrt{\psi_{spe}}}{\pi}\right] \\ +\delta\sqrt{\tau_\delta}\left[G_1\left(\psi s\delta\right) - G_1\left(\psi_{sp\delta}\right) + 2\frac{\sqrt{\psi_{s\delta}} - \sqrt{\psi_{sp\delta}}}{\pi}\right], \end{aligned} \tag{5.6}$$

$$-\frac{\xi}{\zeta}\frac{1-\delta}{1-\gamma_i}\left[G_1\left(\psi_{psi}\right)-G_1\left(\psi_{pi}\right)+2\frac{\sqrt{\psi_{psi}}-\sqrt{\psi_{pi}}}{\pi}\right]=$$
$$+\left[G_2\left(\psi_{se}\right)-2\sqrt{\frac{\psi_{se}}{\pi}}-1\right]+\delta\sqrt{\tau_\delta}\left[G_1\left(\psi_{s\delta}\right)+2\sqrt{\frac{\psi_{s\delta}}{\pi}}-1\right]. \qquad (5.7)$$

These three equations must be simultaneously solved for ψ_{pe}, ψ_{se} and one parameter. Concerning the SCLC, the parameter is γ_i since the current's dependence on the other parameters is the desired goal.

Using the parameter value $\tau_\delta = 0.25$ (so that the surface electrons have sufficient energy to reasonably affect the sheath), along with $\xi = 200$ and $\zeta = 1$, these three equations are solved specifying δ over the range from 0.3 to 0.99. The results are shown in Fig. 5.2. It is clear that the normalized potential drop across the entire sheath, ψ_{spe}, decreases as the normalized current becomes increasingly negative, mainly due to the variation in the normalized surface potential, ψ_{se}. As previously mentioned, the sheath can maintain the space-charge limit despite a low surface emission coefficient, δ, if the normalized current is sufficiently large and negative. Since for $\gamma_i \ll 0$, many more electrons are being drawn from the sheath toward the edge plasma, accomplishing the same task as if δ were larger.

Ideally, one would like an expression similar to the Child-Langmuir law for a single-species, planar diode. Due to the complexity of the charge density, Eq. (5.1), an analytic solution is unavailable. An approximate expression, similar to those presented in Chap. 4 for the sheath potentials, could be determined. However, for the wide range of values which would be required, the accuracy would be lacking. One reason for this is that the length dependence would have to be determined by integrating Poisson's equation across the singularities at x_p, x_b and x_s, leading to large uncertainties in the sheath length which would make the expression of only limited

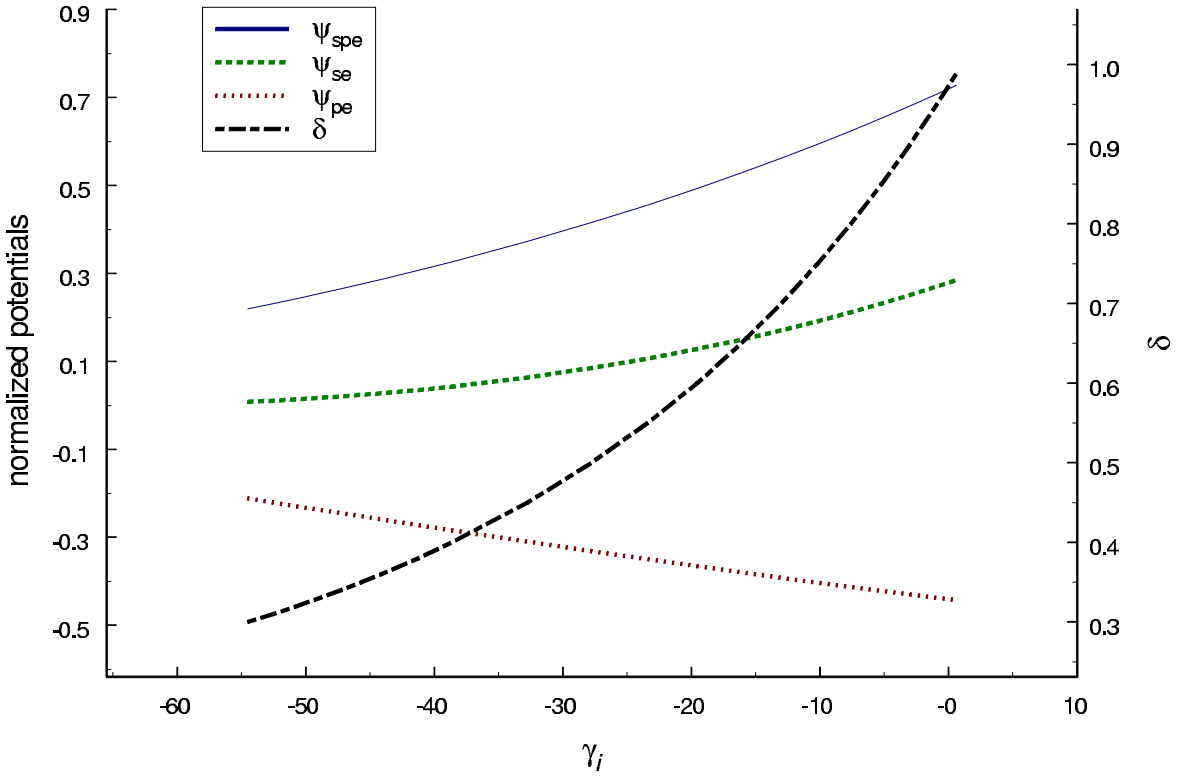

FIG. 5.2. Normalized potentials and emission coefficient profiles for various values of the ion normalized current density for a space-charge limited sheath.

value. However, a qualitative dependence is depicted in Fig. 5.3. The values used for this figure were determined by numerically integrating Poisson's equation across the entire sheath, from ψ_{pe} to ψ_{se}. These should be taken as only an indication of the relationship between γ_i and the sheath length since the integration is extremely sensitive to how closely the singularities are approached. The scant number of data points resulted from the difficulty in obtaining satisfactory results from the integration, which are determined to accurate to within 10^{-6}. Attempting a more stringent accuracy goal led to numerical difficulties. Since $1/\sqrt{\int \rho}$ is being integrated, there are regions where numerical round-off yields a negative result for $\int \rho$. This produces

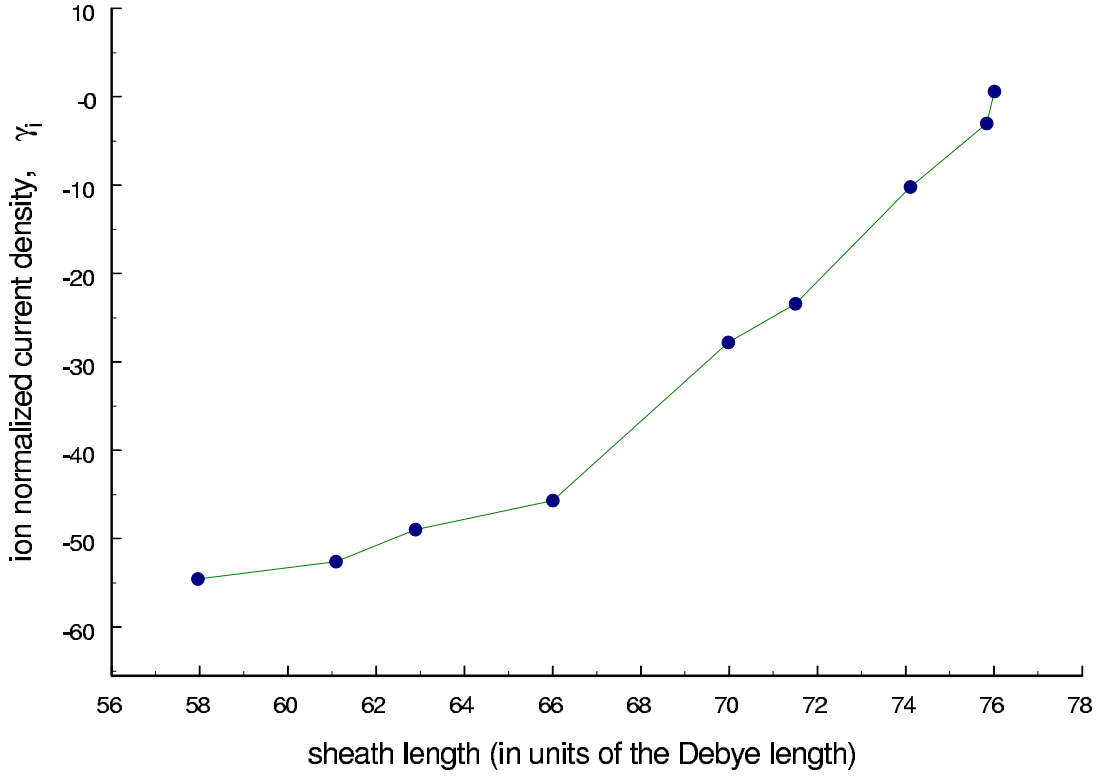

FIG. 5.3. Ion normalized current density versus the sheath length at the space-charge limit.

an imagninary contribution to the sheath length — a completely unacceptable result. Despite these difficulties, the profile shown in Fig. 5.3 shows some similarities to the single-species Child-Langmuir law: as the gap length (i.e., the sheath length) decreases, the magnitude of the current increases. However, the Child-Langmuir law dictates $J \sim V^{3/2}$ whereas within the sheath, the relation has a curvature more similar to $J \sim V^{-3/2}$.

Summary

This chapter examined the planar plasma sheath when the net current within the sheath is space-charge limited. Because of the three species involved (plasma ions,

plasma electrons and surface electrons), this requires enforcing the zero electric field condition at two locations. Since the fully kinetic sheath theory imposes a zero electric field at the presheath/sheath interface, this provides one convienent location. The other lies at the surface, from where the surface electrons are emitted into the sheath. Thus, the effect of space-charge limitation can only be examined within the sheath, not the combined presheath and sheath. However, the presheath plays a pivotal role in limiting the current within the sheath. Neglecting the presheath reduces the problem to a three-species bipolar problem, which alters the charge density. The presheath must be considered in order to accurately accurate for ion acceleration into the sheath, as stated in the Bohm criterion.

Using the fully kinetic sheath theory, the charge density is easily determined. However, because of the extremely non-linear relation to the electric potential, only numerical solutions are available. In order to solve Poisson's equation, a system of three, non-linear equations must be simultaneously solved for the potential at the surface and edge plasma as well as the ion normalized current density. By varying the plasma and/or surface parameters, the relation between the potential drop across the sheath and the current is determined. By varying the secondary electron emission coefficient, it is found that this relation bears a similar relation between the sheath length and current as found in the single-species Child-Langmuir law. However, the current displays a dependence on the sheath potential that more closely resembles $V^{-3/2}$ rather than the more familiar $V^{3/2}$.

REFERENCES

[1]C. Litwin and R. Rosner, "Relativistic Space-Charge Limited Bipolar Flow," Phys. Rev. E **58**, 1163 (1998).

[2]R. B. Miller, *An Introduction to the Physics of Intense Charge Particle Beams*, Plenum Press, New York, NY, 1982.

APPENDIX A

ELECTROSTATIC POTENTIAL IN THE INFINITE-LENGTH APPROXIMATION FOR A UNIFORM CROSS-SECTION BEAM IN A GROUNDED COAXIAL DRIFT TUBE

This appendix solves the radial Poisson equation for an annular region of uniform charge density bounded by grounded coaxial cylinders. The position and value of the potential maximum is also determined. These expressions are developed to simplify determining the space-charge limited current in the infinite-length approximation for various beam and drift tube geometries.

Letting the coaxial cylinders have radii $r_1 < r_2$ and the space-charge to be within the region $r_i < r < r_o$, Poisson's equation is given by

$$\frac{1}{r}\frac{d}{dr}r\frac{d\phi\left(r\right)}{dr} = \begin{cases} 0 & r_1 \leq r < r_i \\ -4\pi & r_i \leq r \leq r_o \\ 0 & r_o < r \leq r_2 \end{cases} . \tag{A.1}$$

This differential equation is solved by breaking the problem into three boundary value problems according to

$$\phi\left(r\right) = \begin{cases} \phi_1\left(r\right) = a_1 \ln r + b_1 & r_1 \leq r < r_i \\ \phi_0\left(r\right) = a_0 \ln r + b_0 - \pi r^2 & r_i \leq r \leq r_o \\ \phi_2\left(r\right) = a_2 \ln r + b_2 & r_o < r \leq r_2 \end{cases} . \tag{A.2}$$

Due to the homogeneous Dirichlet boundary conditions at r_1 and r_2, the expressions for ϕ_1 and ϕ_2 can be immediately simplified to

$$\begin{aligned} \phi_1\left(r\right) &= a_1 \ln \frac{r}{r_1}, \\ \phi_2\left(r\right) &= a_2 \ln \frac{r}{r_2}. \end{aligned} \tag{A.3}$$

To connect the expression in the space-charge region to those in the charge-free regions, matching conditions are required. These are taken to be continuity in the potential and the electric field at r_i and r_o. Therefore, the coefficients in ϕ_1 and ϕ_0

are related by

$$\begin{aligned} a_1 \ln \frac{r_i}{r_1} &= b_0 + a_0 \ln r_i - \pi r_i^2, \\ \frac{a_1}{r_i} &= \frac{a_0}{r_i} - 2\pi r_i, \end{aligned} \tag{A.4}$$

and in ϕ_2 and ϕ_0 by

$$\begin{aligned} a_2 \ln \frac{r_o}{r_2} &= b_0 + a_0 \ln r_o - \pi r_o^2, \\ \frac{a_2}{r_o} &= \frac{a_0}{r_o} - 2\pi r_o. \end{aligned} \tag{A.5}$$

Cancelling a_1 from Eq. (A.4) and a_2 from Eq. (A.5), two expressions for b_0 can be found:

$$a_1 \ln \frac{r_i}{r_1} - a_0 \ln r_i + \pi r_i^2 = b_0 = a_2 \ln \frac{r_o}{r_2} - a_0 \ln r_o + \pi r_o^2 \tag{A.6}$$

Solving this equation for a_0 and re-arranging terms gives

$$a_0 = -\frac{2\pi \left(r_o^2 - r_i^2\right)}{\ln r_1/r_2} \left[\frac{1}{2} - \ln \frac{r_o}{r_2} + \frac{r_i^2}{r_o^2 - r_i^2} \left(\ln \frac{r_0}{r_2} - \ln \frac{r_i}{r_1}\right)\right]. \tag{A.7}$$

Using Eq. (A.7) and reversing the steps, each of the coefficients can be determined in terms of a_0, yielding

$$\begin{aligned} b_0 &= -a_0 \ln r_2 + \pi r_o^2 \left[1 - 2 \ln \frac{r_o}{r_2}\right], \\ a_1 &= a_0 - 2\pi r_i^2, \\ a_2 &= a_0 - 2\pi r_o^2, \end{aligned} \tag{A.8}$$

Therefore, the electrostatic potential in each region can be written in terms of a_0. These expressions are:

$$\begin{aligned} \phi_1(r) &= \left[a_0 - 2\pi r_i^2\right] \ln \frac{r}{r_1}, \\ \phi_0(r) &= a_0 \ln \frac{r}{r_2} + \pi \left(r_o^2 - r^2\right) - 2\pi r_o^2 \ln \frac{r_o}{r_2}, \\ \phi_2(r) &= \left[a_0 - 2\pi r_o^2\right] \ln \frac{r}{r_2}, \end{aligned} \tag{A.9}$$

where

$$a_0 = -\frac{2\pi\left(r_o^2 - r_i^2\right)}{\ln r_1/r_2}\left[\frac{1}{2} - \ln\frac{r_o}{r_2} + \frac{r_i^2}{r_o^2 - r_i^2}\left(\ln\frac{r_0}{r_2} - \ln\frac{r_i}{r_1}\right)\right]. \tag{A.10}$$

To determine the position and value of the potential maximum, it is reasonable to only consider the region of space-charge. Thus, setting the derivative of ϕ_0, with respect to r, equal to zero and solving for r gives

$$r_{\max} = \sqrt{\frac{a_0}{2\pi}} \tag{A.11}$$

as the maximum location and

$$\phi_{\max} = \frac{a_0}{2}\ln\frac{a_0}{2\pi r_2^2} + \pi\left(r_o^2 - \frac{a_0}{2\pi}\right) - 2\pi r_o^2 \ln\frac{r_o}{r_2} \tag{A.12}$$

as the maximum potential value.

APPENDIX B

REVIEW OF PARTICLE-IN-CELL METHODS

This appendix outlines some of the basic principles of particle-in-cell (PIC) methods for simulation of plasmas. To simplify the discussion, only one spatial dimension is considered; higher dimensions are easily generalized.

A PIC code purports to accurately model the temporal evolution of a collection of particles (perhaps multiple species) governed by self-consistently determined forces. In practice, this is accomplished by discretizing space and time (as well as the kinetic equations) and applying a sequence of operations to the particles and fields. The program begins by distributing particles throughout the problem geometry. Grid-based charge and current densities are then determined by weighting the particles to the grid points. These densities are then used to integrate the field equations. Once the grid-based fields are known, they are interpolated to the particle positions in order to advance the particles in time. The entire cycle is repeated as determined by the particular problem. An excellent source for PIC methods is provided in Birdsall and Langdon.[1]

Since the physical equations must be written in a form suitable for computer use, both the geometry and time must be written is a discrete form. Thus, introduce a discrete, spatial grid covering the physical distance from $x = 0$ to $x = L$. The grid is composed of N_g vertices and $N_c = N_g - 1$ segments, or cells. The cell-width is defined as $\Delta x = L/N_c$. The grid positions are defined by

$$x_j = j\Delta x \qquad j = 0, 1, \ldots, N_c. \tag{B.1}$$

The value of any field quantity (charge density, electric potential, electric field, etc.) is defined only at the grid points according to

$$F_j = F\left(x_j\right). \tag{B.2}$$

Finally, let the problem begin at $t = 0$ with each computational cycle advancing the problem from time $t = n\Delta t$ to $t = (n + 1)\Delta t$.

Integration of the Equations of Motion

Typically, most of the computational expense is spent advancing and collecting the particles since a usual problem involves thousands of particles and only a few hundred, at most, grid points. Therefore, efficient "particle-pushers" are required. Perhaps the most popular is the *leap-frog* method applied to Hamilton's equations:

$$m\frac{d\mathbf{v}}{dt} = \mathbf{F}, \tag{B.3}$$

$$\frac{d\mathbf{x}}{dt} = \mathbf{v}. \tag{B.4}$$

These equations are finite-differenced according to a time-centered scheme to give

$$m\frac{\mathbf{v}^{n+1} - \mathbf{v}^n}{\Delta t} = \mathbf{F}^n, \tag{B.5}$$

$$\frac{\mathbf{x}^{n+1} - \mathbf{x}^n}{\Delta t} = \mathbf{v}^{n+1}. \tag{B.6}$$

For electromagnetic problems, the force $\mathbf{F}$ is composed of an electric and magnetic term:

$$\mathbf{F} = q\mathbf{E} + q\left(\frac{\mathbf{u}}{\gamma} \times \mathbf{B}\right). \tag{B.7}$$

Here, $\gamma^{-2} = 1 - (\mathbf{v}/c)^2$ is the relativistic factor and the normalized momentum, $\mathbf{u} = \gamma\mathbf{v}$, is used in lieu of the ordinary velocity, $\mathbf{v}$. A common approach to solving the equations of motion with such a force term is given by Boris.[2] The gist of this method is that only the electric field changes the magnitude of the velocities, whereas the magnetic field simply imposes a rotation. Thus, the velocity can be advanced from $n\Delta t$ to $(n + 1)\Delta t$ by the equations

$$\mathbf{v}^- = \mathbf{v}^n + \frac{q\Delta t}{2m}\mathbf{E}^n, \tag{B.8}$$

$$\mathbf{v}' = \mathbf{v}^- + \mathbf{v}^- \times \mathbf{t}, \tag{B.9}$$

$$\mathbf{v}^+ = \mathbf{v}^- + \mathbf{v}' \times \mathbf{s}, \tag{B.10}$$

$$\mathbf{v}^{n+1} = \mathbf{v}^+ + \frac{q\Delta t}{2m}\mathbf{E}^n, \tag{B.11}$$

where

$$\mathbf{t} = \frac{q\Delta t}{2\gamma^n mc}\mathbf{B} \quad \text{and} \quad \mathbf{s} = \frac{\mathbf{t}}{1+t^2}. \tag{B.12}$$

The relavtivistic factor is evaluated within this method according to $(\gamma^n)^2 = 1 + (u^-/c)^2 = 1 + (u^+/c)^2$. This procedure corresponds to a half-acceleration, a rotation, and another half-acceleration and is easily implemented in one or more dimensions. Even in one spatial dimension, all three velocity components can be used. This allows consideration of external magnetic fields that are not parallel to the spatial axis.

Weighting the Particles to the Grid

Once the particles have been advanced through phase-space, the charge and current densities need to be determined. For each particle, the particle's position and velocity are interpolated to the nearest grid points. In two dimensions, for example, the interpolation involves four grid points but only two in one-dimension. For a particle with position X_i located between the grid points x_j and x_{j+1}, the contributions to the grid based charge distribution are given by

$$q_j = q\left[1 - \frac{X_i - x_j}{\Delta x}\right], \tag{B.13}$$

$$q_{j+1} = q\frac{X_i - x_j}{\Delta x}. \tag{B.14}$$

To determine in which cell the particle lies, .i.e, the value of j, one uses the floor operator. That is, $j = \lfloor x_j/\Delta x \rfloor$ yields the integral portion of the ratio $x_j/\Delta x$.

Recalling that $x_j = j\Delta x$, these expressions can be re-written

$$q_j = q\left[j + 1 - \frac{X_i}{\Delta x}\right], \tag{B.15}$$

$$q_{j+1} = q\left[\frac{X_i}{\Delta x} - j\right]. \tag{B.16}$$

After accumulating every particle to the charge distribution, it can be recast into the charge density required for Maxwell's equations.

For electromagnetic problems, the current density is also required. Thus, each velocity component must be weighted to the grid to produce each component of the current density. The procedure is analogous to accumulating the charge distribution.

Integration of the Field Equations

After determining the charge and current densities, the field equations must be time-advanced (for electromagnetic problems) or simply integrated (for electrostatic problems). Considering only one-dimensional, electrostatic problems, the electric potential is related to the charge density according to Poisson's equation (in cgs units)

$$\frac{d^2\phi(x)}{dx^2} = -4\pi\rho(x), \tag{B.17}$$

and to the electric field by

$$E_x(x) = -\frac{d\phi(x)}{dx}. \tag{B.18}$$

These two equations are finite-differenced according to a space-centered scheme:

$$E_j = \frac{\phi_{j-1} - \phi_{j+1}}{2\Delta x} \tag{B.19}$$

$$\frac{\phi_{j+1} - 2\phi_j + \phi_{j-1}}{(\Delta x)^2} = -4\pi\rho_j. \tag{B.20}$$

Since the finite-differenced Poisson equation is a tridiagonal system with constant coefficients, it can be easily solved by the Thomas tridiagonal method.[3] Once all the ϕ_j are known, the electric field can be determined at every grid point.

The boundary conditions on the potential are imposed while solving Poisson's equation. This simply requires specifying the value of ϕ_0 and ϕ_{N_c}. For example, the potential at an electrically floating perfect conductor is determined not only from the space-charge within the half-cell but also the surface charge deposited from the convective current. For an open boundary, the value of the potential can be arbitrarily chosen. A convenient reference for boundary conditions in one-dimensional models is provided in Verboncoeur *et al.*[4]

Weighting the Fields to the Particles

After determining the electric field, it must be interpolated to the position of each particle in order to push the particle. Recall that the field is defined only at the grid points while the particles are distributed throughout the cells. Therefore, the grid point that is nearest to, and less than, the particle position needs to be determined. Since $x_0 = 0$, this is easily determined for the particle at X_i by $j = \lfloor X_i/\Delta x \rfloor$. This yields the grid index such that $x_j \leq X_i$.

Knowing in what cell the particle is, it is a simple matter to determine the force on the particle. Using only the grid points directly bounding the particle's cell, the force is given by

$$F(X_i) = \frac{x_{j+1} - X_i}{\Delta x} E_j + \frac{X_i - x_j}{\Delta x} E_{j+1}. \tag{B.21}$$

Enhancements to the Basic PIC Method

Although the essential idea of particle-in-cell methods was discussed above, there are several enhancements that can increase the realism and speed at which problems

can be simulated. This section details some of the methods incorporated in the PIC code used in this paper.

Representative Particles

For most plasma applications, the particle density present in a plasma is over a trillion particles per cubic centimeter. Attempting to model such a collection on present-day computers is completely infeasible. To circumvent this difficulty, the idea of a representative particle is mandatory. Rather than consider each electron and ion within such a plasma, the simulation aggregates many physical particles into a single representative particle. This simulation particle carries the charge and mass of many physical particles. As an example, let each simulation electron represent x_{p2c} physical electrons. Then each simulation, or representative, electron carries $-1.602 \times 10^{-19} \times x_{p2c}$ Coulombs of charge and has a mass of $9.11 \times 10^{-31} \times x_{p2c}$ kilograms. However, the acceleration of such a particle in an electric field, $\mathbf{E}$, is still only $-e\mathbf{E}/m_e$, where $-e$ and m_e are the charge and mass of a physical electron, since x_{p2c} cancels from the charge-to-mass ratio. Using representative particles allows a simulation to be tailored to a particular computer's memory capacity while allowing plasmas of arbitrary density to be modelled.

Sub-cycling

Since the mass, or inertia, of a particle defines how easily a force accelerates it, it plays a significant role in the choice of timestep. It is well known that the plasma ions, whose mass is several thousand times more than an electron's, react on much longer timescale than electrons. This fact lead many PIC users to treat the ions as a static background charge density. Although this is acceptable for some applications, it is not for modelling the sheath, for example. In this case, the motion of the ions

(neutralizing the negative charge build-up on the plasma-facing surface) is paramount. Rather than treating the ions as immobile, another approach is to employ "scaled-mass" ions. For this approach, the ion-to-electron ratio is taken to be on the order of 100. Although unrealistic, it does allow the effect of ion motion and yields qualitative information about the particular processes involved. Perhaps, the best choice is called sub-cycling.

Because the ion inertia delays any reaction to a force, compared to the electrons, the ions can be advanced through phase-space using a larger timestep than required by the electrons. This is the gist of sub-cycling. As an example, consider a hydrogen plasma in which the ion mass is 1836 times the electron mass. If each species have the same temperature, the ion thermal velocity is $\sqrt{1836}$ times the electron thermal velocity. Thus, for a timestep Δt, the electrons will move a distance $v_{te}\Delta t$ while the ions will move only $v_{ti}\Delta t = v_{te}\Delta t/\sqrt{1836}$. Thus if the ions are advanced $\sqrt{1836}$ cycles, they will move a distance comparable to the distance an electron would move each cycle. Therefore, sub-cycling allows realistic ion (or neutral) masses to be considered while avoiding severely increasing the problem runtime.

REFERENCES

[1]C. K. Birdsall and A. B. Langdon, *Plasma Simulation via Computer Simulation*, MacGraw-Hill, New York, 1985.

[2]J. P. Boris, "Relativistic Plasma Simulation-Optimization of a Hybrid Code," Fourth Conf. Num. Sim. Plasmas 3-67, Naval Research Laboratory, Washington, D.C., 1970.

[3]R. W. Hockney and J. W. Eastwood, *Computer Simulation Using Particles*, McGraw-Hill, New York, 1981.

[4]J. P. Verboncoeur, M. V. Alves, V. Vahedi, and C. K. Birdsall, "Simultaneous Potential and Circuit Solution for 1D Bounded Plasma Particle Simulation Codes," J. Comp. Phys. **104**, 321 (1993).

BIBLIOGRAPHY

Abramowitz, M. and I. A. Stegun, editors, *Handbook of Mathematical Functions*, (National Bureau of Standards, Washington, D.C., 1964).

Auer, P., J. Appl. Phys. **13**, 2096 (1960).

Benford, J. and J. Swagle, *High-Power Microwaves*, (Artech House, Boston, MA, 1992).

Biblarz, O. and G. S. Brown, "Plasma-sheath Approximate Solutions for Planar and Cylindrical Anodes and Probes," J. Appl. Phys. **73**(12), 8111 (1993).

Biehler, S., G. Ecker, and K.-U. Riemann, "Theory of the Presheath in a Weakly Ionized Plasma with Hot Neutrals," Phys. Fluids **31**(7), 1999 (1988).

Birdsall, C. K. and W. B. Bridges, *Electron Dynamics of Diode Regions*, (Academic Press, New York, 1966).

Birdsall, C. K. and A. B. Langdon, *Plasma Simulation via Computer Simulation*, (MacGraw-Hill, New York, 1985).

Bissell, R. C., "The Application of the Generalized Bohm Criterion to Emmert's Solution of the Warm Ion Collisionless Plasma Equation," Phys. Fluids **30**(7), 2264 (1987).

Bissell, R. C. and P. C. Johnson, "The Solution of the Plasma Equation in Plane Parallel Geometry with a Maxwellian Source," Phys. Fluids **30**(3), 779 (1987).

Bogdankevich, L. S. and A. A. Rukhadze, "Stability of Relativistic Electron Beams in a Plasma and the Problem of Critical Currents," Sov. Phys. Usp. **14**(2), 163 (1971).

Bohm, D., "Minimum ionic kinetic energy for a stable sheath," in *The Characteristics of Electrical Discharges in Magnetic Fields*, edited by A. Guthry and R. K. Wakerling (McGraw-Hill, New York, 1949), Chap. 3.

Boris, J. P., "Relativistic Plasma Simulation-Optimization of a Hybrid Code," Fourth Conf. Num. Sim. Plasmas 3-67, Naval Research Laboratory, Washington, D.C., 1970.

Brewer, G. R., "Graphs of the Space-Charge Depression of Potential in a Cylindrical Electron Beam," Etl Memorandum 55-26, Hughes Aircraft Company, Culver City, CA, 1955.

Bridges, W. B., J. I. Frey, and C. K. Birdsall, "Limiting Stable Currents in Bounded Electron and Ion Streams," I. E. E. E. Trans. Electron Devices **ED-12**, 264 (1965).

Bull, C. S., "Space-Charge Effects in Beam Tetrodes and Other Valves," J. I. E. E., Part III **95**, 17 (1948).

Caruso, A. and A. Cavaliere, "Velocity Anisotropy of the Sheath Region," Nuovo Cimento **26**, 1389 (1962).

Chen, F., "Electric Probes," in *Plasma Diagnotic Techniques*, edited by R. H. Huddlestone and S. L. Leonard (Academic Press, New York, 1965), Chap. 4.

Colombant, D. G. and Y. Y. Lau, "Nonlinear Beam Loading and Dynamical Limiting Currents in a High-Power Microwave Gap," Phys. Rev. Lett. **64**(19), 2320 (1990).

Crystal, T. L., P. C. Gray, W. S. Lawson, C. K. Birdsall, and S. Kuhn, "Trapped-electron Effects on Time-independent Negative-bias States of a Collisionless Single-emitter Plasma Device: Theory and Simulation," Phys. Fluids B **3**(1), 244 (1991).

Destler, W. W., L. E. Floyd, and M. Reiser, "Collective Acceleration of Heavy Ions," Phys. Rev. Lett. **44**, 70 (1980).

Drobot, A. T. and K. Kim, "Space Charge Effects on the Equilibrium of Guided Electron Flow with Gyromotion," Int. J. Electronics **51**(4), 351 (1981).

Emmert, G. A., R. M. Wieland, A. T. Mense, and J. N. Davidson, "Electric Sheath and Presheath in a Collisionless, Finite Ion Temperature Plasma," Phys. Fluids **23**(4), 803 (1980).

Ertl, K. and R. Behrisch, "Electron emission from solid surfaces," in *Physics of Plasma-Wall Interactions in Controlled Fusion*, edited by D. E. Post and R. Behrisch (Plenum, New York, 1986).

Franklin, R. N. and W. E. Han, "The Stability of the Plasma-Sheath with Secondary Emission," Plasma Phys. Controlled Fusion **30**(6), 771 (1988).

Gartstein, Y. N. and P. S. Ramesh, "Hysteresis and Self-Sustained Oscillations in Space Charge Limited Currents," J. Appl. Phys **83**(6), 2958 (1998).

Genoni, T. C. and W. A. Proctor, "Upper Bound for the Space-Charge Limiting Current of Annular Electron Beams," J. Plasma Phys. **23**, 129 (1980).

Gill, E. W. B., Philos. Mag. **49**, 993 (1925).

Gold, S. H. and G. S. Nusinovich, "Review of High-Power Microwave Source Research," Rev. Sci. Instrum. **68**(11), 3945 (1997).

Harrison, E. R. and W. B. Thompson, Proc. Phys. Soc. London **74**, 145 (1959).

Hockney, R. W. and J. W. Eastwood, *Computer Simulation Using Particles*, (McGraw-Hill, New York, 1981).

Hutchinson, I. H., *Principles of plasma diagnostics*, (Cambridge University Press, Cambridge, 1987).

Intrator, T. et al., "The Virtual Cathode as a Transient Double Sheath," J. Appl. Phys. **64**, 2927 (1988).

Jensen, K. L., M. A. Kodis, R. A. Murphy, and E. G. Zaidman, "Space Charge Effects on the Current-Voltage Characteristics of Gated Field Emitter Arrays," J. Appl. Phys **82**(2), 845 (1997).

Jory, H. R. and A. W. Trivelpiece, J. Appl. Phys. **40**(10), 3924 (1969).

Knipp, J. K., "Space-Charge Between Parallel Plane Grids," Radiation Lab. Rept. 534 (1944).

Kponou, A. et al., "Simulation of 10 A Electron-Beam Formation and Collection for a High Current Electron-Beam Ion Source," Rev. Sci. Instrum. **69**(2), 1120 (1998).

Kuhn, S., "Axial Equilibria, Disruptive Effects, and Buneman Instability in Collisionless Single-Ended Q-machine," Plas. Phys. **23**(10), 881 (1981).

Langmuir, C., "Discharge from Hot CaO," Phys. Rev. **32**, 492 (1911).

Langmuir, I., "The Effect of Space Charge and Residual Gases on Thermionic Currents in High Vacuum," Phys. Rev. **2**, 450 (1913).

Langmuir, I., Phys. Zeitschr. **15**, 348 (1914).

Langmuir, I., "The Effect of Space Charge and Initial Velocities on the Potential Distribution and Rhermionic Current between Parallel Plane Electrodes," Phys. Rev. **21**, 419 (1923).

Langmuir, I., "The Interaction of Electron and Positive Ion Space Charges in Cathode Sheaths," Phys. Rev. **33**, 964 (1929).

Langmuir, I. and K. T. Compton, Rev. Mod. Phys. **3**, 191 (1931).

Litwin, C. and R. Rosner, "Relativistic Space-Charge Limited Bipolar Flow," Phys. Rev. E **58**(1), 1163 (1998).

Martin, P. and G. Donoso, Phys. Fluids B **1**, 247 (1989).

Matthews, G. F., G. M. McCracken, P. Sewell, M. Woods, and B. J. Hopkins, "The Determination of Sheath Potential from Retarding Field Analyser Measurements in Tokomak Edge Plasmas," J. Nucl. Mater. **145–147**, 225 (1987).

McIntyre, R. G., "Extended Space-Charge Theory in Low-Pressure Thermionic Converters," J. Appl. Phys **33**, 2485 (1962).

McIntyre, R. G., Proc. IEEE **51**, 760 (1963).

Miller, R. B., *An Introduction to the Physics of Intense Charge Particle Beams*, (Plenum Press, New York, NY, 1982).

Misium, G. R., A. J. Lichtenberg, and M. A. Lieberman, "Macroscopic Modeling of Radio-frequency Plasma Discharges," J. Vac. Sci. Technol. A **7**(3), 1007 (1989).

Modinos, A., *Field, Thermionic, and Secondary Electron Emission Spectroscopy*, (Plenum Press, New York, 1984).

Mücke, M., R. Rao, R. Becker, and M. Kleinod, "Study of the Feasibility of Self Focusing of a Relativistic Electron Beam in an Electron Beam Ion Source/Trap," Rev. Sci. Instrum. **69**(2), 691 (1998).

Nitschke, T. E. and D. B. Graves, "Matching an RF Sheath Model to a Bulk Plasma Model," IEEE Trans. Plas. Sci. **23**(4), 717 (1995).

Ordonez, C. A., "Fully Kinetic Plasma-sheath Theory for a Cold-electron Emitting Surface," Phys. Fluids B **4**(4), 778 (1992).

Ordonez, C. A., "Boundary Conditions Including Sheath Effects at a Plasma-Facing Surface," Phys. Rev. E **55**(2), 1858 (1997).

O'Shea, P. G., W. W. Destler, J. Rodgers, and Z. Segalov, "Laser-Controlled Collective Ion Accelerator," Appl. Phys. Lett. **49**, 1696 (1986).

Ott, W., "Investigation of a Cesium Plasma Diode Using an Electron Beam Probing Technique," Z. Naturforsch. **22**, 1057 (1967).

Qian, B.-L., Y.-G. Liu, and C.-L. Li, "Both Temperature and Relativistic Effects on the Langmuir-Child Equation," Phys. Plasmas **1**(7), 2398 (1994).

Riemann, K.-U., "Kinetic Theory of the Plasma Sheath in a Weakly Ionized Plasma," Phys. Fluids **24**(12), 2163 (1981).

Rynn, N., "Plasma Column End Effects," Phys. Fluids **9**, 165 (1966).

Schwager, L. A., "Effects of Secondary and Thermionic Electron Emission on the Collector and Source Sheaths of a Finite Ion Temperature Plasma using Kinetic Theory and Numerical Simulation," Phys. Fluids B **5**(2), 631 (1993).

Schwager, L. A. and C. K. Birdsall, "Collector and Source Sheaths of a Finite Ion Temperature Plamsa," Phys. Fluids B **2**, 1057 (1990).

Self, S. A., Phys. Fluids **6**, 1762 (1963).

Sheuer, J. T. and G. A. Emmert, "Sheath and Presheath in a Collisionless Plasma with a Maxwellian Source," Phys. Fluids **31**(12), 3645 (1988).

Sizonenko, V. L., "Effects of Strong Secondary Electron Emission of a Plasma Layer," Sov. Phys. Tech. Phys. **26**(11), 1345 (1981).

Smith, L. P. and P. L. Hartman, "The Formation and Maintenance of Electron and Ion Beams," J. Appl. Phys. **11**, 220 (1940).

Spencer, T. A., J. J. Hendricks, J. W. Luginsland, and M. D. Stump, "Dynamics of the Space-Charge-Limiting Current in Gyro-Type Devices," IEEE Trans. Plasma Science **26**(3), 854 (1998).

Stangeby, P. C., "Plasma Sheath Transmission Factors for Tokomak Edge Plasmas," Phys. Fluids **27**(3), 682 (1984).

Stangeby, P. C., "Large Probes in Tokomak Scrape-off Plasmas. Analytic Model for the Collisionless Scrape-off Layer," Phys. Fluids **28**(2), 644 (1985).

Stangeby, P. C., "Edge Probes," J. Nucl. Mater. **145–147**, 105 (1987).

Stephens, II, K. F. and C. A. Ordonez, "Sheath and Presheath Potentials for Anode, Cathode and Floating Plasma-Facing Surface," J. Appl. Phys. **85**(5), 2522 (1999).

Stephens, II, K. F., C. A. Ordonez, and R. E. Peterkin, Jr., "Virtual Cathode Formations in Nested-Well Configurations," in *Non-Neutral Plasma Physics III*, edited by J. J. Bollinger, R. L. Spencer, and R. C. Davidson (American Institue of Physics, Melville, N. Y., 1999), page 451.

Stephens II, K. F. and C. A. Ordonez, "Upper Bound for the Space-Charge Limited Current of Relativistic Electron Beams in Finite-Length Coaxial Drift Tubes," Phys. Plasmas. **7**(7) (2000).

Tonks, L. and I. Langmuir, "A General Theory of the Plasma of an Arc," Phys. Rev. **34**, 876 (1929).

Verboncoeur, J. P., M. V. Alves, V. Vahedi, and C. K. Birdsall, "Simultaneous Potential and Circuit Solution for 1D Bounded Plasma Particle Simulation Codes," J. Comp. Phys. **104**(2), 321 (1993).

Voronin, V. S., Y. T. Zozulaya, and A. N. Lebedev, "Self-Consistent Stationary State of a Relativistic Electron Beam in a Drift Space," Soviet Phys. Tech. Phys. **17**, 432 (1972).

Walker, G. B., "Space-Charge Effects Between a Positive Grid and Anode of a Beam Tetrode," Wireless Engineer **22**, 157 (1945).

Wax, N., "Some Properties of Tubular Electron Beams," J. Appl. Phys. **20**, 242 (1949).

Zhu, P., J. J. Lowke, and R. Morrow, "A Unified Theory of Free Burning Arcs, Cathode Sheaths and Cathodes," J. Phys. D: Appl. Phys **25**, 1221 (1992).